IOWA STATE UNIVERSITY
Digital Repository

Graduate Theses and Dissertations | Graduate College

2014

Particle production at small-x in deep inelastic scattering

Dajing Wu
Iowa State University

Follow this and additional works at: http://lib.dr.iastate.edu/etd

 Part of the Physics Commons

Recommended Citation
Wu, Dajing, "Particle production at small-x in deep inelastic scattering" (2014). *Graduate Theses and Dissertations*. 13846.
http://lib.dr.iastate.edu/etd/13846

This Dissertation is brought to you for free and open access by the Graduate College at Iowa State University Digital Repository. It has been accepted for inclusion in Graduate Theses and Dissertations by an authorized administrator of Iowa State University Digital Repository. For more information, please contact digirep@iastate.edu.

Particle production at small-x in deep inelastic scattering

by

Dajing Wu

A dissertation submitted to the graduate faculty

in partial fulfillment of the requirements for the degree of

DOCTOR OF PHILOSOPHY

Major: Nuclear Physics

Program of Study Committee:

Kirill Tuchin, Major Professor

James Vary

Marzia Rosati

Kerry Whisnant

Alexander Roitershtein

Iowa State University

Ames, Iowa

2014

Copyright © Dajing Wu, 2014. All rights reserved.

DEDICATION

I would like to dedicate this thesis to my father, Xianggui Wu, and my mother, Wenfang Tang. Without their encouragement and support, I could not have completed such work.

TABLE OF CONTENTS

LIST OF FIGURES

ABSTRACT

The properties of small-x QCD are studied in this dissertation. One of the most interesting features of small-x physics is gluon saturation effect and to obtain direct evidence of this effect has been of great theoretical and experimental interest. We focus on deep inelastic scattering off heavy nucleus which may provide the first evidence of gluon saturation. Our results might be put into test in future by Electron-Ion Collider(EIC). We studied k_T spectrum in gluon production and analyzed the result in different regimes of nuclear matter, dilute nucleus and saturated nucleus included. We first studied diffractive gluon production in small-x DIS, which itself is an excellent probe to detect gluon distribution inside nucleus. We then made an investigation on inclusive gluon production in DIS and, specifically, tried to understand the contribution from momentum conservation.

ACKNOWLEGEMENT

I would like to take this opportunity to express my gratitudes to my advisor Kirill Tuchin, who is always insightful in physics and patient in tutoring me from the very beginning. Without his valuable help, it is impossible for me to push my understanding in physics and research work to such depth and width.

I also wish to thank my POS committee members Prof. James Vary, Prof. Marzia Rosati, Prof. Kerry Whisnant and Prof. Alexander Roitershtein for devoting their time to the careful examination of my research and offering their valuable advice.

Great thanks go to my classmates and friends in Iowa State with whom I studied and discussed questions together in such free atmosphere.

PART I

Theoretical foundations for small-x physics

CHAPTER 1. QCD as a theory for strong interactions

1.1 QCD Lagrangian

Quantum chromodynamics is the theory of strong interactions. Specifically, QCD is SU(3) local gauge theory [1, 13]. The QCD Lagrangian density reads [4, 5, 6, 7, 8],

$$\mathcal{L}_{QCD} = \sum_f \bar{q}_i^f(x)[i\gamma^\mu D_\mu - m_f]_{ij} q_j^f(x) - \frac{1}{4} F^a_{\mu\nu} F^{a\mu\nu} \tag{1.1.1}$$

Where $\bar{q}^f$ and q^f are spinors of antiquark and quark of spin-$\frac{1}{2}$. Covariant derivative

$$D_\mu = \partial_\mu - igA_\mu = \partial_\mu - igt^a A^a_\mu \tag{1.1.2}$$

while field strength tensor

$$F_{\mu\nu} = \frac{i}{g}[D_\mu, D_\nu] = t^a F^a_{\mu\nu} \tag{1.1.3}$$

It can be checked that

$$F^a_{\mu\nu} = \partial_\mu A^a_\nu - \partial_\nu A^a_\mu + g f_{abc} A^b_\mu A^c_\nu \tag{1.1.4}$$

where t^a are the fundamental representation matrices of generators of SU(3) group and f^{abs} stand for the structure constants of the SU(3) group.

1.2 Perturbative QCD

No exact solution to QCD has been found so far and it is thus often approached perturbatively. Like QED, people often calculate the process order by order with respect

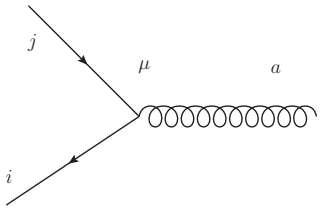

(a)Quark-gluon vertex

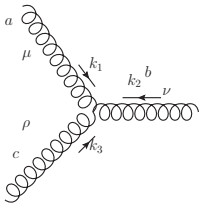

(b) 3-gluon vertex

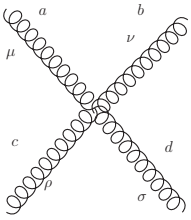

(c)4-gluon vertex

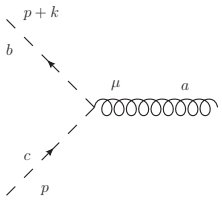

(d)Gluon-ghost vertex(in Lorentz gauge)

Figure 1.1 Vertices in QCD.

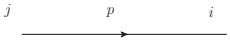

(a)Quark propagator

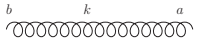

(b)Gluon propagator

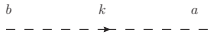

(c)Ghost propagator

Figure 1.2 Propagators in QCD

to the coupling constant. The coupling constant of QCD reads [2, 3]

$$\alpha_s(Q^2) = \frac{1}{\beta_2 \ln(Q^2/\Lambda^2_{QCD})}, \tag{1.2.1}$$

where $\beta_2 = \frac{11N_c - 2N_f}{12\pi}$ and Λ_{QCD} is a non-perturbative scale of the order of $200MeV$. In fact, $\alpha_s(M_z^2) = 0.118 \pm 0.011$, where $M_z = 91.2$GeV is the mass of Z-boson [50].

One can see that α_s decreases with growing energy scale, i.e., it becomes stronger at larger distances. The crucial observation is that for sufficiently high Q^2, $\alpha_s(Q^2)$ serves as the expansion parameter. Feynman rules are listed as follows [4]

1. Quark-gluon vertex: $ig\gamma^\mu(t^a)_{ji}$

2. 3-gluon vertex: $-gf^{abc}[g^{\mu\rho}(k_1 - k_3)^\nu + g^{\mu\nu}(k_2 - k_1)^\rho + g^{\nu\rho}(k_3 - k_2)^\mu]$

3. 4-gluon vertex:

$$-ig^2[f^{abe}f^{cde}(g^{\mu\rho}g^{\nu\sigma}-g^{\mu\sigma}g^{\nu\rho})+f^{ace}f^{bde}(g^{\mu\nu}g^{\rho\sigma}-g^{\mu\sigma}g^{\nu\rho})+f^{ade}f^{bce}(g^{\mu\nu}g^{\rho\sigma}-g^{\mu\rho}g^{\nu\sigma})]$$

4. Ghost-gluon vertex: $gf^{abc}(p+k)^\mu$

5. Quark propagator: $\frac{i(\not{p}+m_f)}{p^2-m_f^2+i\epsilon}\delta^{ij}$

6. Gluon propagator: $\frac{-id_{\mu\nu}^{(k)}}{k^2+i\epsilon}\delta^{ab}$,
   where $d_{\mu\nu}^{(k)}=\sum_{\lambda=\pm}\epsilon_\mu^\lambda(k)\epsilon_\nu^{\lambda*}(k)$ In Feynman gauge $d_{\mu\nu}^{(k)}=g_{\mu\nu}$ while in the light-cone gauge $d_{\mu\nu}^{(k)}=g_{\mu\nu}-\frac{\eta_\mu k_\nu+\eta_\nu k_\mu}{\eta\cdot k}$

7. Ghost propagator: $\frac{i}{k^2+i\epsilon}\delta^{ab}$

8. Include a factor of -1 for each fermion loop

1.3 Light-cone perturbation theory

Equal-time quantization quantize the wave function into field operators at $t=0$. The Light-cone quantization differs from equal-time quantization in that the quantization condition is imposed at the $x^+=0$, where *

$$p^+=p^0+p^3,\qquad p^-=p-p^3,\qquad \boldsymbol{p}=\boldsymbol{p} \tag{1.3.3}$$

$$x^+=t+x,\qquad x^-=t-x,\qquad \boldsymbol{x}=\boldsymbol{x} \tag{1.3.4}$$

Thus,

$$p\cdot q=p^0q^0-p^1q^1-p^2q^2-p^3q^3=\frac{1}{2}(p^+q^-+p^-q^+)-p^1q^1-p^2q^2. \tag{1.3.5}$$

*Note that throughout this dissertation we adopted the "bold" notation for the transverse components of 4-vectors, i.e., for 4-vector

$$v\equiv(v^0,v^1,v^2,v^3), \tag{1.3.1}$$

$$\boldsymbol{v}\equiv(v^1,v^2) \tag{1.3.2}$$

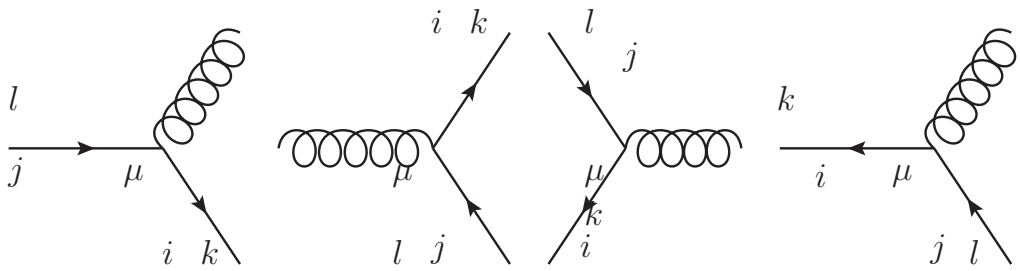

(a) Quark-gluon vertex

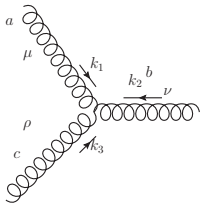

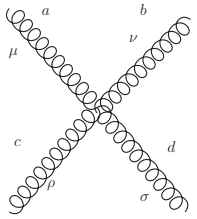

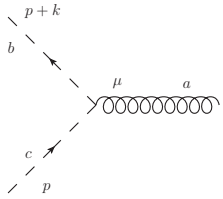

(b)3-gluon vertex (c)4-gluon vertex (d)Gluon-ghost vertex (in Lorentz gauge)

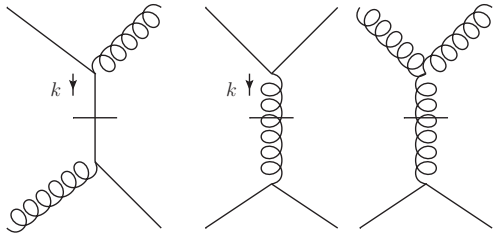

(e)instantaneous propagators in light-cone perturbation theory

and

$$p \cdot x = p^0 x^0 - p^1 x^1 - p^2 x^2 - p^3 x^3 = \frac{1}{2}(p^+ x^- + p^- x^+) - p^1 x^1 - p^2 x^2. \tag{1.3.6}$$

x^+ plays the role as time and p^- is the equivalence of energy in Light-Cone field theory in comparison with covariant field theory.

The rules for light-cone perturbation theory is listed as follows [17],[18],[19],

1. Assign a momentum to each line such that $k^\mu = (k^+, \frac{\boldsymbol{k}^2+m^2}{k^+}, \boldsymbol{k})$. All the particles are on-shell

2. include a factor of $\theta(k^+)$ for each line.

3. For each vector boson line, include a factor of $\frac{d_{\mu\nu}^{(k)}}{k^+}$. where $d_{\mu\nu}^{(k)} = \sum_{\lambda=\pm} \epsilon_\mu^\lambda(k)\epsilon_\nu^{\lambda *}(k)$ In Feynman gauge $d_{\mu\nu}^{(k)} = -g_{\mu\nu}$ while in the light-cone gauge $d_{\mu\nu}^{(k)} = -g_{\mu\nu} + \frac{\eta_\mu k_\nu + \eta_\nu k_\mu}{\eta\cdot k}$

4. Gluon-fermion vertices are
$g\frac{\bar{u}(k)}{\sqrt{k^+}}\gamma^\mu\frac{u(l)}{\sqrt{l^+}}(t^a)_{ji}, \quad g\frac{\bar{u}(k)}{\sqrt{k^+}}\gamma^\mu\frac{v(l)}{\sqrt{l^+}}(t^a)_{ji}, \quad -g\frac{\bar{u}(k)}{\sqrt{k^+}}\gamma^\mu\frac{u(l)}{\sqrt{l^+}}(t^a)_{ji}, \quad -g\frac{\bar{u}(k)}{\sqrt{k^+}}\gamma^\mu\frac{v(l)}{\sqrt{l^+}}(t^a)_{ji}$

5. The trigluon vertex is $-gf^{abc}[g^{\mu\rho}(k_1-k_3)^\nu + g^{\mu\nu}(k_2-k_1)^\rho + g^{\nu\rho}(k_3-k_2)^\mu]$
The four-gluon vertex is $g^2[f^{abe}f^{cde}(g^{\mu\rho}g^{\nu\sigma} - g^{\mu\sigma}g^{\nu\rho}) + f^{ace}f^{bde}(g^{\mu\nu}g^{\rho\sigma} - g^{\mu\sigma}g^{\nu\rho}) + f^{ade}f^{bce}(g^{\mu\nu}g^{\rho\sigma} - g^{\mu\rho}g^{\nu\sigma})]$

6. For each intermediate state, include an energy denominator $\frac{1}{\sum_{inc} k^- - \sum_{interm} k^- + i\epsilon}$ where $\sum_{inc} k^-$ is the sum of light-cone incoming energies, while $\sum_{interm} k^-$ the sum of light-cone intermediate energies.

7. In Feynman gauge, for each ghost line, include a factor $-\frac{\theta(k^+)}{k^+}$, the gluon-ghost vertex is $gf^{abc}(p+k)^\mu$. There is no ghosts in light-cone gauge.

8. Fermion propagator has an instantaneous part $\frac{\gamma^+}{2k^+}$
Gluon propagator has an instantaneous part $\frac{\eta^\mu\eta^\nu}{k^{+2}}$ in the light-cone gauge

9. Two consecutive instantaneous propagators gives zero.

10. Integrate $\frac{1}{2(2\pi)^3}\int_0^\infty dk^+ \int d^2\boldsymbol{k}$ for each independent k's and sum over all internal spins are polarizations, as well as flavors.

11. Include a factor of -1 for any loop

Note that LCPT vertices do not conserve energy, as the Fock states considered are only part of the scattering process, but it preserve the on-shellness of the particles, by construction.

CHAPTER 2. DGLAP evolution and parton model

2.1 Parton wave function and the parton distribution function

One can, in principle, study nucleus in arbitrary frame. However, physical interpretations vary in different frames and a good choice of frame will not only simplify calculation, but also reveals more intuitive picture. Two frames are often used to describe nucleus.

- Rest frame of nucleus.
- Infinite momentum frame(IMF) or Bjorken frame: $P^+ \to \infty$. The "+" component of the nucleus is set to be much larger than any momentum scale in the system.

In studying nucleus, we will be working in the infinite momentum frame. Due to time dilation, the lifetime of the partons is much larger than the typical fluctuation time scale inside the nucleus and thus validating an unambiguous partonic description of the nucleus contents. This is a clear advantage of IMF.

Starting from the light-cone wave function of the nucleus in Fock space [8]

$$\Psi_n^f(\{x_i, \boldsymbol{k}_i\}; x, \boldsymbol{k}; \sigma), \tag{2.1.1}$$

which is multi-particle wave function for n-spectator partons in the Fock state of transverse momentum $\boldsymbol{k}_i$ and longitudinal momentum fraction x_i, along with one measured quark with transverse momentum $\boldsymbol{k}$, longitudinal momentum fraction x and parton polarization σ.

The parton distribution function is related to Ψ_n^f by [8]

$$q^f(x,Q^2) = \sum_n \frac{1}{x}\int \frac{d^2\boldsymbol{k}}{2(2\pi)^3}\frac{1}{S_n}\sum_{\sigma=\pm1}\prod_{i=1}^{n}\frac{dx_i}{x_i}\frac{d^2\boldsymbol{k}_i}{2(2\pi)^3} \\ |\Psi_n^f(\{x_i,\boldsymbol{k}_i\};x,\boldsymbol{k};\sigma)|^2(2\pi)^3\delta^2\left(\boldsymbol{k}+\sum_{j=1}^{n}\boldsymbol{k}_j\right)\delta\left(1-x-\sum_{i=1}^{n}x_i\right). \tag{2.1.2}$$

The Gluon distribution can be defined in the same way as the quark distribution[8].

$$G(x,Q^2) = \sum_n \frac{1}{x}\int \frac{d^2\boldsymbol{k}}{2(2\pi)^3}\frac{1}{S_n}\sum_{\sigma=\pm1}\prod_{i=1}^{n}\frac{dx_i}{x_i}\frac{d^2k_i}{2(2\pi)^3} \\ |\Psi_n(\{x_i,\boldsymbol{k}_i\};x,\boldsymbol{k};\sigma)|^2(2\pi)^3\delta^2\left(\boldsymbol{k}+\sum_{j=1}^{n}\boldsymbol{k}_j\right)\delta\left(1-x-\sum_{i=1}^{n}x_i\right). \tag{2.1.3}$$

Note that $S_n = n_G n_q n_{\bar{Q}}$ is the symmetry factor, where n_G,n_q and $n_{\bar{Q}}$ stand for, respectively, the number of gluon, quark and anti-quark in the wave function.

The advantage of light cone approach over covariant approach lies in its clear space-time picture at high energies. To be specific, processes with well-defined time sequence disentangles, making great simplification to the physical picture and to calculations.

2.2 DGLAP evolution equation

One might have already noticed that the PDFs are Q^2-dependent. However, the definitions (2.1.2)(2.1.3) do not exhibit a manifesting Q^2 dependence. In fact Q^2 enters as the upper bound for the transverse momenta of the partons and plays the role as the quantification of the sharpness of the microscopic probes. The larger the Q^2, the better resolution the 'microscope' has, and the smaller the size of partons are detected. Since no probe whatsoever can resolve infinitely small objects, Q^2 has to be finite. The perception of the parton numbers is actually varying with the sharpness of the probe, and so do the PDFs which count the number of partons the probe can resolve. The probe can respond only to the partons with transverse size larger than $\sim 1/Q$, while completely oblivious of the smaller ones. In short, a PDF is the record of number of partons with

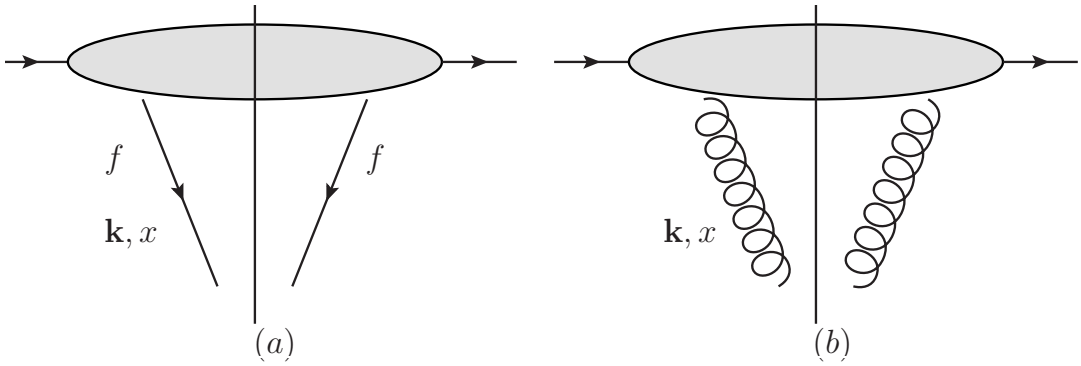

Figure 2.1 Diagrammatical illustrations of (a) quark distribution function, (b) gluon distribution function.

transverse momentum smaller or equal to $1/Q$, with longitudinal momentum fraction x of the nucleon/nucleus.

It would be very interesting to find exactly how PDFs evolve with Q^2. If the high-Q^2 limit is taken, the problem simplifies to resumming over $\alpha_s \ln(Q^2/\Lambda^2_{QCD})$, in which $\alpha_s \ln(Q^2/\Lambda^2_{QCD}) \sim 1$. Noticing that even though the high Q^2 leads to small coupling, i.e., $\alpha_s \ll 1$,the accompanying factor $\ln(Q^2/\Lambda^2_{QCD}) \gg 1$ compensates for the smallness of the coupling, rendering the terms with expansion parameter $\alpha_s \ln(Q^2/\Lambda^2_{QCD})$ nonnegligible. The logarithmic enhancement due to Q^2 make it necessary to resum to all orders of the parameter $\alpha_s \ln(Q^2/\Lambda^2_{QCD})$.

Starting from a known parton distribution q^f, if the resolution scale Q^2 is increased, the phase space available for producing new partons expanded. For simplicity, we consider first the lowest order corrections to the quark distribution function.

Both real and virtual corrections contribute a power of α_s. Actually for large Q^2, each α_s is always accompanied by the $\ln(Q^2/\Lambda^2_{QCD})$. A detailed calculation reveals

$$q^f_A(x,Q^2) = \frac{\alpha_s C_F}{2\pi} \int^{Q^2} \frac{d\boldsymbol{k}^2}{\boldsymbol{k}^2} \int_x^1 \frac{dz}{z} \frac{1+z^2}{1-z} q^f(\frac{x}{z}, \boldsymbol{k}^2). \tag{2.2.1}$$

Where the subscript A for quark distribution function denotes the contribution from real gluon emission, shown in A of Fig. 2.2.

The contribution B and C can be calculated in the similar way. We refer the reader to

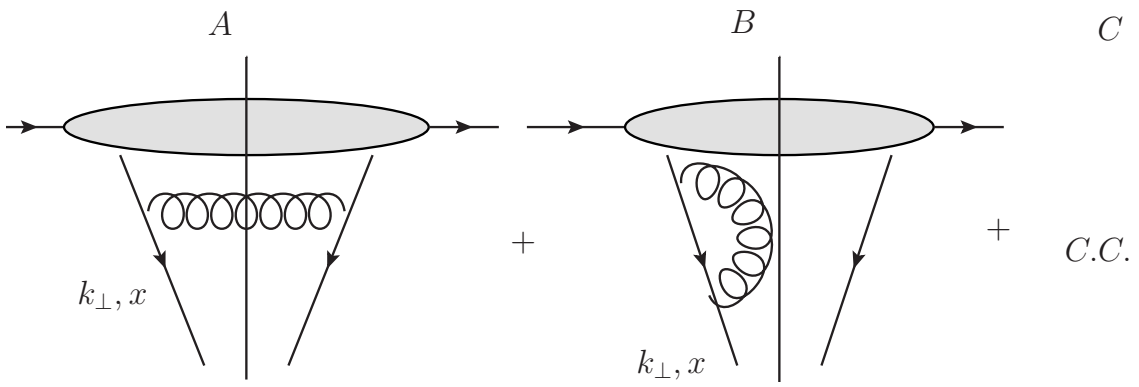

Figure 2.2 Lowest order corrections to quark distribution function. A is the real correction while B and C are virtual corrections. The solid line in the middle represents the final state

[5] and [8] for details. Note that other diagrams are omitted because they are subleading compared with $\alpha_s \ln(Q^2/\Lambda^2_{QCD})$. Further calculations must be included to not only $q \to qg$ splittings, but also, $g \to q\bar{q}$. Define flavor nonsinglet distribution function by

$$\Delta^{f\bar{f}}(x, Q^2) = q^f(x, Q^2) - \bar{q}^f(x, Q^2). \tag{2.2.2}$$

we get

$$Q^2 \frac{\partial \Delta^{f\bar{f}}(x, Q^2)}{\partial Q^2} = \frac{\alpha_s(Q^2)}{2\pi} \int_x^1 \frac{dz}{z} P_{qq}(z) \Delta^{f\bar{f}}\left(\frac{x}{z}, Q^2\right) \tag{2.2.3}$$

This evolution equation is self-contained as it treats only quark evolution. To study the gluon evolution, we further define flavor singlet distribution function by

$$\Sigma^{f\bar{f}}(x, Q^2) = \sum_f [q^f(x, Q^2) + \bar{q}^f(x, Q^2)]. \tag{2.2.4}$$

We then reach an evolution equation

$$Q^2 \frac{\partial}{\partial Q^2} \begin{pmatrix} \Sigma(x, Q^2) \\ G(x, Q^2) \end{pmatrix} = \frac{\alpha_s(Q^2)}{2\pi} \int_x^1 \frac{dz}{z} \begin{pmatrix} P_{qq}(z) & P_{qG}(z) \\ P_{Gq}(z) & P_{GG}(z) \end{pmatrix} \begin{pmatrix} \Sigma(\frac{x}{z}, Q^2) \\ G(\frac{x}{z}, Q^2) \end{pmatrix} \tag{2.2.5}$$

(2.2.3) together with (2.2.5) constitutes Dokshitzer-Gribov-Lipatov-Altarelli-Parisi (DGLAP) evolution equations [20],[21],[22],[23],[24].

Splitting functions are listed as follows,

$$
\begin{aligned}
P_{qq}(z) &= C_F \left[\frac{1+z^2}{(1-z)_+} + \frac{3}{2}\delta(1-z) \right] \\
P_{Gq}(z) &= C_F \frac{1+(1-z)^2}{z} \\
P_{qG}(z) &= N_f[z^2 + (1-z)^2] \\
P_{GG}(z) &= 2N_c \left[\frac{z}{(1-z)_+} + \frac{1-z}{z} + z(1-z) \right] + \frac{11N_c - 2N_f}{6}\delta(1-z)
\end{aligned}
\tag{2.2.6}
$$

Where we have introduced "+" notation [5],

$$
\int_x^1 dz \frac{1}{(1-z)_+} f(z) = \int_x^1 dz \frac{1}{1-z}[f(z) - f(1)] + f(1)\ln(1-x) \tag{2.2.7}
$$

The "+" treatment effectively remove the collinear singularities–singularities from the events in which the emitted parton carries the emitter's entire momentum.

2.3 General solution to DGLAP

Solutions to DGLAP equations are found in the moment space. Define

$$
f_\omega(Q^2) \equiv \int_0^1 dx x^\omega f(x, Q^2) \tag{2.3.1}
$$

to be the parton distribution in the moment space, where $f(x, Q^2)$ could be either for gluon distribution function G, singlet quark distribution Σ (2.2.4) or nonsinglet quark distribution function $\Delta^{f\bar{f}}$ (2.2.2). The inverse of Mellin transformation reads

$$
f(x, Q^2) = \int_\gamma \frac{d\omega}{2\pi i} x^{-\omega-1} f_\omega(Q^2) \tag{2.3.2}
$$

The contour γ runs to the right of all singularities in ω-space of $f_\omega(Q^2)$ The advantage of Mellin transformation is that it turns the original equations with integrals to algebraic equations.

$$
Q^2 \frac{\partial \Delta_\omega^{f\bar{f}}(Q^2)}{\partial Q^2} = \frac{\alpha_s(Q^2)}{2\pi} \gamma_{qq}(\omega) \Delta_\omega^{f\bar{f}}(Q^2) \tag{2.3.3}
$$

and

$$Q^2\frac{\partial}{\partial Q^2}\begin{pmatrix}\Sigma_\omega(Q^2)\\ G_\omega(Q^2)\end{pmatrix}=\frac{\alpha_s(Q^2)}{2\pi}\begin{pmatrix}\gamma_{qq}(\omega) & \gamma_{qG}(\omega)\\ \gamma_{Gq}(\omega) & \gamma_{GG}(\omega)\end{pmatrix}\begin{pmatrix}\Sigma_\omega(Q^2)\\ G_\omega(Q^2)\end{pmatrix} \tag{2.3.4}$$

These are DGLAP equations in the moment space. where in (2.3.3) and (2.3.4), anomalous dimension had been defined [8],

$$\gamma_{ij}=\int_0^1 dz z^\omega P_{ij}(z) \tag{2.3.5}$$

where $i,j=q,G$. From (2.2.6), we get [25][26]

$$\begin{aligned}
\gamma_{qq}(\omega)&=C_F\left[\frac{3}{2}+\frac{1}{(1+\omega)(2+\omega)}-2\psi(\omega+2)+2\psi(1)\right]\\
\gamma_{Gq}(\omega)&=C_F\left[\frac{1}{2+\omega}+\frac{2}{\omega(1+\omega)}\right]\\
\gamma_{qG}(\omega)&=N_f\left[\frac{1}{1+\omega}-\frac{2}{(2+\omega)(3+\omega)}\right]\\
\gamma_{GG}(\omega)&=2N_c\left[\frac{1}{\omega(1+\omega)}+\frac{1}{(2+\omega)(3+\omega)}-\psi(\omega+2)+\psi(1)\right]+\frac{11N_c-2N_f}{6}
\end{aligned} \tag{2.3.6}$$

where $\psi(\omega)=\Gamma'(\omega)/\Gamma(\omega)$. Experiments can give at some specific value of $Q^2=Q_0^2$ the initial condition of $\Delta_\omega^{f\bar{f}}(Q^2)$, $\Sigma_\omega(Q^2)$, and $G_\omega(Q^2)$. Then the general solutions can be derived formally from (2.3.3) and (2.3.4) [8]

$$\Delta_\omega^{f\bar{f}}(Q^2)=\exp\left\{\int_{Q_0^2}^{Q^2}\frac{dQ'^2}{Q'^2}\frac{\alpha_s(Q^2)}{2\pi}\gamma_{qq}(\omega)\right\}\Delta_\omega^{f\bar{f}}(Q_0^2), \tag{2.3.7}$$

$$\begin{pmatrix}\Sigma_\omega(Q^2)\\ G_\omega(Q^2)\end{pmatrix}=\exp\left\{\int_{Q_0^2}^{Q^2}\frac{\alpha_s(Q^2)}{2\pi}\begin{pmatrix}\gamma_{qq}(\omega) & \gamma_{qG}(\omega)\\ \gamma_{Gq}(\omega) & \gamma_{GG}(\omega)\end{pmatrix}\right\}\begin{pmatrix}\Sigma_\omega(Q_0^2)\\ G_\omega(Q_0^2)\end{pmatrix} \tag{2.3.8}$$

(2.3.8) tells us one can, in principle, obtain PDFs for all $Q^2\gg\Lambda_{QCD}^2$ if experiments measures PDFs at some value.

2.4 Solution to DGLAP equations in small-x limit

Finding the most general solutions to the DGLAP equations draws much attention[11, 12]. We will, however, throughout this dissertation, content ourselves only with the

behavior of the evolution equation at small-x. We will see that the small-x tail reveals some unique features.

At small-x, the z-integral is enhanced at $z \to 0$ by P_{Gq} and P_{GG} which behave as $1/z$, while quark splitting functions are nonsingular. We therefore will neglect quark evolution. Also, P_{Gq} affects the gluon evolution through $\Sigma(x, Q^2)$, it will be neglected as well due to the lack of evolution of $\Sigma(x, Q^2)$ in (2.2.5). In consequence, at small-x limit, the nucleus becomes a gluon-dominated phase. This remarkable feature will be revisited in the discussions on small-x evolution in the following chapters.

Let us make a quantitative study on the DGLAP equations in this small-x limit. In fact, a *double logarithmic approximation* (DLA) is applicable since both $\ln(Q^2/\Lambda)$ and $\ln(1/x)$ set in to enhance the small parameter α_s, i.e., the resummation parameter becomes $\alpha_s \ln(1/x) \ln(Q^2/\Lambda)$.

$$Q^2 \frac{\partial G(x, Q^2)}{\partial Q^2} = \frac{\alpha_s(Q^2)}{2\pi} \int_x^1 \frac{dz}{z} \frac{2N_c}{z} G\left(\frac{x}{z}, Q^2\right) \tag{2.4.1}$$

It can be reduced to

$$\frac{\partial^2 xG(x, Q^2)}{\partial \ln(1/x) \partial \ln(Q^2/Q_0^2)} = \frac{\alpha_s(Q^2) N_c}{\pi} xG(x, Q^2) \tag{2.4.2}$$

It has the solution [8]

$$xG(x, Q^2) \sim \exp\left\{2\sqrt{\frac{N_c}{\pi\beta_2} \ln \frac{\ln(Q^2/\Lambda_{QCD}^2)}{\ln(Q_0^2/\Lambda_{QCD}^2)} \ln \frac{1}{x}}\right\} \tag{2.4.3}$$

DGLAP studies the effects of Q^2 evolution to parton distributions. The increase of resolution power unveils finer internal structure of the nucleon/nucleus target. The better the resolution, the smaller the partons the probe can tell, and smaller partons which previously serve as dressings on larger partons at lower resolution gradually manifest themselves along the path of evolution. In other words, large-Q^2 evolution stepwise uncovers partons previously hidden within a nucleon. Naively, the density inside the nucleon should turn higher, however, the system become more dilute, as predicted by

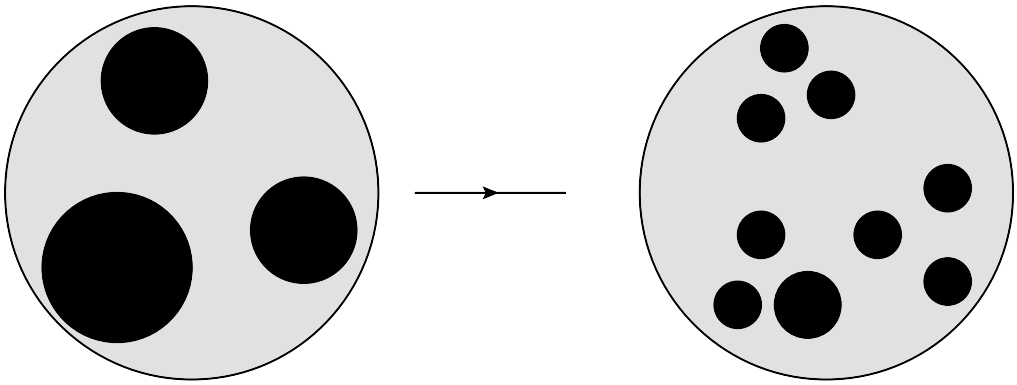

Figure 2.3 A schematic show about DGLAP evolution. The probed parton size turns smaller with growing resolution power Q^2.

DGLAP equation. This seems counter-intuitive, but let us recall that the Q is the measure of probe's resolution power and therefore the smallest detectable parton size is $1/Q$. On the other hand, an ultrarelativistic proton/nucleus has negligible longitudinal dimension. This makes $1/Q$ the smallest resolvable transverse parton size. The interaction cross section of the partons $\sim (\alpha_{em}/Q^2)$ while the total number of partons is $G(x, Q^2)$, thus the total interaction cross section of the partons is $(\alpha_{em}/Q^2)G(x, Q^2)$. $G(x, Q^2)$'s weak dependence on Q^2 makes the total interaction cross section of partons inside the nucleus fall rapidly as $\sim 1/Q^2$. In other words, the nucleus becomes dilute, see Fig. 2.3 for an illustrative picture.

We will get back to this problem when we discuss the small-x evolution. DGLAP predicts that Q^2 evolution at small-x counts more gluons, but under no circumstances should saturation effects occur inside the nucleus due to DGLAP evolution.

CHAPTER 3. High energy evolution and the BFKL equation

The DGLAP equation deals with the evolution of resolution scale, i.e., it can be viewed as a variant of RG equation along the line of Q^2. How about the evolution with respect to the x? Contrary to the Bjorken limit [34],[35], Regge-Gribov limit [27],[28],[29],[30] study the behavior of parton evolution with growing center of mass energy in fixed resolution power. It is often more convenient to use the variable y, called rapidity, related to x by $y = \ln(\frac{1}{x})$.

3.1 Two gluon exchange

High energy scattering event, each t-channeled particle with spin j contribute to the cross section a factor

$$s^{j-1}. \tag{3.1.1}$$

Each quark exchange in the t-channel contributes a factor $1/s$ to the cross section, counting in the quark contribution both in amplitude and its complex conjugate. In contrast, one gluon exchange furnishes s^0, i.e., no energy dependence. Therefore, quark contributions in the t-channel are suppressed at high energies. Let us consider the simplest case where a gluon is exchanged between two relativistic quarks moving in the opposite direction.

Note that throughout the calculation any other momentum scales are assumed much smaller than P_1^+ and P_2^-, where P_1 and P_2 are the momenta of two incoming quarks moving relativistically in "+" and "−" directions, respectively.

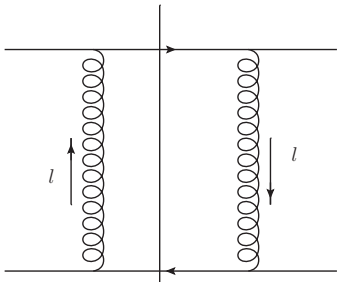

Figure 3.1 Interaction between two quarks through the change of one gluon.

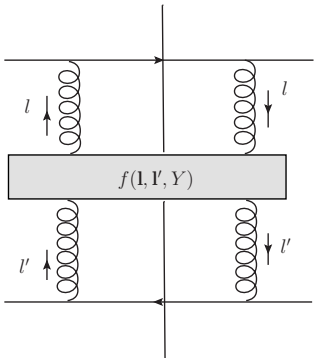

Figure 3.2 t-channel propagator

Born level quark-quark interaction has the following form [8]

$$\sigma^0_{qq\to qq} = \frac{2\alpha_s^2 C_F}{N_c}\int \frac{d^2\boldsymbol{l}}{(\boldsymbol{l}^2)^2} \tag{3.1.2}$$

3.2 BFKL evolution equation

At high energies, the resummation parameter is $\alpha_s \ln(1/x)$. The Born level result obtained in (3.1.2) will be corrected to include high order longitudinal logarithms. t-channel evolution become important. Let us incorporate the t-channel evolution into the a Green's function $f(\boldsymbol{l},\boldsymbol{l}',Y)$[10],

$$\sigma_{qq\to qq} = \frac{2\alpha_s^2 C_F}{N_c}\int \frac{d^2\boldsymbol{l}}{(\boldsymbol{l}^2)^2}\frac{d^2\boldsymbol{l}'}{(\boldsymbol{l}'^2)^2} f(\boldsymbol{l},\boldsymbol{l}',Y) \tag{3.2.1}$$

$f(\boldsymbol{l},\boldsymbol{l}',Y)$ encapsulates corrections to all orders with respect to the resummation parameter $\alpha_s Y$. $f(\boldsymbol{l},\boldsymbol{l}',Y)$ must satisfy the result from Born level approximation as its initial

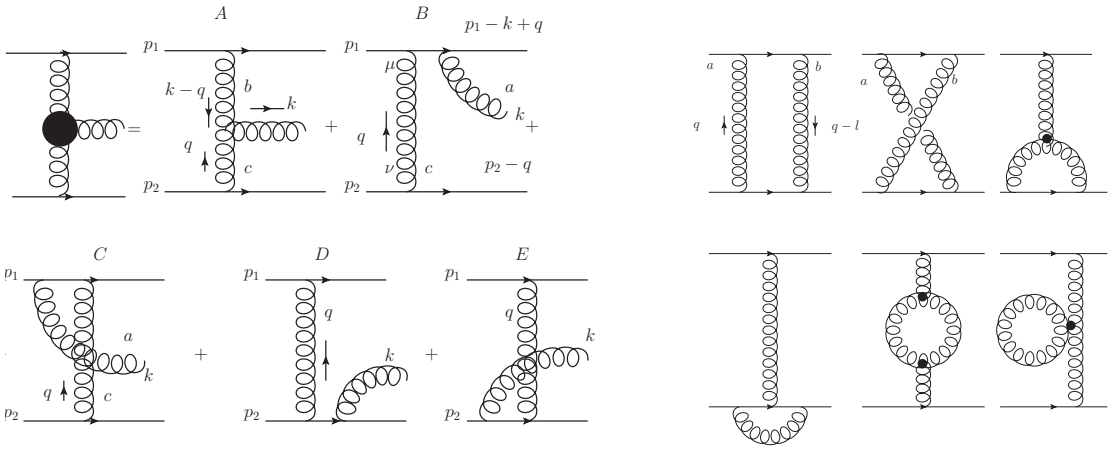

(a) Real corrections (Lipatov vertex) (b) virtual corrections

Figure 3.3 Real and virtual corrections to lowest nontrivial order to Born approximation.

condition for Y evolution.

$$f(\boldsymbol{l}, \boldsymbol{l}', Y = 0) = \delta^2(\boldsymbol{l} - \boldsymbol{l}') \tag{3.2.2}$$

Let us consider $qq \to qqG$, which is the simplest next order correction to $qq \to qq$. Let us consider the following corrections.

Real corrections can be cast into one single effective vertex. Detailed calculation shows that the real correction takes the form

$$f_1^{\text{Real}}(\boldsymbol{l}, \boldsymbol{l}', Y) = \frac{\alpha_s N_c}{\pi^2} Y \frac{1}{(\boldsymbol{l} - \boldsymbol{l}')^2} \tag{3.2.3}$$

Also, virtual corrections get the form

$$f_1^{\text{Virtual}}(\boldsymbol{l}, \boldsymbol{l}', Y) = f_0(\boldsymbol{l}, \boldsymbol{l}', Y) Y (-\frac{\alpha_s N_c}{2\pi^2}) \int d^2q \frac{\boldsymbol{l}^2}{\boldsymbol{q}^2 (\boldsymbol{q} - \boldsymbol{l})^2} \tag{3.2.4}$$

As a result we get

$$\begin{aligned} f(\boldsymbol{l}, \boldsymbol{l}', Y) =& f_0(\boldsymbol{l}, \boldsymbol{l}', Y) + \frac{\alpha_s N_c}{\pi^2} \int_0^Y dy \int \frac{d^2q}{(\boldsymbol{q} - \boldsymbol{l})^2} \\ & \times \left[f_0(\boldsymbol{q}, \boldsymbol{l}', Y) - \frac{\boldsymbol{l}^2}{2q^2} f_0(\boldsymbol{l}, \boldsymbol{l}', Y) \right] + O(\alpha_s^2) \end{aligned} \tag{3.2.5}$$

The energy evolution comes in two parts, one coming from real gluon emission, one from virtual correction. We will not going to the details, but the general outlines of that will be given.

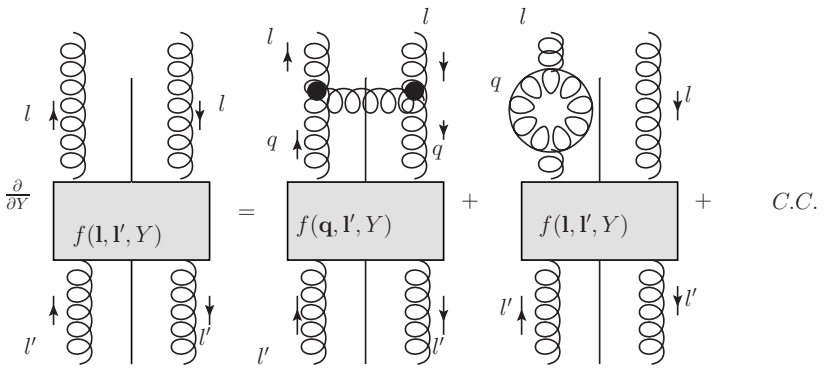

Figure 3.4 Diagrammatical interpretation of BFKL equation.

Taking Derivative with respect to Y, we arrive at

$$\frac{\partial f(\boldsymbol{l},\boldsymbol{l}',Y)}{\partial Y} = \frac{\alpha_s N_c}{\pi^2}\int \frac{d^2q}{(\boldsymbol{q}-\boldsymbol{l})^2}\left[f_0(\boldsymbol{q},\boldsymbol{l}',Y) - \frac{\boldsymbol{l}^2}{2q^2}f_0(\boldsymbol{l},\boldsymbol{l}',Y)\right] + O(\alpha_s^2). \tag{3.2.6}$$

In fact, this equation actually applied to all orders of resummation parameter $\alpha_s Y$. Readers interested in the treatment of high orders in this evolution equations are referred to [10], which presented a systematical treatment. Even though the details of this derivations are skipped, we will rederive this equation in a much simpler way from a different perspective in Chap. 4.

$$\frac{\partial f(\boldsymbol{l},\boldsymbol{l}',Y)}{\partial Y} = \frac{\alpha_s N_c}{\pi^2}\int \frac{d^2q}{(\boldsymbol{q}-\boldsymbol{l})^2}\left[f(\boldsymbol{q},\boldsymbol{l}',Y) - \frac{\boldsymbol{l}^2}{2q^2}f(\boldsymbol{l},\boldsymbol{l}',Y)\right]. \tag{3.2.7}$$

This equation is known as Balitskii-Fadin-Kuraev-Lipatov(BFKL) equation. The diagrammatical interpretations is as follows The first term corresponds to the corrections due to real gluon emissions while the second and third term virtual corrections.

3.3 Solutions to BFKL equation

The solution to BFKL equation is(taking into account initial condition)For details to solving the equation, refer to [10].

$$f(\boldsymbol{l},\boldsymbol{l}',Y) = \sum_{n=-\infty}^{\infty}\int_{-\infty}^{\infty}\frac{d\nu}{2\pi^2}\exp\left[\frac{\alpha_s N_c}{\pi}\chi(n,\nu)\right] l^{-1+2i\nu}l'^{-1-2i\nu}e^{in(\phi-\phi')} \tag{3.3.1}$$

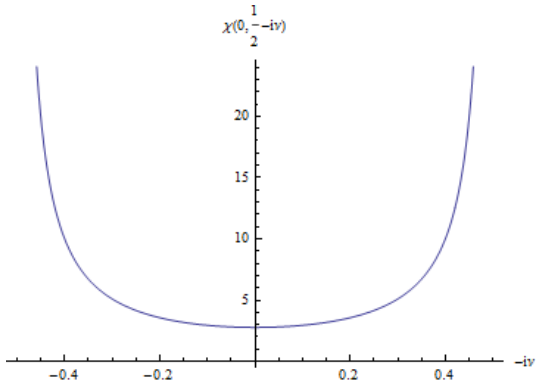

Figure 3.5 $\chi(0, \frac{1}{2} - i\nu)$as a function of $-i\nu$

where

$$\chi(n,\nu) = 2\psi(1) - \psi(\frac{1+|n|}{2} + i\nu) - \psi(\frac{1+|n|}{2} - i\nu) \tag{3.3.2}$$

and

$$\psi(x) = \frac{\Gamma'(x)}{\Gamma(x)} \tag{3.3.3}$$

No closed form of 3.3.1 can be found so far, yet it still sheds light to physics in its asymptotic regions. Often saddle point expansion is applied in ν on the exact integral-form solution. 3.3.1 can be rewritten as

$$f(\boldsymbol{l},\boldsymbol{l}',Y) = \sum_{n=-\infty}^{\infty} \int_{-\infty}^{\infty} \frac{d\nu}{2\pi^2} \frac{1}{ll'} \exp\left[\frac{\alpha_s N_c}{\pi}\chi(n,\nu) + 2i\nu \ln^2(l^2/l'^2)\right] e^{in(\phi-\phi')} \tag{3.3.4}$$

BFKL solution is often studied in *Diffusion limit* $l \sim l'$,the two transverse momenta are not too far off each other. The saddle points sits at $\nu = 0$. Due to large Y and $\chi(n = 0, \nu = 0) > \chi(n = 0, \nu > 0)$, we keep only the $n = 0$ term. $\chi(n = 0, \nu) \approx 4\ln 2 - 14\zeta 3)\nu^2$, we arrive at

$$f(\boldsymbol{l},\boldsymbol{l}',Y) \approx \frac{1}{2\pi^2 ll'} \sqrt{\frac{\pi}{14\zeta(3)\bar{\alpha}_s Y}} \exp\left\{(\alpha_P - 1)Y - \frac{\ln^2(l^2/l'^2)}{14\zeta(3)\bar{\alpha}_s Y}\right\} \tag{3.3.5}$$

where $\bar{\alpha_s} = \frac{\alpha_s N_c}{\pi}$ and

$$\alpha_P - 1 = \frac{4\alpha_s N_c}{\pi} \ln 2. \tag{3.3.6}$$

The subscript P stands for pomeron, a historical name denoting a collective gluon state in the t-channel at high energy hadron collisions. $\alpha_P - 1$ is called BFKL pomeron intercept

[31],[32]. The lowest order two-gluon exchange model make this intercept zero, i.e., no energy dependence of the cross section with center of mass energy, experimentally it was found that [49, 50]

$$\sigma^{\exp} \sim s^{0.08}. \tag{3.3.7}$$

Our result shows

$$\sigma^{\mathrm{BFKL}} \sim s^{\alpha_P - 1}. \tag{3.3.8}$$

It would be very illuminating to study BFKL equation in the *Double Logarithmic Approximation*(DLA), as what has been done when we treat the DGLAP equation. One might want to cross check whether the two equations converge in the limit of small-x and large Q^2. The large Q^2 limit corresponds to the case if $l \gg l'$. Without lose of generality, only $n = 0$ term in the series is retained. For $n \neq 0$ terms, they are suppressed by powers of $(l^2/l'^2)^{|n|}$. The saddle point sits at $\nu = \frac{i}{2}$ and the $\chi(0,\nu) \approx -\frac{i}{\nu - i/2}$, thus the saddle point $\nu = \frac{i}{2} - i\sqrt{\frac{\bar{\alpha_s} N_c}{\ln^2(l^2/l'^2)}}$. We get

$$f(\boldsymbol{l}, \boldsymbol{l}', Y) = \frac{1}{2\pi^{3/2} l^2} \frac{(\bar{\alpha_s} Y)^{1/4}}{\ln^{3/4}(l^2/l'^2)} \exp\left\{2\sqrt{\bar{\alpha_s} \ln^2(l^2/l'^2) Y}\right\} \tag{3.3.9}$$

It is easily seen that the exponents matches DGLAP in the DLA limit, the coefficients are different, though. This difference is due to the fact that gluon distribution function and t-channel Greens functions are two different quantities. To further illustrate how the BFKL affects the gluon distribution function, we define unintegrated gluon distribution function(UGDF)

$$\phi(x, Q^2) = \frac{\partial x G(x, Q^2)}{\partial Q^2} \tag{3.3.10}$$

It can be equivalently redefined in the LLA as

$$\phi(x, k^2) = \frac{\alpha_s C_F}{\pi} \int \frac{d^2 l}{l^2} f(\boldsymbol{k}, \boldsymbol{l}, Y = \ln(1/x)) \tag{3.3.11}$$

This definition can be justified diagrammatically from 3.6. This redefinition essentially absorbs the t-channel propagator into the wave function of the incoming quark. What

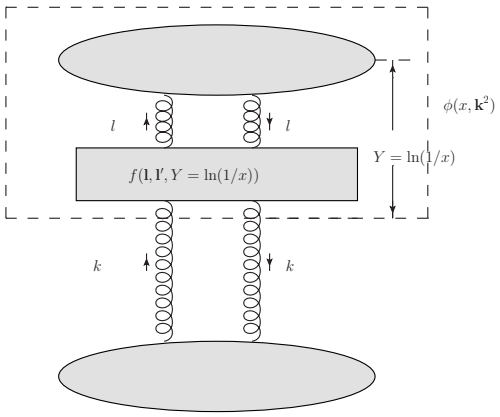

Figure 3.6 Diagrammatical illustration of unintegrated gluon distribution function (UGDF).

we would like to emphasize here this definition is, in fact, UV divergent. A single quark cannot exist in nature, so a more realistic model of proton would remedy the problem. From next section we would like to replace the quark by a more realistic model of proton,i.e., onium wave function. The word *onium* refers to a color dipole. The size of the dipole plays the role as UV cutoff for the incoming quark; moreover, the dipole wave function serves as a good base to write down proton wave function. We will get back to this problem in Chap. 4.

It can be seen that the $\phi(x, Q^2)$ satisfies BFKL equations,too.

$$\frac{\partial \phi(x, k^2)}{\partial \ln(1/x)} = \frac{\alpha_s N_c}{\pi^2} \int \frac{d^2 q}{(\boldsymbol{q} - \boldsymbol{l})^2} \left[\phi(x, q^2) - \frac{\boldsymbol{l}^2}{2q^2} \phi(x, k^2) \right]. \tag{3.3.12}$$

It has a similar solution

$$\phi(x, k^2) = \int_{-\infty}^{\infty} \frac{d\nu}{2\pi} C_\nu \exp\left[\frac{\alpha_s N_c}{\pi} \chi(0, \nu) \right] k^{-1+2i\nu} \Lambda^{-1-2i\nu} \tag{3.3.13}$$

Where C_ν is to be determined by initial condition. We do have an initial condition for t-channel Green's function as a delta function. However, the initial condition for UGDF has to be an input from outside. Gluon distribution at a given x has to be measured before the application of evolution equation. Similar to the discussion of the diffusion

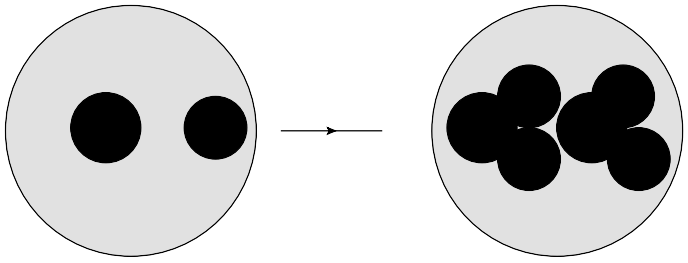

Figure 3.7 A schematic show of the effects of BFKL evolution in a proton. The BFKL evolution does not affect the size of the partons; the small-x evolution increase the number of the partons.

approximation for BFKL solution, we concludes that

$$\phi(x, k^2) \sim \left(\frac{1}{x}\right)^{\alpha_P - 1} \tag{3.3.14}$$

This is result of significant consequence.

The DGLAP equation shows that the nucleons become diluter with growing Q^2. As has been state above, BFKL and DGLAP has the same DLA behavior. However, we bear in mind that they are studying different evolutions. In BFKL, Q^2 is fixed, while x is free to approach zero. If x nears zero, i.e., the gluons become softer, the number follows a power law increase. However, the gluon size $r \sim 1/k$, eventually the gluons inside nucleus will occupy the entire space and begin overlapping each other, see Fig. 3.7 This phenomenon is known as gluon saturation at small-x.

BFKL predicts the growth of cross section with the energy, however, it is worthwhile pointing out that solution to BFKL equation violates a fundamental property known as *unitarity*–the probability for all possible final states must not be larger than unity. However, the partial amplitudes at given impact parameter $\boldsymbol{b}$ as predicted by the BFKL equation grows with energy faster than what is allowed by the unitary. Specifically, the partial amplitude for any scattering process at impact parameter $\boldsymbol{b}$ must not exceed 1.

Let $N(\boldsymbol{b})$ be the forward scattering amplitude for an arbitrary scattering process at impact parameter $\boldsymbol{b}$, then optical theorem dictates that

$$\sigma^{tot} = \int d^2b N(\boldsymbol{b}). \tag{3.3.15}$$

It can be shown that [54] that for the scattering for a point-like particle on a sphere of radius R, $\sigma^{tot} \leq 2\pi R^2$ holds. Then $N \leq 1$ must be satisfied.

Note that for $N = 1$, σ^{tot} reaches its upper bound $2\pi R^2$, i.e., the target becomes completely absorptive(black) and *black disk limit* is achieved. *

BFKL predicts that the total cross section is unbounded by the black disk limit. Therefore, the BFKL formalism is incomplete and some mechanism must come into play to bring down the growth rate. We will see in the next chapter that the problem no longer occur in the dipole approach.

* In this limit, elastic scattering and inelastic scattering each constitutes half of the total cross section. It should be understood that since the target is complete black except at the edge, its geometric size πR^2 contributes to the inelastic cross section, as expected. The other half of the total cross section πR^2 only comes from the scattering at edge of the target. The elastic contribution to the total cross section is purely a quantum effect and may not be drawn from classical analogies.

CHAPTER 4. Color dipole picture and small-x evolution

We studied the BFKL equation in the preceding chapter to characterize small-x evolution. It predicts a power law growth of the gluon density inside proton which violates unitary. It is natural to expect that higher-orders of BFKL small-x evolution would bring down the growth. However, due to extreme complexity of higher order calculations, no systematical way of resummation to all orders is known so far. As an alternative approach, the present chapter treats the problem in the color dipole framework and one would observe that the preservation of unitarity is inherent in this formalism.

A color dipole consists of quark and its anti-quark, and in the eikonal approximation it has a simple form in the mixed representation $(k^+, \boldsymbol{x})$,where k^+ stands for the "+" momentum of the color dipole while $\boldsymbol{x}$ is the transverse separation between the quark and anti-quark. In the eikonal approximation, the transverse coordinates of the quark(anti-quark) remain unaffected either after the emission of secondary partons. This leads to the factorization of one step of evolution from the existing onium wave functions, justifying an iterative treatment on the small-x evolution that will be used below to derive the evolution equation.

4.1 Classical dipole picture without energy evolution

4.1.1 Dipole-nucleon interaction

We discussed quark-quark interaction at high energies in Chap. 3. We have not explicitly pointed out that the calculated cross section is not finite. Now, instead of

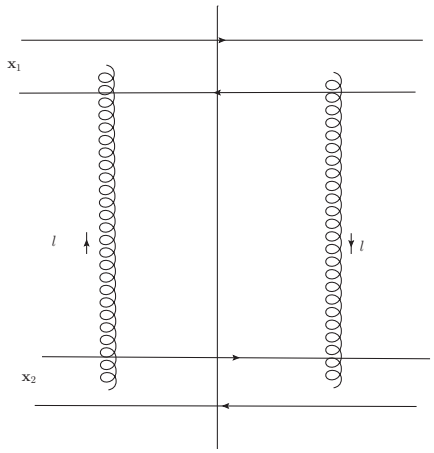

Figure 4.1 Dipole-dipole interaction.

considering quark-quark cross section, one would resort to a more realistic model for high energy scatterings. Quarks are confined in the colorless hadrons and nuclei, and the size of hadrons and nuclei offers natural IR cutoff to prevent the unlawful rapid growth of the cross section. For the time being, let us concentrate on dipole-dipole interaction.

The dipole-dipole cross section in the Born level reads [62]

$$\sigma^{dip+dip} = \frac{2\alpha_s^2 C_F}{N_c}\int \frac{d^2l}{(l^2)^2}(2 - e^{-i\boldsymbol{l}\cdot\boldsymbol{x}_{1\perp}} - e^{i\boldsymbol{l}\cdot\boldsymbol{x}_{1\perp}})(2 - e^{-i\boldsymbol{l}\cdot\boldsymbol{x}_{2\perp}} - e^{i\boldsymbol{l}\cdot\boldsymbol{x}_{2\perp}}) \tag{4.1.1}$$

It is a nontrivial result. It tells that dipole-dipole interactions are transverse.

Averaging over all the angular dependence, one gets

$$\left\langle \sigma^{dip+dip} \right\rangle = \frac{4\pi\alpha_s^2 C_F}{N_c} x_<^2 (\ln(x_>/x_<) + 1) \tag{4.1.2}$$

Our first approximation for dipole-nucleus interactions was modeled by lowest-order dipole-dipole interaction

$$\sigma^{dip+N} = \frac{2\pi\alpha_s^2 C_F}{N_c} x^2 \ln(\frac{1}{x^2\Lambda^2}) \tag{4.1.3}$$

In arriving at this formula, we made the assumption that the dipole size if perturbative, while the nucleon makes $x_> \sim 1/\Lambda$.

Quoting the result from last chapter, we have

$$\phi_{LO}^{onium}(x,k^2) = \frac{\alpha_s C_F}{\pi}\frac{2}{k^2}, \tag{4.1.4}$$

thus

$$xG_{LO}^{onium}(x,Q^2) = \frac{\alpha_s C_F}{\pi} 2\ln\frac{Q^2}{\Lambda^2}. \tag{4.1.5}$$

As a result, one can cast the dipole-nucleus cross sections as

$$\sigma^{dip+N} \approx \frac{\alpha_s \pi^2}{N_c} x^2 x G_N(x, \frac{1}{x^2}) \tag{4.1.6}$$

4.1.2 Multiple rescatterings in dipole-nucleus interaction

The study on dipole-dipole interactions may serve as a qualitative description and quantitative approximation on the cross section of the dipole-nucleon interaction. However, dipole-nucleus scattering deserves more considerations as multiple scatterings has to be properly taken care of.

Let us consider the case where $\alpha_s \ll 1$ while $\alpha_s^2 A^{1/3} \sim 1$. It is therefore, strictly speaking, only applicable to heavy nuclei. The lifetime of the dipole fluctuation τ is assumed much larger than the nucleus size.

We choose to work in the IMF where the dipole is fast moving in the "+" direction while the nucleus is at rest. Denoting the dipole momentum by q, one may express the coherent length of the dipole as $l_{coh} \sim 2/q^-$. Since $x = q^-/P^-$, where P stands for the momentum of the nucleus and $P^- = m$ in nucleus rest frame, then $q^- = xm$. Hence $l_{coh} \sim 2/(xm)$. One crucial observation is that for sufficiently small x, $l_{coh} \gg R$ –with R the nucleus size– the dipole is interacting with the entire nucleus simultaneously. Further, we will show that the transverse size of the dipole remains fixed throughout the interaction with the nucleus if this condition is satisfied. Let δr be the change of transverse due to interaction with the nucleus, then $\delta r \approx Rk_T/q^z$. Here, k_T denotes the typical relative transverse momentum between the quark and antiquark acquired through interactions with the nucleus and q^z is the longitudinal momentum of the dipole. then $\delta r/r =$

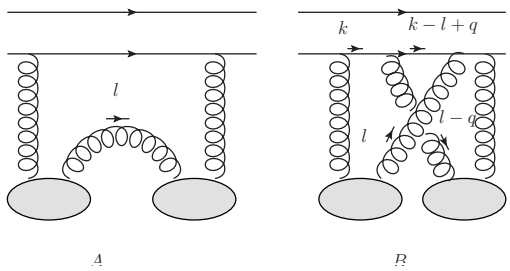

Figure 4.2 Diagrams that are suppressed

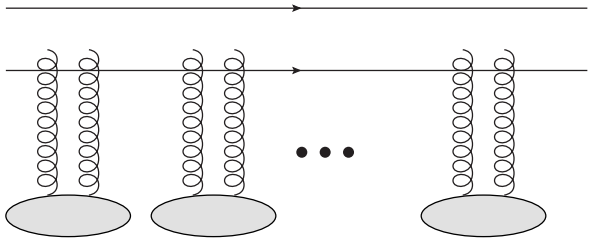

Figure 4.3 Multiple scatterings.

$(2R/q^+)(k_T/r)$. For $k_T \sim 1/r$ and note that $k_T^2 \sim q^+q^-$, then $\delta r/r \approx 2Rq^- = 2Rxm = 4R/l_{coh}$. Therefore, small enough x would naturally leads to the diagonalization of the scattering matrix, since the dipole does not change its size throughout the interaction. Since $Y = \ln(1/x) = \ln(P^-/q^-)$,this condition translates into $Y \gg \ln(1/mR)$. On the other hand, in the spirit of classical approximation, no leading order Bremsstrahlung should be evoked. It requires $\alpha_s Y \ll 1$. As a result, classical approximation applies to

$$\ln \frac{1}{mR} \ll Y \ll \frac{1}{\alpha_s} \tag{4.1.7}$$

It can be shown [76, 77] that in the covariant gauge $\partial_\mu A^\mu = 0$, for high energy scattering of a dipole off a heavy nucleus, the process in which two nucleons communicate and cross are suppressed(see Fig. 4.2). As a result, the dipole scatters off the nucleons in sequence of x^+. Glauber's assumption is realized in the covariant gauge of the gluons and in the frame we are working in. Keeping in mind that the cross section is frame-independent, we can paraphrase the above statement that covariant gauge is sufficient in

achieving the independence assumption of the individual nucleons. The dipole-nucleus scattering process now becomes easily tractable due to clear separation between any of the two consecutive dipole-nucleon interactions. In the spirit of eikonal approximation of the traversing dipole through the nucleus, the space-time picture of dipole-nucleus interaction is reducible into uncorrelated dipole-nucleon interactions; summing over the number of participating nucleons and taking into account symmetry factor, the S-matrix actually exponentiates. Nucleus thickness function is defined as

$$T(\boldsymbol{b}) = \int db^{+} \rho(\boldsymbol{b}), \tag{4.1.8}$$

where

$$\int d^{3}b \rho(\boldsymbol{b}) = A, \tag{4.1.9}$$

with A being the Atomic weight and $\rho(\boldsymbol{b})$ nuclear profile function. The meaning of $T(\boldsymbol{b})$ is now clear, it records the number density of nucleons for given transverse coordinate $\boldsymbol{b}$. Let us consider the case where the dipole interacts with n nucleons of the entire nucleus. The dipole-nucleon forward scattering amplitude is obtained from optical theorem

$$N^{dip+n}(b) = \frac{1}{2}\frac{d\sigma^{dip+N}}{d^{2}b} = \frac{1}{2}\frac{1}{S_p}\sigma^{dip+N} \tag{4.1.10}$$

where the S_p is the proton radius. The nucleus is modeled as being evenly distributed inside nucleus and a dilute system as well,

$$S(\boldsymbol{b}) = \sum_{n=1}^{A} \frac{1}{n!} S^{p}(\boldsymbol{b}) \tag{4.1.11}$$

As a result

$$S(\boldsymbol{x}, \boldsymbol{b}, Y = 0) = \exp\left[-\frac{\sigma^{dip+N}}{2} T(\boldsymbol{b})\right] \tag{4.1.12}$$

The relation between S-matrix and the forward scattering amplitude N is,

$$S = 1 - N \tag{4.1.13}$$

We eventually arrive at

$$N(\boldsymbol{x}, \boldsymbol{b}, Y = 0) = 1 - \exp\left[-\frac{\alpha_s \pi^2}{2N_c} T(\boldsymbol{b}) x^2 x G_N(x, \frac{1}{x^2})\right] \tag{4.1.14}$$

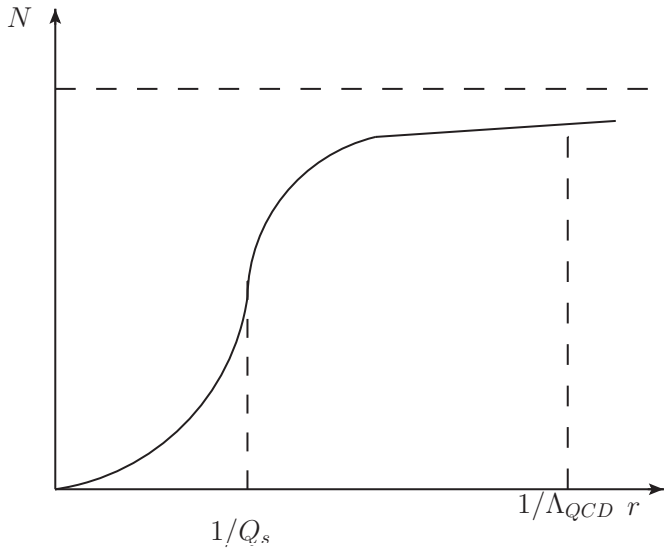

Figure 4.4 GGM formula (4.1.14) in two limits. For small dipole size r, N behaves as r^2; At large r, N saturates to unity. The characteristic scale distinguishing small and large r is $1/Q_s$, where Q_s is the saturation momentum. Λ_{QCD} denotes the border for perturbative calculations.

This is known as Glauber-Gribov-Mueller(GGM) model.

Defining saturation scale as the solution to the following equation

$$\frac{\alpha_s \pi^2}{2N_c} T(\boldsymbol{b}) \frac{1}{Q_s^2(\boldsymbol{b})} x G_N(x, Q_s^2(\boldsymbol{b})) = 1 \tag{4.1.15}$$

We know that if $x \sim 1/Q_s$, multiple scattering become important for dipole-nucleus scattering. One can see from this formula that the amplitude vanishes if the dipole size tends to zero. This phenomenon is known as color transparency. Also it solves unitarity problem and also naturally leads the black disk limit. GGM formula succeeded in accommodating the two limits, see Fig. 4.4.

Saturation momentum scales as $A^{1/3}$, thus the resummation parameter for GGM formalism is $\alpha_s A^{1/3}$.

4.2 Mueller's dipole model

The GGM model is energy-independent and would lose its predictive power at very high energies. At very high energies, the coherence length of the emitted gluons from the

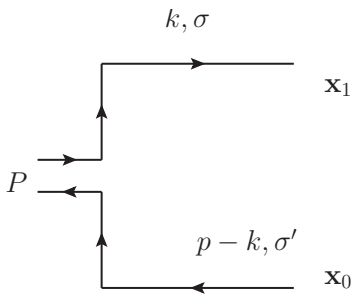

Figure 4.5 Onium wave function in its initial state.

quark (antiquark) making up the dipole becomes so large that it does not distinguish the x^+ difference between the individual nucleons. This contradicts the foundation of the GGM formulism–the independence assumption of the nucleons–and the gluons interacts with the nucleons simultaneously.

The computation of the multiple scattering taking into account energy evolution was not solved until large N_c limit[33] had been applied to QCD. In the large N_c limit, the emission of one single gluon can be viewed as the splitting of color dipole into two dipoles. The conservation of color is most easily illustrated in this limit. The greatest advantage of the large N_c limit is that all the non-planar diagram are suppressed by $\frac{1}{N_c^2}$ only planar diagrams contribute.

Let us transform the light-cone wave function into dipole picture

$$\Psi^{(0)}_{\sigma\sigma'}(\boldsymbol{x}_{10}, z) = \int \frac{d^2k}{(2\pi)^2} e^{i\boldsymbol{k}\cdot\boldsymbol{x}_{10}} \Psi^{(0)}_{\sigma\sigma'}(\boldsymbol{k}, z) \tag{4.2.1}$$

where x_{10} is the dipole size, see Fig. 4.5 for the detailed notation. The dipole wave function is normalized to unity.

$$\int_0^1 \frac{dz}{z(1-z)} \int \frac{d^2x_{10}}{2(2\pi)} \sum_{\sigma\sigma'} |\Psi^{(0)}_{\sigma\sigma'}(\boldsymbol{x}_{10}, z)|^2 = \int_0^1 \frac{dz}{z(1-z)} \int \frac{d^2k}{2(2\pi)^3} \sum_{\sigma\sigma'} |\Psi^{(0)}_{\sigma\sigma'}(\boldsymbol{k}, z)|^2 = 1 \tag{4.2.2}$$

Now let us consider the emission of on gluon from the dipole, and we choose light-cone

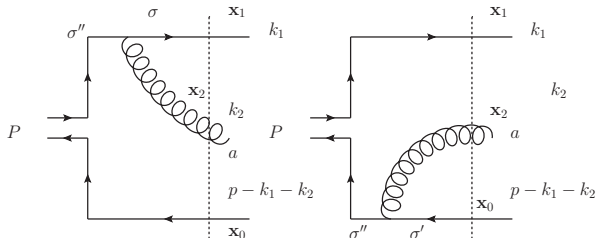

Figure 4.6 Lowest order gluon emission from the initial onium state.

gauge $A^+ = 0$. One reaches [8]

$$\Psi^{(1)}_{\sigma\sigma'}(\boldsymbol{k}_1, \boldsymbol{k}_2, z_1, z_2) = \frac{gt^a\theta(k_2^+)}{k_2^- + k_1^+(p-k_1-p_2)^- - p^-} \sum_{\sigma''=\pm 1} [\frac{\bar{u}_\sigma(k_1)\gamma\cdot\epsilon^*_\lambda(k_2)u_{\sigma''}(k_1+k_2)}{k^+ + k^+}\Psi^{(0)}_{\sigma\sigma'}(\boldsymbol{k}_{1\perp}+\boldsymbol{k}_{2\perp}, z_1+z_2) - \frac{\bar{v}_{\sigma''}(p-k_1)\gamma\cdot\epsilon^*_\lambda(k_2)v_{\sigma'}p-k_1-k_2}{p^+-k^+}\Psi^{(0)}_{\sigma\sigma'}(\boldsymbol{k}_{1\perp}, z_1)] \tag{4.2.3}$$

See Fig. 4.6 for Mueller's notations, there the dashed vertical lines stand for energy denominators in LCPT.

We assume the emitted gluon carries only very small momentum fraction of the dipole, which translates to $z_2 \ll z_1, 1-z_1$. The very soft gluon momentum renders a great simplifications to the energy denominator.

$$k_2^- + k_1^+(p-k_1-p_2) \approx \frac{1}{k_2^-} = \frac{k_2^+}{k_{2\perp}^2} \tag{4.2.4}$$

It can be shown that real emission of gluon Fig. 4.6 gives

$$\sum_{\sigma,\sigma',\lambda,a} |\Psi^{(1)}_{\sigma\sigma'}(\boldsymbol{x}_{10}, \boldsymbol{x}_{20}, z_1, z_2)|^2 = \frac{4\alpha_s C_F}{\pi}\frac{x_{10}^2}{x_{20}^2 x_{21}^2}\sum_{\sigma,\sigma'}|\Psi^{(0)}_{\sigma\sigma'}(\boldsymbol{x}_{10}, z)|^2 \tag{4.2.5}$$

Here, $\boldsymbol{x}_2$ is the transverse coordinate of the emitted gluon and z_2 its longitudinal momentum fraction of the original dipole. The phase space for gluon emission is

$$\int_{z_0}^{minz_1,1-z_1}\frac{dz_2}{z_2}\int\frac{d^2x_2}{4\pi} \tag{4.2.6}$$

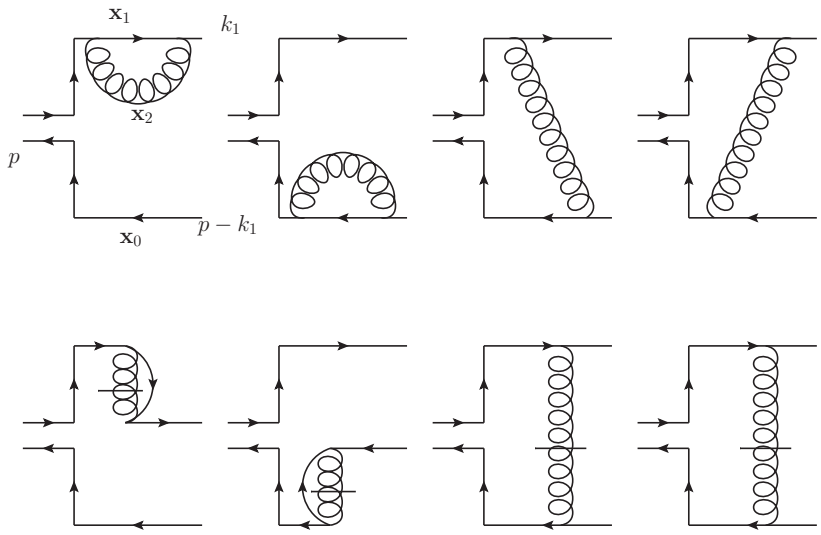

Figure 4.7 Virtual corrections to the lowest order gluon emission.

where z_0 is lower cutoff determined by the particular process and is not highly relevant in the present discussion.

The probability of finding one gluon in the dipole wave function is therefore [61, 62, 63]

$$\int_{z_0}^{minz_1,1-z_1}\frac{dz_2}{z_2}\int\frac{d^2x_2}{4\pi}\sum_{\sigma,\sigma',\lambda,a}|\Psi^{(1)}_{\sigma\sigma'}(\boldsymbol{x}_{10},\boldsymbol{x}_{20},z_1,z_2)|^2 = \int_{z_0}^{minz_1,1-z_1}\frac{dz_2}{z_2}\int d^2x_2\frac{\alpha_s C_F}{\pi^2}\frac{x_{10}^2}{x_{20}^2x_{21}^2}\sum_{\sigma,\sigma'}|\Psi^{(0)}_{\sigma\sigma'}(\boldsymbol{x}_{10},z)|^2 \tag{4.2.7}$$

An important observation of this equation is that the probability of gluon emission completely factors out the wave function of the parent dipole. Specifically, the emission probability for one gluon at $\boldsymbol{x}_2$ is equal to the probability if finding a dipole of size x_{10} times the probability of the dipole to emit a gluon at $\boldsymbol{x}_2$ (see [8] for more detailed explanations). This also justifies the reason why transverse coordinate representation is preferred, as the emission of a gluon does not alter the trajectory of the original dipole. In fact, gluon emission can be real, as explained above, or, it can be virtual, as shown in Fig. 4.7. We will not elaborate in detail and we refer to interested readers to the original

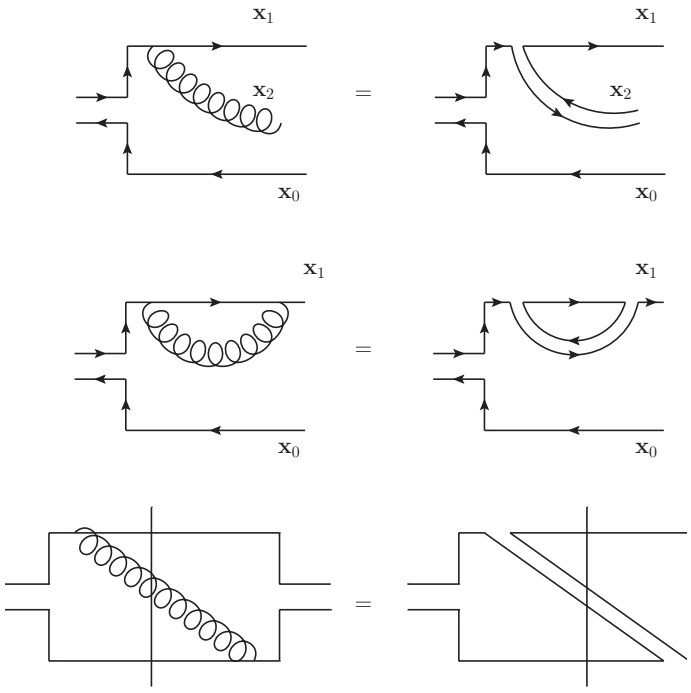

Figure 4.8 Gluon-dipole dualism

work of Mueller [61, 62, 63]. Presented below are the general ideas of dipole model. A single quark(or anti-quark) emits a parton, and this parton emits a softer parton, which then emits another parton. The birth of each parton in the large N_c limit contributes to the total number of dipoles by one, see Fig. 4.8. The iterative emission forms a cascade of dipoles. Note that each step of emission is eikonal,i.e., The trajectory of the emitter is unchanged. The dipole cloud grows until the desired rapidity is reached.

Since only planar diagrams are allowed, dipoles belonging to the same ancestry do not interact; we can build our interaction of the original dipole with the target sheerly by the superposition of the interactions of all its living descendants with the target. The disentanglement inside the projectile is a major breakthrough in the path of simplification to high energy QCD scattering. N_c corrections beyond the leading order is an unsolved problem. However, numerical studies[131, 132, 133] suggest that high energy process might not be far off the N_c limit.

4.3 Balitsky-Kovchegov evolution equation

GGM model serves as the initial condition as the dipole starts to evolve along the rapidity. As the energy increases, evolution effects has to be taken into account. Following Mueller's dipole approach, the problem is cast in the transverse momentum space with eikonalization of all the dipoles assumed and in the large N_c limit. We now explain the general idea that leads to this evolution equation. Let us start with a single dipole. The dipole can emit a gluon within a finite rapidity range. As is explained in Sec. 4.2 gluon emission from a dipole is equivalent to the splitting of the parent color dipole to two daughter color dipoles. The typical interaction time is much shorter than the dipole lifetime. The split dipole, upon interaction, becomes two real daughter dipoles. Otherwise, the dipole will merge back to the parent dipole. This split and merge corresponds to a virtual gluon. Both real and virtual gluons must be included within the dipole evolution.

The S-matrix of dipole-nucleus interaction evolves with respect to Y upon dipole splitting and is iterative. Real gluon emission may occur either before or after the interaction with the nucleus. For virtual gluons, the parent dipole interacts with the nucleus before or after the lifecycle of virtual gluon emission and the subsequent absorpsion.

Each dipole interacts with the heavy nucleus target via two-gluon exchange in multiple scattering in the classical limit, i.e., GGM formula describes the interaction between each dipole with the heavy nucleus.

$$S_0(\boldsymbol{r}_j, \boldsymbol{b}_j) = \exp\left[-T(\boldsymbol{b})\frac{\sigma^{dip+A}}{2}\right] \tag{4.3.1}$$

is the two-gluon exchange forward scattering S-matrix element(GGM), where $T(\boldsymbol{b})$ is the nucleus thickness function satisfying

$$\int d^2bT(\boldsymbol{b}) = A \tag{4.3.2}$$

We thus arrive at [8]

$$S(\boldsymbol{r}_{10}, \boldsymbol{b}_{10}) = 1 + \sum_{n=1}^{\infty}\frac{1}{n!}\int\prod_{j=1}^{n} d^2b_j d^2r_j \frac{\Phi^{[n]}(\{\boldsymbol{r}_k, \boldsymbol{b}_k\}_{k=1}^n, Y)}{\Phi^{(0)}(\boldsymbol{x}_{10}, \boldsymbol{b}_{10})}\prod_{l=1}^{n} S_0(\boldsymbol{r}_l, \boldsymbol{b}_l) \tag{4.3.3}$$

Note that in arriving at this, we follow the Kovchegov's notations, in which $\Phi^{[n]}(\{\boldsymbol{r}_k, \boldsymbol{b}_k\}_{k=1}^n, Y)$ represents the wave function of n-dipoles; while $\Phi^{(0)}(\boldsymbol{x}_{10}, \boldsymbol{b}_{10})$ is the initial dipole wave function. Readers interested in detailed derivations are referred to [8].

Noticing that 1 is included in the summation series since we are using the S-matrix instead of N, as the non-interacting amplitudes also contribute its share.

Since

$$\Phi^{[n+1]}(\{\boldsymbol{r}_k, \boldsymbol{b}_k\}_{k=1}^n, Y) = \frac{\bar{\alpha}_s N_c}{2\pi^2}\int d^2x_{j+1}\frac{x_{j+1}}{x_{j+1}x_{j+1}}\Phi^{[n]}(\{\boldsymbol{r}_k, \boldsymbol{b}_k\}_{k=1}^n, Y) \tag{4.3.4}$$

As a result, the evolution for wave functions gets the form

$$\Phi^{[n+1]}(\{\boldsymbol{r}_k, \boldsymbol{b}_k\}_{k=1}^{n+1}, Y) = \frac{\bar{\alpha}_s N_c}{2\pi^2}\int d^2r_{n+1}\frac{(\boldsymbol{r}_n)^2}{r_{n+1}^2(\boldsymbol{r}_n^2 - \boldsymbol{r}_{n+1})^2}\Phi^{[n]}(\{\boldsymbol{r}_k, \boldsymbol{b}_k\}_{k=1}^n, Y) \tag{4.3.5}$$

Taking derivatives on both sides of 4.3.3 furnishes an evolution equation for S

$$\frac{\partial}{\partial Y}S(\boldsymbol{x}_{10},\boldsymbol{b},Y)=\frac{\alpha_s N_c}{2\pi^2}\int d^2x_2\frac{x_{10}^2}{x_{20}^2x_{21}^2}\Big[S(\boldsymbol{x}_{12},\boldsymbol{b}+\frac{\boldsymbol{x}_{20}}{2},Y)S(\boldsymbol{x}_{20},\boldsymbol{b}+\frac{\boldsymbol{x}_{21}}{2},Y)-S(\boldsymbol{x}_{10},\boldsymbol{b},Y)\Big] \tag{4.3.6}$$

Dipole-nucleus forward scattering amplitude relates to its S-matrix by $N=1-S$, we conclude that

$$\begin{aligned}\frac{\partial}{\partial Y}N(\boldsymbol{x}_{10},\boldsymbol{b},Y)=\frac{\alpha_s N_c}{2\pi^2}\int d^2x_2\frac{x_{10}^2}{x_{20}^2x_{21}^2}\\ [N(\boldsymbol{x}_{12},\boldsymbol{b}+\frac{\boldsymbol{x}_{20}}{2},Y)+N(\boldsymbol{x}_{20},\boldsymbol{b}+\frac{\boldsymbol{x}_{21}}{2},Y)-N(\boldsymbol{x}_{10},\boldsymbol{b},Y)\\ -N(\boldsymbol{x}_{12},\boldsymbol{b}+\frac{\boldsymbol{x}_{20}}{2},Y)N(\boldsymbol{x}_{20},\boldsymbol{b}+\frac{\boldsymbol{x}_{21}}{2},Y)]\end{aligned} \tag{4.3.7}$$

This is Balitsky-Kovchegov(BK) equation [78, 76]. This evolution equation constitutes the basis of our discussions in this dissertation. A few words about its resummation parameter:(i)It treats the small-x evolution in the leading logarithmic approximation(LLA) which resums over $\alpha_s\ln(1/x)$; (ii)This formalism is applicable only in the large N_c limit; (iii)Heavy nucleus is essential in arriving at BK equation, only terms enhanced by $A^{1/3}$ are included. Therefore, the resummation parameter for BK equation is $\alpha_s A^{1/3}N_c^2\ln(1/x)$.

The general idea of BK equation can be explained as follows. The splitting of the parent dipole into two daughter dipoles affects the way how the nucleus interacts with the original dipole–the nucleus may interact with any of the two daughter dipoles, or, alternatively, with the parent dipole if the dipole recombines into the parent dipole(virtual corrections). These three possible processes together contribute. One can see that aside from the linear evolution term similar to our discussion in BFKL equation, a quadratic term emerges. It is the simultaneous interaction of the two daughter dipoles with the nucleus. This quadratic term tells that the evolution of the two daughter dipoles are actually not independent and, further, "-" sign implies that linear contributions must be brought down by nonlinear term.

4.3.1 Solution to the BK equation

No closed form of analytical solution has been found so far fitting all dipole sizes. Still, the equation can be solved in asymptotics.

If one assumes the b-dependence of the forward scattering amplitude is weak in the for scales of the order of dipole size $\boldsymbol{x}_{10}$, we may suppress its dependence as a first approximation to help obtain analytical resolutions. This is true in the large-A limit. b-dependence may be incorporated into models, as we will see later. Further, the fact that nucleus is isotropic enables us to suppress the angular dependence of N [8],

$$\frac{\partial}{\partial Y}N(x_{10},Y) = \frac{\alpha_s N_c}{2\pi^2}\int d^2x_2 \frac{x_{10}^2}{x_{20}^2 x_{21}^2}[N(x_{12},Y) + N(x_{20},Y) - N(x_{10},Y) - N(x_{12},Y)N(x_{20},Y)]. \tag{4.3.8}$$

4.3.1.1 Linear evolution

In the dilute region where the $N \ll 1$,the quadratic term vanishes and the equations turns linear.

$$\frac{\partial}{\partial Y}N(x_{10},Y) = \frac{\alpha_s N_c}{2\pi^2}\int d^2x_2 \frac{x_{10}^2}{x_{20}^2 x_{21}^2}[N(x_{12},Y) + N(x_{20},Y) - N(x_{10},Y)] \tag{4.3.9}$$

It is the equivalence of BFKL equation in the coordinate space. Expanding the forward scattering amplitude in the Mellin space, we get

$$N(r,Y) = \int_{-\infty}^{\infty} d\nu C_\nu \exp[\bar{\alpha}_s \chi(0,\nu)Y + (1+2i\nu)\ln(rQ_{s0})] \tag{4.3.10}$$

We can apply the same approximations like what we have for BFKL equation in the momentum space–diffusion approximation and double logarithmic approximation. Observing the fact that dipole transverse size and momentum are conjugate to each other.

Fig. 3.5 tells that the function $\chi(0,\nu)$ is rather flat throughout the region $\frac{-1}{2} < -i\nu < \frac{1}{2}$ unless close to the boundaries. Therefore $\chi(0,\nu)$ can be modeled near $-\frac{i}{2}$ by a simple function while retaining its original form elsewhere.

DLA corresponds to the region where $rQ_{s0} \ll 1$. $\ln(rQ_{s0})$ contributes a large logarithm. Since χ behaves away from the vicinity of $\nu = 0$ as $\chi(0,\nu) \approx \frac{2}{1-2\nu}$, one gets the saddle point

$$\nu_{DLA} = \frac{-i}{2}(1 - \sqrt{\frac{2\bar{\alpha}_s Y}{\ln(1/rQ_{s0})}}). \tag{4.3.11}$$

Saddle point approximation yields

$$N(r,Y) = (rQ_{s0})^2 C_{\nu_{DLA}}. \tag{4.3.12}$$

The solution in DLA parallels the discussion on BFKL in this region. However, diffusion approximation needs more elaboration. $r \lesssim 1/Q_{s0}$ is the region of interest. Different from the case in BFKL, we may not push it arbitrarily close to the boundary $r = 1/Q_{s0}$ as nonlinear term would come into play for large dipole sizes. r is assumed large compared with DLA region, but still smaller than $1/Q_{s0}$. Define

$$\phi(\nu) = \bar{\alpha}_s \chi(0,\nu) Y + (1 + 2i\nu)\ln(rQ_{s0}) \tag{4.3.13}$$

Saddle point is the steepest descend of ϕ and is found with the equation

$$\phi'(\nu_{sp}) = \bar{\alpha}_s \chi'(0,\nu_{sp}) + 2i\ln(rQ_{s0}) = 0 \tag{4.3.14}$$

Therefore in this approximation, we get

$$N(r,y) \sim (rQ_{s0})^{1+2i\nu} \exp \bar{\alpha}_s \chi(0,\nu_{sp}) Y \tag{4.3.15}$$

We can see that the increase of dipole size and rapidity both contribute to the growth of the forward amplitude. It is often of great interest to study when the nonlinear effects become important, i.e.,$N(r,Y) \sim 1$. Define saturation scale by the solution of the following equation [8],

$$N(r = \frac{1}{Q_s(Y)}, Y) = \text{constant} \tag{4.3.16}$$

$Q_s(Y)$ is the characteristic line in the (r,Y) plane in which the dipole size r propagates along rapidity Y to keep amplitude constant. Set $N = 1$ helps us qualitatively keep

track of the demarcation in which the nonlinear term in BK equation has significant contribution.

$$\bar{\alpha}_s \chi(0,\nu_{sp}) Y + (1+2i\nu_{sp}) \ln(\frac{Q^{s0}}{Q_s Y}) = 0 \tag{4.3.17}$$

We get

$$Q_s(Y) = Q_{s0} \exp[\bar{\alpha}_s \frac{\chi(0,\nu_{sp})}{1+2i\nu_{sp}} Y] \tag{4.3.18}$$

This saddle point can actually be explicitly solved if we combine (4.3.14) and (4.3.17). One gets

$$\frac{\chi'(0,\nu_{sp})}{\chi(0,\nu_{sp})} = \frac{2i}{1+2i\nu_{sp}} \tag{4.3.19}$$

Therefore [56]

$$\nu_0 = -0.1275i. \tag{4.3.20}$$

We now arrive at

$$Q_s(Y) = Q_{s0} \exp(2.44\bar{\alpha}_s Y). \tag{4.3.21}$$

It is worthwhile studying the behavior of $N(r,Y)$ near the saturation region. Expressing Y in terms of Q_s and plugging back to 4.3.10, one arrives

$$N(r,Y) \sim (rQ_{s0})^{1+2i\nu_{sp}} \left(\frac{Q_s(Y)}{Q_{s0}}\right)^{(1+2i\nu_0)\chi(0,\nu_{sp})/\chi(0,\nu_0)} \tag{4.3.22}$$

Since only the region close to saturation is considered, we can approximate ν_{sp} by ν_0. We get

$$N(r,Y) \sim [rQ_s(Y)]^{(1+2i\nu_0)} \tag{4.3.23}$$

N is a function of a dimensionless variable rQs. This result is called extended geometric scaling [151, 135].

4.3.1.2 Nonlinear region and geometric scaling

We now consider a case in which $r \gg 1/Qs(Y)$. Dipole size become sufficiently large that $N(r,Y)$ nears unity.

Set

$$S = 1 - N, \tag{4.3.24}$$

Neglecting quadratic terms of S as it is assumed small, one gets [146]

$$\frac{\partial S(x_{10}, Y)}{\partial Y} = -\frac{\bar{\alpha}_s N_c}{2\pi^2} \int d^2x_2 \frac{x_{10}^2}{x_{20}^2 x_{21}^2} S(x_{10}, Y). \tag{4.3.25}$$

As what have done in solving BK equation, we have assumed an isotropic nucleus to suppress angular dependence of dipoles. The UV divergence is remedied by imposing $1/Q_s$ as the lower cutoff. We get

$$\frac{\partial S(x_{10}, Y)}{\partial Y} = -2\bar{\alpha}_s \ln[x_{10} Q_s(Y)] S(x_{10}, Y) \tag{4.3.26}$$

By introducing a new variable

$$\xi = \ln[r^2 Q_s^2(Y)], \tag{4.3.27}$$

one gets

$$\frac{\partial S}{\partial \xi} = -\frac{1 + 2i\nu_0}{2\xi(0, \nu_0)} \xi S. \tag{4.3.28}$$

Solving this equation, one arrives at [146]

$$S(\xi) = S_0 \exp[\frac{1 + 2i\nu_0}{2\xi(0, \nu_0)} \xi^2]. \tag{4.3.29}$$

Getting back to the convention for N leads to

$$N(\xi) = 1 - S_0 \exp[\frac{1 + 2i\nu_0}{2\xi(0, \nu_0)} \xi^2]. \tag{4.3.30}$$

This is Levin-Tuchin formula [146]. The sole dependence of N on the dimensionless variable ξ is called *geometric scaling*. All the dependence of N on r and Y are encoded in the variable ξ. Two important observations should be noted on the solution to BK equation.

- In dilute regimes, the cross section grows as a power law with center of mass energy, which is hinted by the famous pomeron intercept, even though the analytic result is far larger than the experimental results.

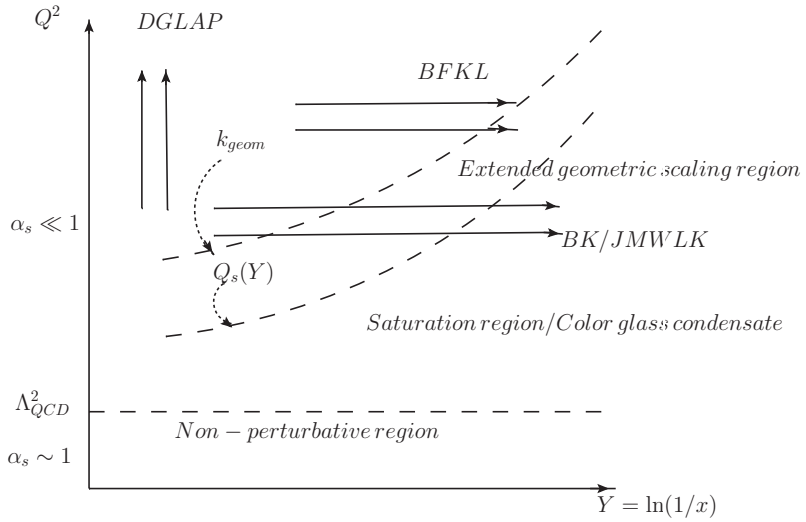

Figure 4.9 Phase diagram for different evolutions.

- The naturally occurring quadratic term preserves unitarity.

Let us close this chapter by a phase diagram that describes the applicability regimes of different evolution equations.

PART II

Phenomenological applications

CHAPTER 5. Deep inelastic scattering

5.1 Basic concepts in DIS

Deep inelastic process is the high energy process in which a lepton scatters off a nucleus/proton target via the emission of virtual photon by the incoming lepton. The larger the momentum transfer of the lepton, the deeper the virtual photon probes inside the target. The advantage of DIS over heavy ion collisions is that one will be able to study the nucleus directly, provided that the energies scales are large enough to match the required precision. Two distinctive energy scales come into play, the longitudinal energies scales and the transverse scales. To get a closer look at the DIS, we first need to introduce kinematic variables commonly used in DIS.

DIS is typically characterized with the following kinematic variables [9],[37]. Note that they are all Lorentz invariants and has clear interpretations in particular frames.

- Collision energy squared $s = (p + k)^2 = 4E_pE_e$
- Squared energy transfer $Q^2 = -q^2 = -(k - k')^2$. t-channel DIS is often approximated as the tree level one-photon exchange and thus Q^2 is equal to photon virtuality.
- Bjorken variable $x_B = \frac{Q^2}{2p\cdot q}$. In the IMF, it equals the momentum fraction of the proton carried by the quark struck by the virtual photon. $0 < x < 1$ for ep collisions. From now on, we will use x throughout the dissertation.
- Inelasticity $y = \frac{q\cdot p}{k\cdot p}$. It is interpreted as the momentum fraction of the incoming

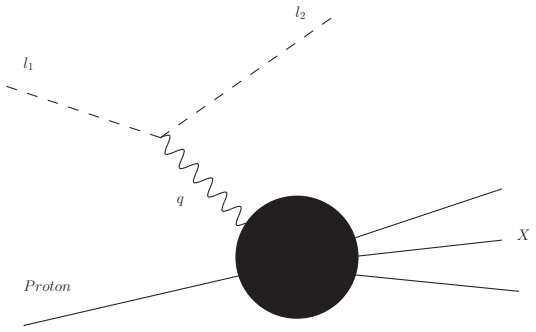

Figure 5.1 Deep Inelastic Scattering.

lepton carried by the virtual photon measured in the rest frame of the proton. $0 < y < 1$.

- Energy squared in the $\gamma^* p$ system $W^2 = (p+q)^2 = M^2 + Q^2(\frac{1}{x} - 1)$, where M is the proton mass.

- Energy lost by the incoming lepton $\nu = \frac{p \cdot q}{M}$ in proton rest frame.

Note that $Q^2 = xys$, neglecting the lepton mass and proton mass at very high energies.

The DIS cross section for the process $l + N \to l' + X$(N stands for either a nucleon or a nucleus) in the one photon exchange approximation can be cast into [37]

$$\frac{d^2\sigma}{dxdQ^2} = \frac{4\pi\alpha_{em}^2}{xQ^4}\left[\left(1 - y + \frac{y^2}{2}\right)F_2(x,Q^2) - \frac{y^2}{2}F_L(x,Q^2)\right] \tag{5.1.1}$$

In fact, *reduced cross section* is more often used, which is defined as

$$\sigma_r = \left(\frac{d^2\sigma}{dxdQ^2}\right)\frac{xQ^4}{2\pi\alpha_{em}^2[1+(1-y)^2]} = F_2(x,Q^2) - \frac{y^2}{1+(1-y)^2}F_L(x,Q^2) \tag{5.1.2}$$

The polarization vectors of the virtual photon may be written as [46]

$$\begin{aligned} \epsilon_T^\lambda &= (0,0,\boldsymbol{\epsilon}^\lambda), \\ \epsilon_L &= (\frac{q^+}{Q}, \frac{Q}{q^+}, \mathbf{0}), \end{aligned} \tag{5.1.3}$$

which decompose the photon propagator into [8]

$$g_{\mu\nu} - \frac{q_\mu q_\nu}{q^2} = -\sum_{\lambda=\pm1} \epsilon^{\lambda}_{T,\mu}\epsilon^{\lambda *}_{T,\nu} + \epsilon^{\lambda}_{L,\mu}\epsilon^{\lambda *}_{L,\nu}. \tag{5.1.4}$$

Throughout this dissertation, we will be concentrating on the subprocess of DIS: $\gamma^* + N \to X$. Structure functions are related to longitudinal photon cross section and transverse photon cross section by

$$\begin{aligned} F_2(x,Q^2) &= \frac{Q^2}{4\pi^2\alpha_{em}}\sigma^{\gamma^* A}_{tot} = \frac{Q^2}{4\pi^2\alpha_{em}}(\sigma^{\gamma^* A}_T + \sigma^{\gamma^* A}_L) \\ 2xF_1(x,Q^2) &= \frac{Q^2}{4\pi^2\alpha_{em}}\sigma^{\gamma^* A}_T \end{aligned} \tag{5.1.5}$$

The F_L is related to F_1 and F_2 by

$$F_L(x,Q^2) = F_2(x,Q^2) - 2xF_1(x,Q^2) = \frac{Q^2}{4\pi^2\alpha_{em}}\sigma^{\gamma^* A}_L \tag{5.1.6}$$

This is supposed to be zero for real photon, however, virtual photon contains longitudinal polarization.

Bjoken first proposed that for fixed x, the structure functions is flat with respect to Q^2 [14]. In the 1960s, the prevailing picture about a proton is a continuum of charge distribution. If the inside of proton is a continuum of distribution, the harder the scattering is, the less charge would be probed. Then the structure function should fall with increasing resolution scale. However, the SLAC-MIT experiment showed that the structure function within its energy scanning range does not vary with the momentum transfer Q^2.Instead, this phenomenon is best explained by naive parton model, proposed first by Feynman. Feynman parton model states that proton builds on top of point-like particles, called partons. It is therefore insensitive to the resolution power of the external electro-magnetic probe.

It turns out Bjorken scaling is not exact. The Feynman's naive parton model is the result of the active degrees of freedom at low energies. However, at high center of mass energies $\sqrt{s}$(small-x), deviations from the Q^2-scaling due to evolution become

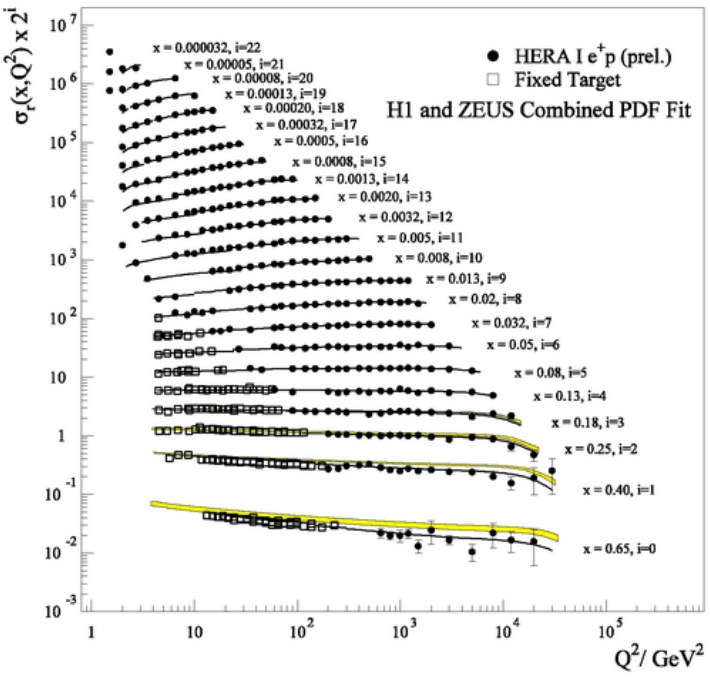

Figure 5.2 Bjorken scaling and its violation at small-x, from [14].

manifesting, as can be seen from Fig. 5.2. The theory explaining the deviations has already been well established in Chap. 2, which calculates the quantum corrections to the naive parton model. In this regard, naive parton model at high $\sqrt{s}$ ceased to be valid, and genuine QCD partons came into play.

Let's take a look at the experimental results for these parton distribution functions.

We can see from Fig. 5.3 that gluon distribution dominates over quark contents at very small-x. In other words, matter is made up glues other than blocks at small-x. Both DGLAP and BFKL confirmed this trend.

5.2 Deep inelastic scattering at small-x in dipole approach

The process of $\gamma^* A$ scattering has a very clear space-time separation in the light-cone perturbation theory.

Assuming that the proton/nucleus of interest is studied at its rest frame, then the center of mass energy $\sqrt{s} = mq^+$. It is argued that in the IMF of the virtual photon, one

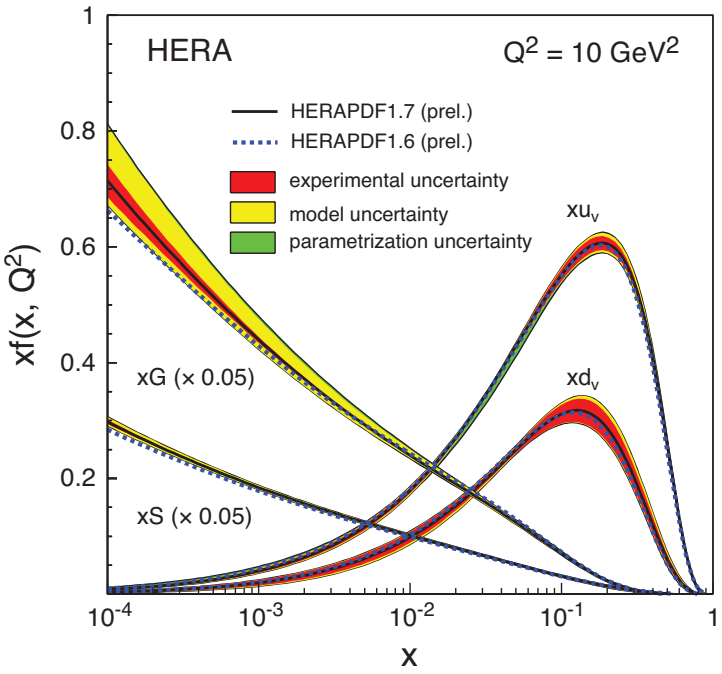

Figure 5.3 Parton distribution function, from [37].

could make further simplification on DIS by safely factoring out the photonic contribution from the rest of the strong interaction.

In this frame, the lowest order contribution comes from the splitting of the virtual photon into $q\bar{q}$ pair, which interacts with the target. The interaction time

$$x^+_{int} \sim \frac{1}{p+} = \frac{1}{m} \tag{5.2.1}$$

where m is the mass of the target; while the the lifetime for $q\bar{q}$

$$\Delta x^+_{dip} \sim \frac{1}{\frac{k_T^2}{zq^+} + \frac{k_T^2}{(1-z)q^+} - \frac{-Q^2}{q^+}} = \left[\frac{k_T^2}{z(1-z)} + Q^2\right]\frac{1}{q^+}. \tag{5.2.2}$$

Here k_T is the transverse momentum of the quark, and z denotes + momentum fraction of the photon carried by the quark.

Recalling that q^+ is assumed much larger than any other momentum scales, we conclude

$$\Delta x^+_{dip} \gg x^+_{int} \tag{5.2.3}$$

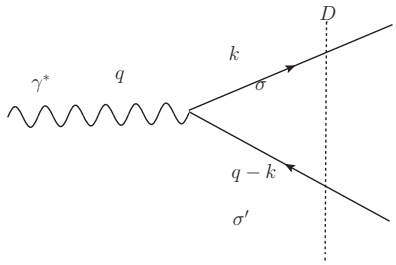

Figure 5.4 Virtual photon wave function, the dashed like denote the energy denominator.

The interaction lifetime is instantaneous compared with the lifetime of the color dipole $q\bar{q}$. Therefore, the fluctuation can be viewed as being frozen. Further, the existence of the virtual photon has its manifestation in the dipole-nucleus nucleus interactions only in the energy denominator. More precisely

$$D = k^-_{interm} - q^- \approx k^-_{interm} \tag{5.2.4}$$

Noticing that we have dropped $q^- = \frac{-Q^2}{q^+}$ due to the large q^+ assumption.

The intermediate states of the DIS bear no memory of the initial virtual photon state and the QCD interactions completely disentangles from the QED processes at small-x limit [47],

$$\sigma^{\gamma^* A} = \Phi^{\gamma^* \to q\bar{q}}(z, Q) \otimes \sigma^{q\bar{q}A}. \tag{5.2.5}$$

LCPT gives Fig. 5.4 [8]

$$\Psi^{\gamma^* \to q\bar{q}}_{T,L}(\boldsymbol{k}, z) = eZ_f \frac{z(1-z)}{\boldsymbol{k}^2 + m_f^2 + Q^2 z(1-z)} \bar{u}_\sigma(k) \gamma \cdot \epsilon^\lambda_{T,L} v_{\sigma'}(q-k), \tag{5.2.6}$$

and it is transformed into dipole picture via

$$\Psi^{\gamma^* \to q\bar{q}}_{T,L}(\boldsymbol{x}, z) = \int \frac{d^2k}{(2\pi)^2} e^{i\boldsymbol{k}\cdot\boldsymbol{x}} \Psi^{\gamma^* \to q\bar{q}}_{T,L}(\boldsymbol{k}, z) \tag{5.2.7}$$

As a consequence

$$\sigma^{\gamma^* A} = \Phi^{\gamma^* \to q\bar{q}}(z, Q) \otimes \sigma^{q\bar{q}A} \tag{5.2.8}$$

where

$$|\Psi_T^{\gamma^*\to q\bar{q}}(\boldsymbol{r},z)|^2 = 2N_c\sum_f \frac{\alpha_{em}Z_f^2}{\pi}z(1-z) \times \{a_f^2[K_1(ra_f)]^2[z+(1-z)^2]+m_f^2[K_0(ra_f)]^2\} \tag{5.2.9}$$

is the transverse wave function squared [8], with

$$a_f^2 = Q^2z(1-z)+m_f^2; \tag{5.2.10}$$

and

$$|\Psi_L^{\gamma^*\to q\bar{q}}(\boldsymbol{r},z)|^2 = 2N_c\sum_f \frac{\alpha_{em}Z_f^2}{\pi}4Q^2z^3(1-z)^3[K_0(ra_f)]^2 \tag{5.2.11}$$

is the transverse wave function squared [8].

Note that the dipole-nucleus cross section is independent of the momentum fraction z. This can be justified in the eikonal approximation and LLA, as has been explained in Chap. 4.

$$\sigma_{T,L}^{\gamma^*\to q\bar{q}}(x,Q^2) = \int\frac{d^2r}{4\pi}\int_0^1 dz|\Psi_{T,L}^{\gamma^*\to q\bar{q}}(\boldsymbol{r},z)|^2\sigma_{tot}^{q\bar{q}A}(r,Y) \tag{5.2.12}$$

This, in part, justifies the necessity of discussing in great length the dipole picture in Chap. 4. The DIS off heavy the proton/nucleus now becomes $q\bar{q}p$ and $q\bar{q}A$ interaction.

5.3 Diffraction in DIS at small-x

So far, we have constrained the discussion to the total cross section of scattering processes, which is related to the imaginary part of the forward elastic scattering amplitude through optical theorem. The final states are summed over and no exclusive information about the final states is available. We will see that diffractive particle production serves as a powerful tool in extracting more exclusive information about the scattering processes.

Diffraction in optics is due to the wave nature of the light. The electromagnetic wave superimpose in space and if an aperture or object is located in its way, the partial waves

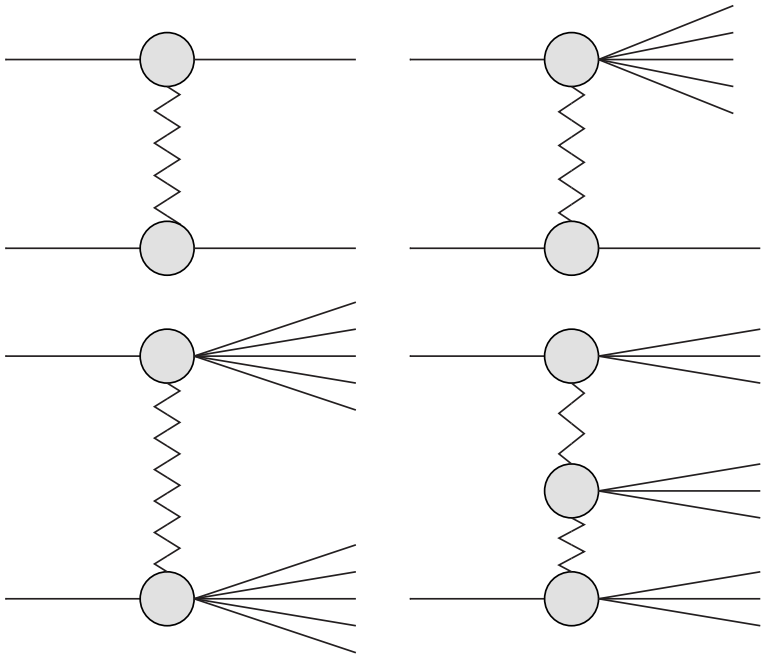

Figure 5.5 Diffractive events of:(a) elastic event, (b) single diffractive dissociation, (c) double diffractive dissociation, (d)central exclusive diffraction.

no long propagate uniformly in space, resulting in a redistribution of energy in space, forming patterns of minima and maxima [8]:

$$\frac{I(\theta)}{I(\theta=0)} = \frac{(2J_1(\theta kR))^2}{x^2} \approx 1 - R^2\frac{(k\theta)^2}{4} \tag{5.3.1}$$

Where $x = kR\sin\theta$ and R is the radius of the blocker.

This phenomenon in optics can actually find its close analogy in QCD.

Diffraction in hadronic interactions is the process in which there exists at least one rapdity gap between two final states. No particles are detected between two rapidities. The rapidity gap corresponds to zero quantum number collective gluon state [38, 40, 41, 42]–for historical reasons it is called pomeron[55].

Let us consider a hadron in the IMF while the target is at rest. If the interaction eigenstates are the same with the eigenstates of the projectile hadron, then the projectile would not change after the scattering, i.e., elastic scattering is ensured by construction.

However, if interaction eigenstates are not the eigenstates of the hadrons, diffractive pattens occur. Diffraction in QCD is analogous to diffraction in optics in a sense that there is coherent superposition of waves of different phases, giving birth to a redistribution of intensity measurable for detectors. To make our point clear, let us expand projectile hadron state $|h\rangle$ on interacton eigenstates ϕ_i [45].

$$|h\rangle = \sum_i h_i \, |\psi_i\rangle \tag{5.3.2}$$

$|\psi_i\rangle$ is the eigenstates for T-matrix,

$$ImT \, |\psi_i\rangle = t_i \, |\psi_i\rangle \, . \tag{5.3.3}$$

The normalization requires

$$\langle h \, | \, h\rangle = \sum_i |c_i|^2 = 1 \tag{5.3.4}$$

If we expand in The $2 \to 2$ cross section in the impact parameter space takes the form([8, 45]),

$$\begin{aligned} \sigma_{tot} &= 2 \int d^2b ImA(s, \boldsymbol{b}) \\ \sigma_{el} &= \int d^2b |A(s, \boldsymbol{b})|^2 \end{aligned} \tag{5.3.5}$$

Where $A(s, \boldsymbol{b})$ is the scattering amplitudes for $2 \to 2$ processes. We note that the amplitude only have a negligible real part, we arrive at

$$\frac{d\sigma_{tot}}{d^2b} = 2 \langle t \rangle \tag{5.3.6}$$

$$\frac{d\sigma_{el}}{d^2b} = \langle t \rangle^2 \tag{5.3.7}$$

Where

$$\langle t \rangle = \sum_i |c_i|^2 t_i \tag{5.3.8}$$

$$\langle t^2 \rangle = \sum_i |c_i|^2 t_i^2 \tag{5.3.9}$$

Therefore, one reaches [45],

$$\frac{d\sigma_{inel}^{diff}}{d^2b} = \left\langle t^2 \right\rangle - \left\langle t \right\rangle^2 \tag{5.3.10}$$

Inelastic diffraction per unit area for the projectile and target separated by impact parameter b is equal to the variance of the forward amplitudes weighed by its occurring probability of the state $|\phi_k\rangle$ in the projectile state $|h\rangle$. If we include elastic scattering into the diffractive scattering

$$\frac{d\sigma^{diff}}{d^2b} = \left\langle t^2 \right\rangle \tag{5.3.11}$$

Denoting

$$N = ImA \tag{5.3.12}$$

and

$$\sigma_{el}^{h_1h_2} = \int d^2bN^2(\boldsymbol{b}, Y) \tag{5.3.13}$$

$$\sigma_{tot}^{h_1h_2} = 2\int d^2bN(\boldsymbol{b}, Y) \tag{5.3.14}$$

At very high energies, black disk limit is approached, the target becomes totally absorptive, i.e., $N \to 1$. In the language of non-relativistic quantum mechanics, the projectile are bound in the infinite potential well with area πR^2, where R is the radius of the target. The projectile hits the target and was completely absorbed except at the boundary. This counts the total inelastic cross section πR^2. Recalling that the inelastic diffractive scattering is the variance of the amplitudes, for a nearly completely absorptive black disk, it is zero for small-bs and nonzero only at the edge of the target. For strict black disk limit, the inelastic diffraction vanishes. Therefore, one reaches the profound conclusion that at sufficiently high energies, the inelastic cross section and elastic cross section in hadron-hadron interactions each counts half of the total cross section.

$$\sigma_{inel} = \sigma_{el} = \frac{1}{2}\sigma_{tot} = \pi R^2 \tag{5.3.15}$$

For the purpose of this dissertation, it suffices to discuss in the framework of the DIS. In fact, as explained in our aforementioned properties of DIS, fast moving virtual photon

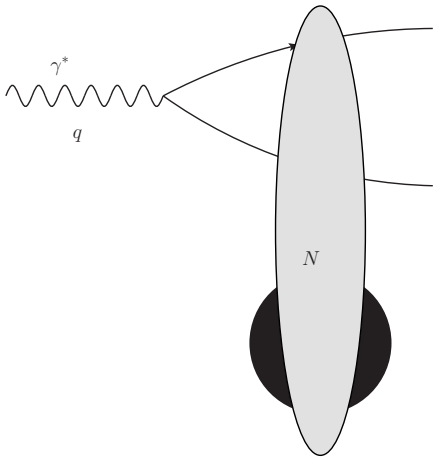

Figure 5.6 Diffractive deep inelastic scattering.

in the rest frame of the target is of hardronic nature, as can be seen from its fluctuation into color dipole, the simplest colorless state. Therefore dipole picture treatment in diffractive process in DIS is still applicable, similar to our discussion for total cross section of DIS, though they have clear difference, to be explained.

$$\sigma_{tot}^{\gamma^* A} = \int \frac{d^2r}{2\pi} d^2b \int_0^1 dz |\Psi^{\gamma^* \to q\bar{q}}(\boldsymbol{r}, z)|^2 N(\boldsymbol{r}, \boldsymbol{b}, Y) \tag{5.3.16}$$

Like before, we isolate the dipole-nucleus interaction from the initial virtual state, which deldays into $q\bar{q}$ long before the interaction, we get

$$\sigma_{tot} = 2 \int d^2b N(\boldsymbol{r}, \boldsymbol{b}, Y) \tag{5.3.17}$$

The elastic cross section is [39]

$$\sigma_{el} = \int d^2b N^2(\boldsymbol{r}, \boldsymbol{b}, Y) \tag{5.3.18}$$

Correspondingly

$$\sigma_{diff}^{\gamma^* A} = \int \frac{d^2r}{4\pi} d^2b \int_0^1 dz |\Psi^{\gamma^* \to q\bar{q}}(\boldsymbol{r}, z)|^2 N^2(\boldsymbol{r}, \boldsymbol{b}, Y) \tag{5.3.19}$$

It is diffractive, but not elastic, for $\gamma^* A$, as the virutual photon does not appear in the final state. The dipole, will hadronize in the form of jets. Let us discuss still on the

level of dipole instead of virtual photon which has been factored out of the interaction. At very high energies, if the black disk limit is achieved, elastic scattering of dipole off nucleus constitutes half of the total cross section, as stated in the general hadron projectile case. At very high energies, $N \to 1$ as predicted by BK equation. Therefore, we conclude that

$$\frac{\sigma_{el}^{q\bar{q}A}}{\sigma_{tot}^{q\bar{q}A}} = \frac{\int d^2bN^2(b,Y)}{2\int d^2bN(b,Y)} = \frac{1}{2} \tag{5.3.20}$$

It is purely quantum mechanical effect and does not have classical explanation. The dipole interacts with the nucleus via gluon cascades, i.e., dipole clouds in the large N_c limit, and after the interactions, they have half chance of going back into a dipole. The dipole clouds bears memory of the initial dipole even after the interactions with the nucleus.

5.4 Semi-inclusive process in DIS

To get more information from the scattering process, we often go further from inclusive total DIS to semi-inclusive DIS, where, along with the measurement for the outgoing leptons, one of the hadrons is measured. This unveils more information from scattering process.

$$l + h \to l' + h' + X, \tag{5.4.1}$$

where l' and h' are the outgoing lepton and hadrons, respectively. h' is the final product of the hadronization process starting from outgoing partons.

As stated above, the photon can be treated as hadronic. The fluctuation of photons into hadronic contents have lifetime greatly larger than the typical interaction time of its hadronic contents with the rest target.

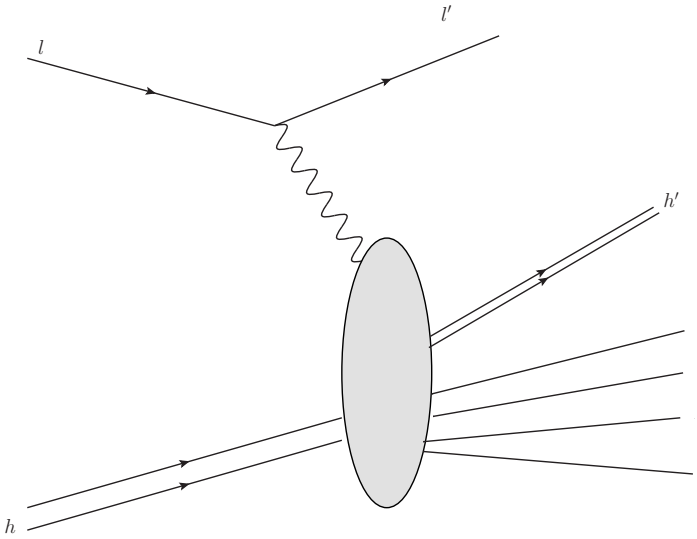

Figure 5.7 Semi-inclusive DIS.

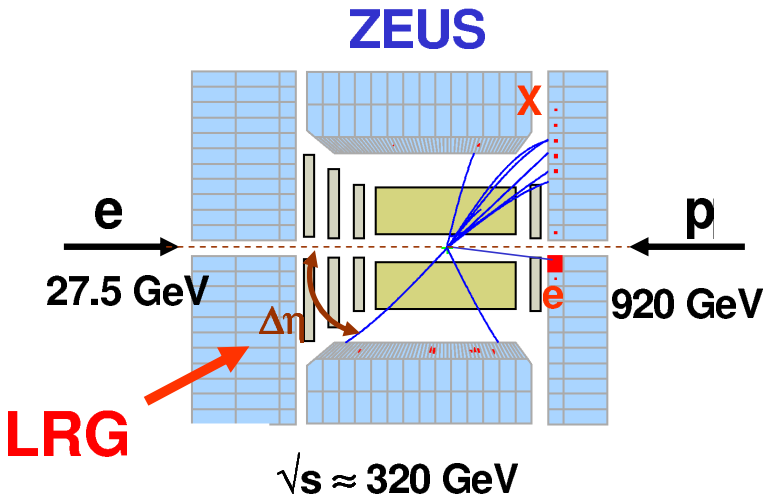

Figure 5.8 A schematic illustration for diffractive DIS event in HERA, picture excerpted from [44].

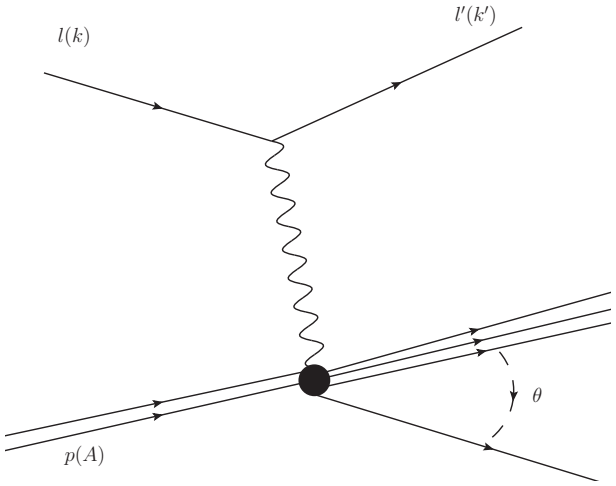

Figure 5.9 Diffractive DIS event diagram.

5.5 Semi-inclusive diffractive process in DIS

$$l + N \to l' + N' + X + [\text{LRG}] \tag{5.5.1}$$

Where [LRG] stands for Large rapidity gap,see Fig. 5.9 and [43].

Here is the typical kinematic variables typically used in semi-inclusive DIS

$$t = (k - k')^2, \quad M_X^2 = (k - k' - q)^2, \quad M_Y^2 = k'^2,$$
$$x_{\mathbb{P}} = \frac{(k - k') \cdot q}{k \cdot k'} = \frac{M_x^2 + Q^2 - t}{W^2 + Q^2 - M^2}, \quad \beta = \frac{Q^2}{M_x^2 + Q^2 - t} = \frac{x}{x_{\mathbb{P}}} \tag{5.5.2}$$

$x_{\mathbb{P}}$ is the nucleus/proton momentum fraction carried by the Pomeron while β being the momentum fraction of the pomeron carried by the parton struck by the virtual photon. M is the mass of nucleus/proton.

Let us define a diffractive structure function [44]

$$\frac{d\sigma}{dx dQ^2 d^2 x_{\mathbb{P}} dt} = \frac{4\pi\alpha_{em}^2}{xQ^2}[(1 - y + \frac{y^2}{2})F_2^{D(4)} - \frac{y^2}{2}F_L^{D(4)}] \tag{5.5.3}$$

where $F_i, \quad i = T, L, 2$ are diffractive structure functions, and

$$F_i^{D(3)}(x_{\mathbb{P}}, \beta, Q^2) = \int_{|t|_{min}}^{|t|_{max}} dt F_i^{D(4)}(x_{\mathbb{P}}, \beta, Q^2), \quad i = T, L, 2 \tag{5.5.4}$$

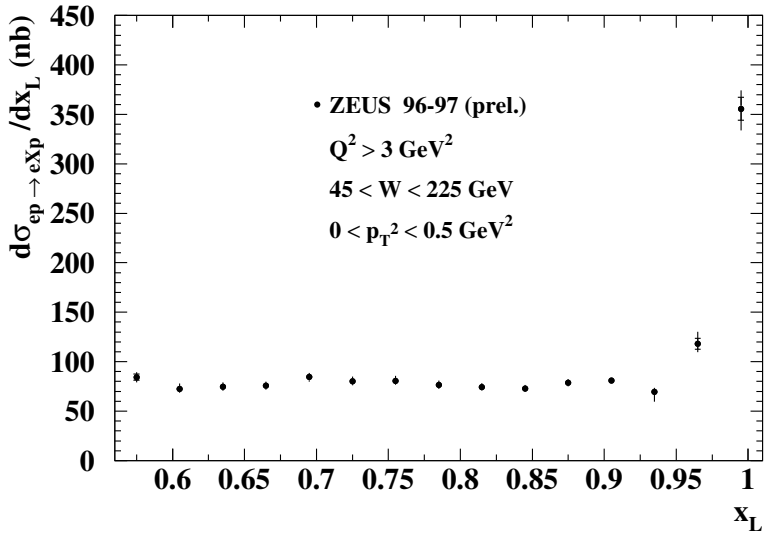

Figure 5.10 x_L dependence, excerpted from [44].

are the t-integrated structure functions. Noting that

$$F_2 = F_T + F_L. \tag{5.5.5}$$

The definition of F_is run parallel with (5.1.5), except that we are now studying its differential form.

The HERA ep collision records a 15% of the events are diffractive. First, the hadronic final state X has the same quantum number of the photon. Second, the outgoing hadronic state X and the emerging proton are separated by a large rapidity gap, see Fig. 5.9.

Fig. 5.10 show the dependence of $F_2^{D(3)}$ with β vs the dependence on x_B of F_2. One can see that the diffractive structure function is flat while F_2 decay very fast for $x_B > 0.2$.

There are two distinctive features that could be extracted from Fig. 5.11 (see [44] for details), where in this figure x_L is defined as the momentum fraction of the incoming proton carried by the outgoing proton. First, the highest cross section $\frac{d\sigma^{diff}}{dx_L}$ exists at $x_L \approx 1$. Also, the t-dependence peaks at $t = 0$ and exponentially suppressed away from $t = 0$. These are typical behaviors of diffraction commonly seen in optics. It is a highly nontrivial phenomenon. Thinking of the momentum transfer of the electron, Q^2 can be hundreds of GeV^2, while the momentum transfer of the proton t is close to zero. The

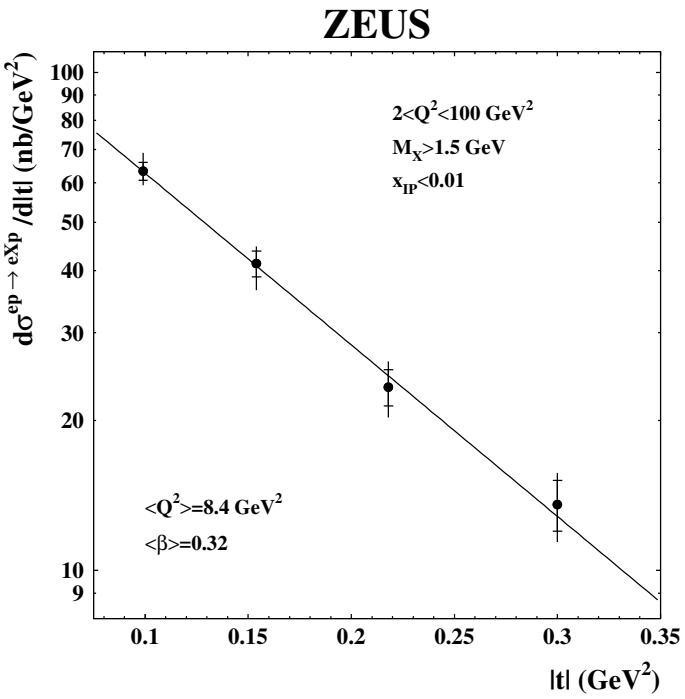

Figure 5.11 t-dependence for $F_2(x_{\mathbb{P}}, \beta, Q^2)$, excerpted from [44].

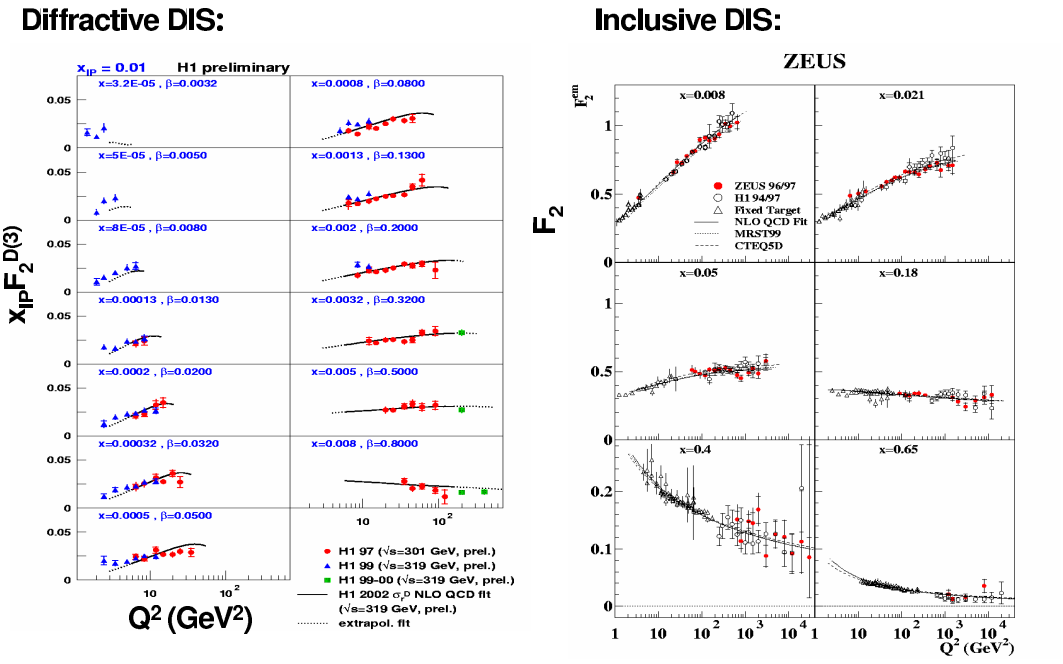

Figure 5.12 Diffractive vs inclusive DIS in Q^2 dependence, excerpted from [44].

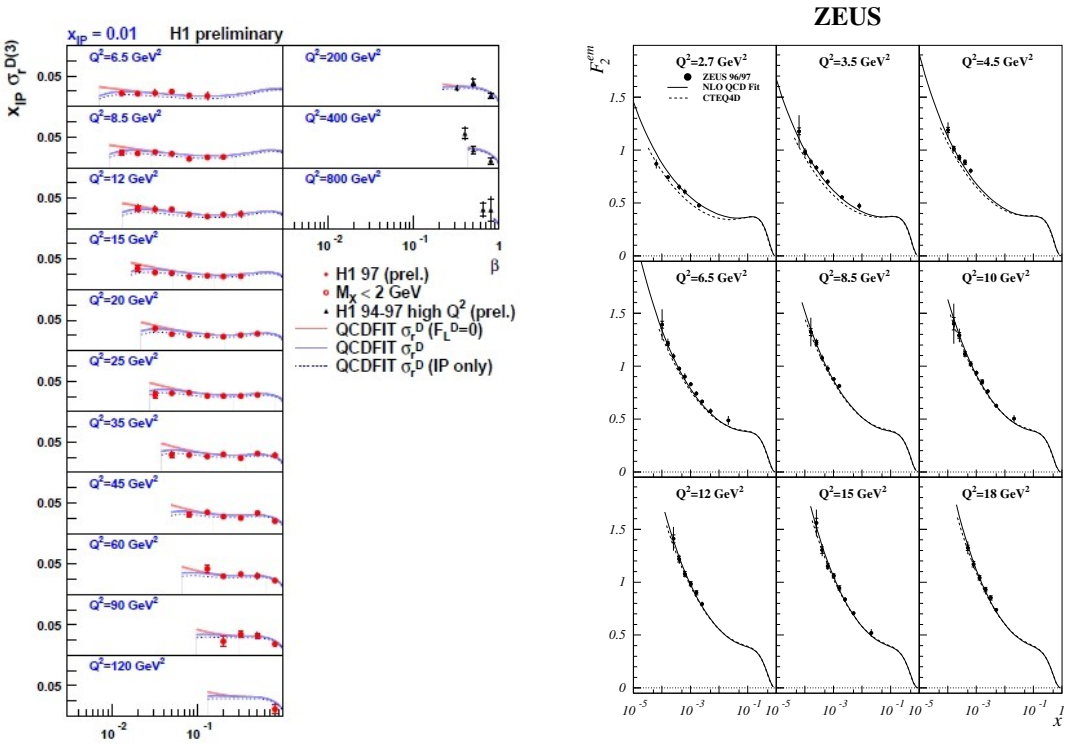

Figure 5.13 Diffraction in β vs inclusive in x, plots excerpted from [51] and [52].

sheer coexistence in a single event the very hard scale and soft scale does not come from any classical analogy, but rather, it has its origin in the wave nature of the hadrons.

Fig. 5.12 shows the the comparison between $F_2^{D(3)}$ and inclusive DIS F_2 with respect to their Q^2 dependences; Fig. 5.13 compares the β dependence of $F_2^{D(3)}$ and x_B dependence of F_2.

Note that for β of all range, the diffractive structure function is logarithmically dependent on Q^2. This approximate Bjorken scaling behavior justifies a parton model treatment of diffractive inclusive DIS. It grows with Q^2 except for $\beta \sim 1$. In comparison, F_2 grows with Q^2 for small $x_{\mathbb{P}}$, where x_B range from $x_B < 0.2$; otherwise, it goes down logarithmically. Violation of Bjorken scaling is well explained by DGLAP evolution equation. The growth of F_2 at small x_B indicates more gluons are detected. For very small-x_B, the proton become a gluon-dominated matter. Similarly for small βx_B, it should become gluon dominated: since $x_B \sim 0.02$, no matter what value β takes, βx_B

is very small [44].

Define *Rapidity* by

$$y = \ln \frac{E' + k'}{E' - k'} \tag{5.5.6}$$

At very high energies, it is related to pseudo-rapidity,

$$\eta = -\ln\left(\tan\frac{\theta}{2}\right) \tag{5.5.7}$$

Where θ is the angle of the struck parton from the proton/nucleus remnant direction.

We can see that diffractive events are measured at very small angle from the beam directions, therefore observing the diffractive patterns pose a great challenge to the experimentalist as it calls for detectors at very forward directions.

Another important effect coming from saturation is the ratio for diffractive to total cross section, at very high energy limit, diffractive events constitute half of the cross section, fig 5.14 attested to this prediction well.

5.6 Deep Inelastic scattering off heavy nucleus

The kinematics of the DIS off heavy nucleus follows our discussion in DIS off proton. However, p should be understood as the momentum for individual nucleons inside nucleus, i.e.,$p = P/A$. Here P is the momentum of the nucleus and A is the atomic mass. As a result, for Bjorken-x, instead of $0 < x < 1$, we have $0 < x < A$.

EMC effect [15, 16] is observed at $x \gtrsim 0.3$ at the Bjorken-x. It compared the structure function F_2 for a nucleus to that for a deuteron, both normalized to a single nucleons. EMC effect shows that A-dependence of structure function is nontrivial and a proper explanation of EMC effect remains an unsolved question.

While EMC effect is important in its own right–our study is largely focused on pinning down the saturation effect that occurs in the region of small-x–we would not go any further in this dissertation on EMC effect.

A much broader range data for x shows where EMC effect attested to a great number

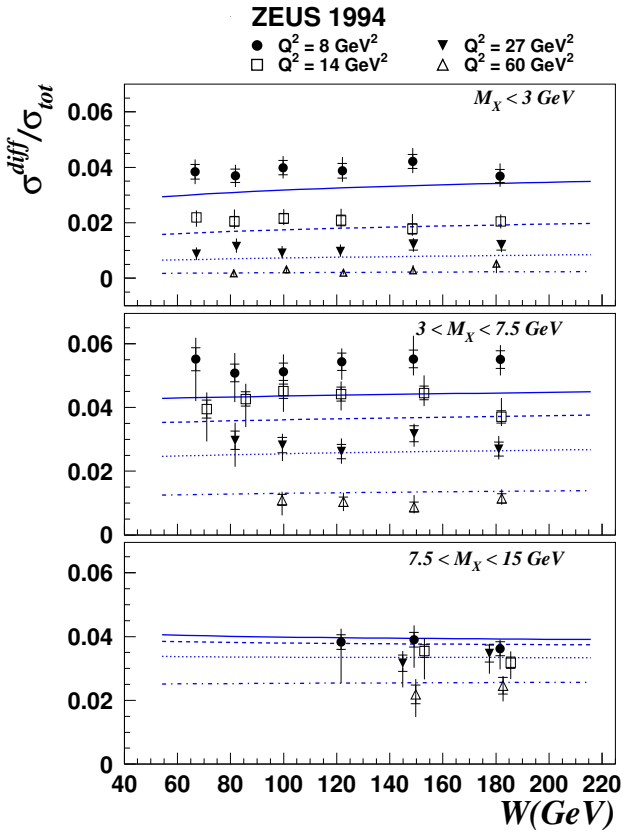

Figure 5.14 Diffractive to total cross section in $\gamma^* p$,excerpted from [44, 85].

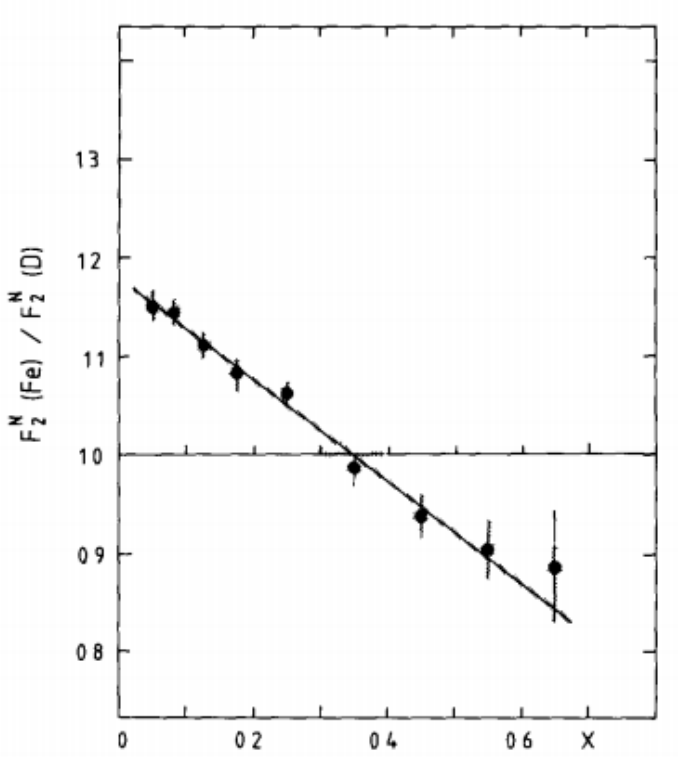

Figure 5.15 EMC effect, from [15].

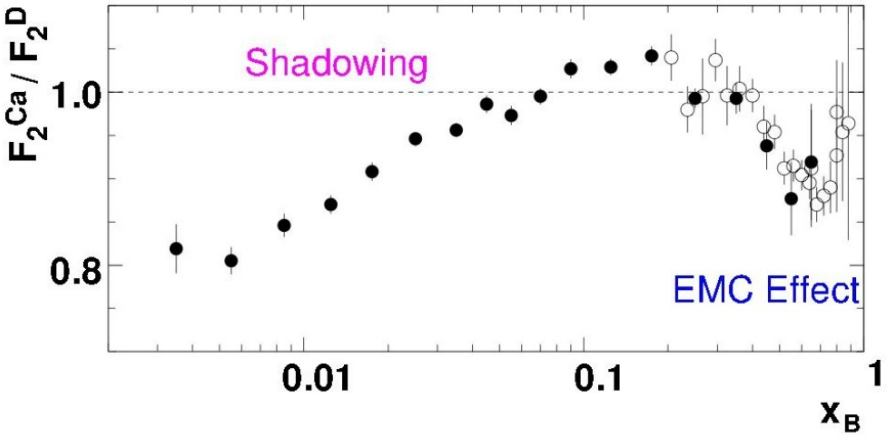

Figure 5.16 EMC effect and nuclear shadowing, from [16].

of experiments at moderately small x region. Also another effect shows up at small-x.

The suppression of the ratio of cross section in DIS small-x is known as shadowing region. As the name suggests, it is due to overlapping of the wave functions of the nucleons in the longitudinal direction inside the nucleus that likely causes the reduction of the ratio compared against that for a free nucleon. For Bjorken-x tuned smaller, in the IMF of the nucleus, overlapping of the nucleons is no longer negligible. An intuitive picture would be a nucleon, shaded by nucleons located before itself in the longitudinal direction, interacts only partially with the projectile. In fact, at small enough x the gluon density in each of the constituent nucleons inside nucleus becomes so large that they start to interacts with gluons coming from other nucleons. The gluon distribution cannot be the incoherent sum of the all the gluon distributions of each of the nucleons, as the gluons from different nucleons become highly correlated. The large number of nucleons inside nucleus makes possible a significant level of merging between the gluons from different nucleons, resulting in gluon saturation.

5.7 DIS off heavy nucleus in small-x

We will explain in this section that the DIS experiment on heavy nuclei is the best way to study gluon dynamics. At very high energy, the large number of nucleon overlaps and they form a very strong gluonic field in the wave function nucleus, which is known as Color Glass Condensate. A typical scale that describes the transition to this nonlinear regime is saturation momentum Q_s. In fact, this momentum scale goes way beyond Λ_{QCD} and makes possible perturbative calculations.

We can extract most useful information about the proton by DIS off a proton. Then what are the necessities of DIS off heavy ions? As we have discussed in Chap. 4, the saturation effect was hinted in HERA, RHIC and LHC data and it is expected that by conducting measurements in Electron Ion Collider(EIC)[36], one can gain unprecedented

precision. Naively, one might wish to measure gluon saturation effect in proton. This is correct in principle, but the cost to collide electrons and protons to high enough energy goes beyond reasonable budget. In fact, an ep collider capable of detecting the saturation point must be of TeV scale. However, due to the $A^{1/3}$ factor in the saturation scale, ~ 100 GeV is sufficient in obtaining data with sufficient confidence level for the existence of gluon saturation/CGC.

F_2^A is proportional to the quark distribution inside the nucleus,while F_L^A proportional to the gluon distribution. To quantify the effect of binding nucleons inside the nucleus and nuclear environment on the parton distributions, it is instructive to define nuclear modification factor [37]

$$R_2 = \frac{F_2^A}{AF_2^N}, \quad R_L = \frac{F_L^A}{AF_L^N}. \tag{5.7.1}$$

They compared the parton distribution in a heavy nucleus with that in a proton, effective measuring the nuclear effect on the parton distributions. Naively, if the parton distributions are the simple summation of the distribution of A nucleus, they would be equal to unity. However, as we see in Fig. 5.16, they behave nontrivially for a wide range of x.

5.8 Measurement of diffractive events

Diffractive interactions occur if the electron probe in DIS interacts with the target via the exchange of partons of zero net color, as we have seen in DIS events in HERA. In HERA, diffractive events means the proton is intact and is separated by the large rapidity gap with the hadronic state X. In eA collisions, another possibility comes into play. First, like the ep case, the nucleus stays intact. Second, the nucleus breaks up. Let us remind ourselves that diffraction in hadronic interactions is defined by the large rapidity gap. It turns out that coherent diffractive cross section has the pattern of maxima and minima, in analogy with what happens in optics. However, incoherent

diffractions is characterized by a slowly decaying trend in t instead of wave-like pattern. It is still pinned down by a rapidity gap, though, by definition.

Diffractive vector meson production $e + A \to e' + A' + V$ is the simplest exclusive process of DIS diffraction [37]. The vector mesons have the same quantum number as the photon and therefore the photon exchange zero quantum number with the nucleus, making the process diffractive. In fact, the size of the vector mesons serves as a measurement for saturation. The larger the size, the deeper into saturation region it probes. For small vector mesons, like J/ψ, is not sensitive to saturation due to color transparency. This feature is related to our discussion on the properties of dipole interactions with nucleus in Chap. 4. The virtual photon fluctuates into a dipole, and dipole evolves into a dipole cascade, with each daughter dipole interacting with the nucleus via two-gluon exchange. After interactions with the nucleus, it is precisely the dipole cloud that recombines into a dipole of the same size as the one after the photon dissociation, which subsequently associates into a vector meson after the interaction. The typical size for the dipole size squared $r^2 \sim \frac{1}{Q^2+M_X^2}$(see [37]). For smaller (heavier)vector mesons, the typical dipole size is smaller, and stays relatively away from saturation region compared with larger vector mesons.

This trend is illustrated in Fig. 5.17. One can see that J/ψ is relatively insentive to saturation–the cross section under saturation and non-saturation model are closer–in comparison with that for a ρ meson. For large Q^2, one can see for each panel, both modelled results drift away from the saturation regions and tend to unity.

Coherent diffraction is most useful in the obtaining the spatial distribution of quarks and gluons. It is done by analyzing the t-dependence. In fact, the virtual photon interacts with the nucleus via the exchange of partons with zero net color. The lowest order of that is a two gluon exchange. By Fourier transforming the squared root of the t-distribution, one can access the gluon distribution inside the nucleus (see [37]). Incoherent diffractions, on the other hand, is the measure of the variance of fluctuation of

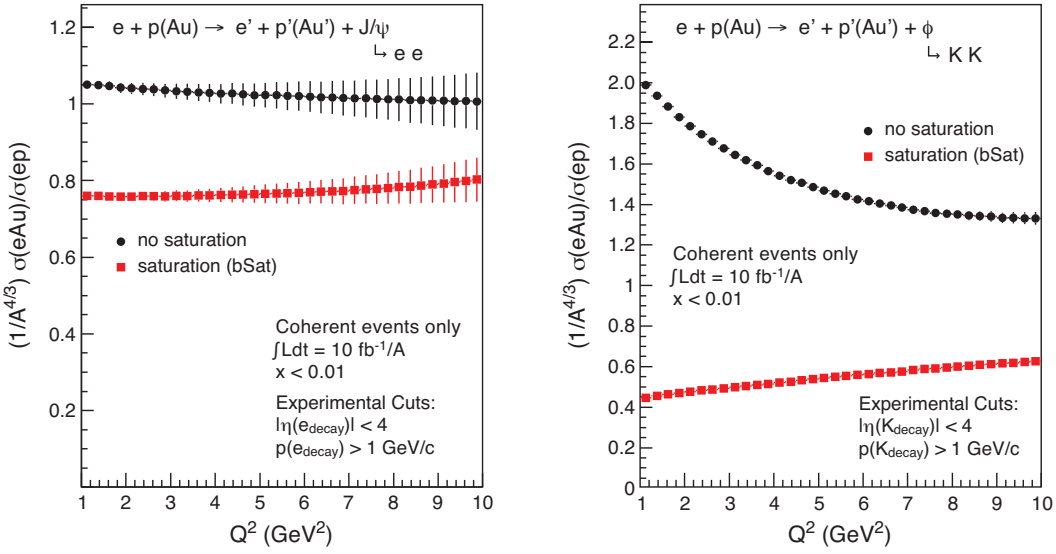

Figure 5.17 Ratio of vector meson production cross section of eA to ep in exclusive diffraction, excerpted from [37].

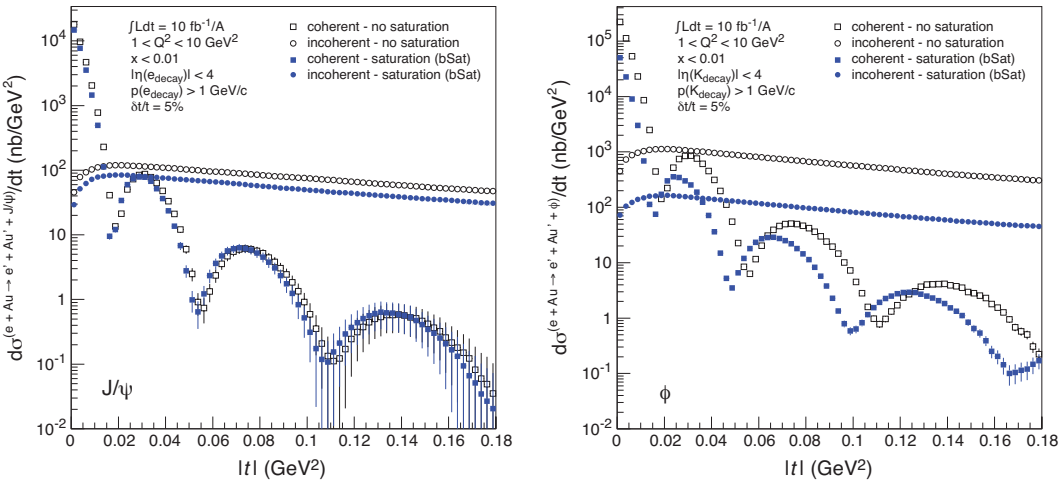

Figure 5.18 Coherent diffraction and incoherent diffraction with respect to their $|t|$ - dependences, excerpted from [37].

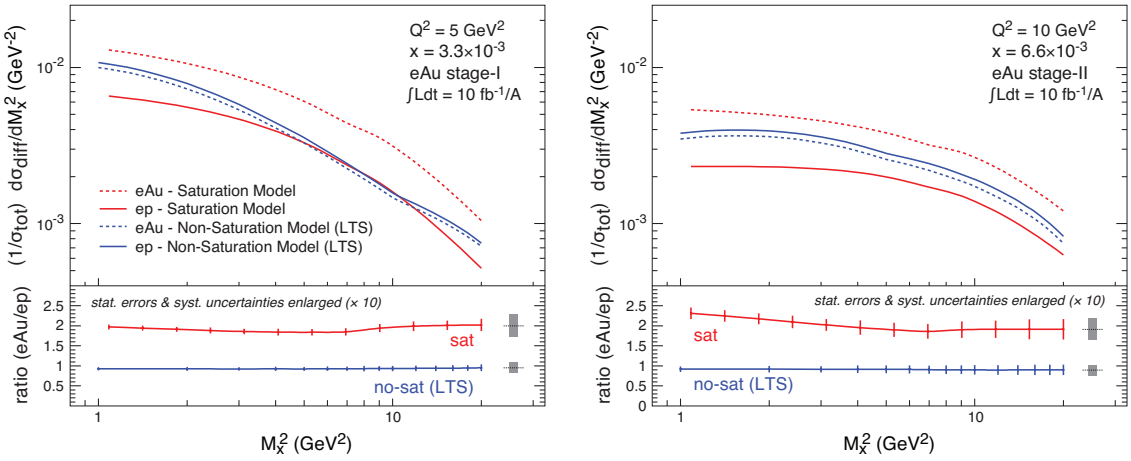

Figure 5.19 Ratio of inclusive diffraction to total in EIC, excerpted from [37].

the source. Experimentally, by detecting the neutron production [37], one can distinguish the process of coherent and incoherent diffraction. Fig. 5.18 are two plots of cross section for exclusive vector meson production in diffraction. Left panel is for J/ψ while right one for ϕ mesons. As expected, larger vector mesons(ϕ meson) are better probes for saturation. Further, we can explore from the figure, that diffractive pattern are different for coherent and incoherent diffractions. Coherent diffractions is most concentrated at very small angles, while incoherent ones survives much wider range in momentum tranfer, i.e., angular distributions are wider than the coherent cases.

It is useful to measure the ratio of coherent diffractive to total cross section. In Fig. 5.19, ratios of inclusive coherent diffractive cross section to total cross section $(d\sigma_{diff}/dM_X^2)/\sigma_{tot}$ in eAu and ep are plotted against the diffractive mass variable M_X^2, respectively. Left panel and right panel each predicts the EIC-stage I and EIC-state II. Note that they differ in the value for Q^2 and x. In each panel, saturation model and non-saturation models are both presented in comparison for each ratio. The lower plot for each panel is the double ratio $[(d\sigma_{diff}/dM_X^2)/\sigma_{tot}]_{eA}/[(d\sigma_{diff}/dM_X^2)/\sigma_{tot}]_{ep}$ One can read off the plots that two models are clearly distinguishable and future experiments would likely make unambiguous selections, thus testing the correctness of gluon saturation.

Fig. 5.19 shows that nuclear effects are stronger at large Q^2. The lower the Q^2,

the deeper the nucleus is in the saturation region, as predicted by DGLAP equations. Therefore, saturation effects tend to bring down A-dependence in $(d\sigma_{diff}/dM_X^2)/\sigma_{tot}$. Another effect is that the diffractive to total cross section ratio indeed goes up with decreasing Q^2,i.e. deeper in saturation region, offering hints to the onset of black disk limit.

5.9 Proton-nucleus(pA) scattering at small-x

It is interesting to discuss particle production in pA scattering. pA scattering cross sections, similar to that for DIS, can be cast in the dipole model. It can be shown that pA scattering bears close resemblance with $\gamma^* A$ scattering, so that the formalism developed for DIS at small-x–in the absence of direct experimental evidence from an Electron Ion Collider expected to be built in future–may be tested by existing data for pA scattering.

The small-x limit can be studied in low-$\boldsymbol{k}$ region, extended geometric scaling region and saturation region (see [8] and the references therein for detailed discussions). All these regions show a suppression of nuclear modification factor under 1. Note that the nuclear effect at very small-x caused suppression of cross section in the entire region of $\boldsymbol{k}$. At very small-x, gluon merge become predominant and gluon density saturates. Since the nuclear modification factor measures the ratio of gluon density for a nucleus in comparison with that of a nucleon, this suppression at small-x is in agreement of saturation effect of enhanced by the nuclear weight A, see Chap. 4.

Fig. 5.20 show the experimental result for single inclusive hadron production in pPb process at mid rapidity. We can see that it agrees qualitatively with our expectations. At low-$\boldsymbol{k}$, nuclear modifications factor is suppressed, and a Cronin peak is manifesting at moderately high-$\boldsymbol{k}$. Very high-$\boldsymbol{k}$ spectrum needs careful analysis since quantum evolution must be accounted for and the numbers of produced partons are no longer conserved. On the other hand, since experimental data is for mid-rapidity, we do not expect an overall

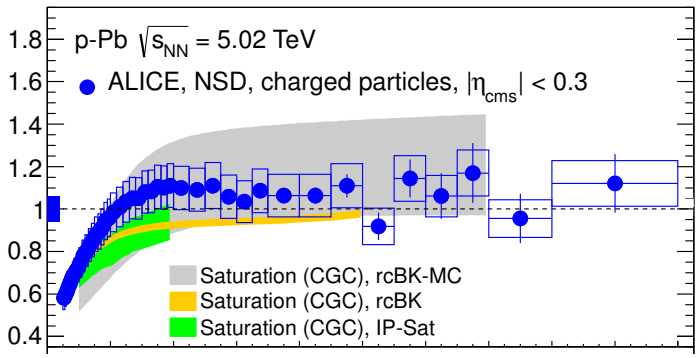

Figure 5.20 Charged hadron nuclear modification factor at mid-rapidity at LHC in p-Pb process, the x-axis is the transverse momentum of the charged hadron p_T, while the y-axis is the nuclear modification factor R^{pPb}, from [53].

suppression for all $\boldsymbol{k}$ range.

PART III

Hadron production in DIS at small-x

This part of the dissertation is primarily concentrated on my research work [160],[161]. It is structured as follows. First, I will discuss the properties of coherent and incoherent diffractive gluon production in $\gamma^* A$ at small-x. Then, I will study inclusive gluon production in DIS at small-x, especially on the effect of NLO corrections to BK evolution equation on the particle production spectrum.

CHAPTER 6. Diffractive gluon production in DIS at small-x

6.1 Introduction

Diffraction is one of the most effective tools for investigating the structure of the nuclear matter at low values of Bjorken variable x. Its hallmark is large rapidity gaps (LRG) in rapidity distribution of the produced hadrons. At high energies, these gaps correspond to scattering processes mediated by exchange of a collective gluon state with vacuum quantum numbers, known as Pomeron. On the other hand, according to the Pomerantchuk theorem, high energy asymptotic of QCD is driven by the Pomeron exchange (see e.g. [55]). Hence, measurements of diffractive structure functions at HERA attracted a lot of interest. Indeed, diffractive physics at HERA yielded many exciting results that heralded the dawn of the new QCD regime of gluon saturation/color glass condensate (CGC) [56, 57, 58, 59, 78, 68, 70, 72, 74, 75].

A possible launch of Electron Ion Collider (EIC) will open new avenues in studying the physics of diffraction in high energy nuclear physics. It will not only allow probing lower x and measure dependence of diffractive processes on nuclear weight, but also make possible studying less inclusive processes. One such process, diffractive hadron production in DIS is the subject of this chapter. Our goal is to make predictions for DIS on a nucleus at the EIC kinematic region based on the CGC theory. We argue that diffractive hadron production is very sensitive to parameters of CGC and thus can be very effective instrument in extracting properties of the nuclear matter at low x. Gluon saturation effects on diffractive gluon production in DIS on proton at HERA have

been discussed in [83, 82, 84, 85, 86, 95, 93, 87, 94]. A concise discussion of the gluon saturation effects in semi-inclusive DIS on nuclei is given in [97, 98, 96].

This chapter is structured as follows. In Sec. 6.2 we review the formalism developed in our previous publications [99, 100, 101], which allows for the calculation of coherent and incoherent diffractive gluon production in the regime of coherent scattering $l_c \gg R_A$, where $l_c = 1/(M_P x)$ is the coherence length in the nucleus rest frame. Coherent diffractive gluon production is the process $\gamma^* + A \to X + h + [LRG] + A$. The corresponding cross section is given by Eqs. (6.2.1)–(6.2.3) and (6.2.6) below. For heavy nuclei $A^{1/3} \sim 1/\alpha_s^2 \gg 1$ and at high energies this type of diffractive process dominates over the incoherent diffraction, which is the process $\gamma^* + A \to X + h + [LRG] + A$ with A^* being excited nucleus. Nevertheless, at EIC energies, cross sections for coherent and incoherent diffraction processes are often comparable [101]. In pA collisions their dependences on gluon rapidity y and transverse momentum $\boldsymbol{k}$ and on atomic weight A are quite different. Therefore, as was pointed out in [101], it is important to separately measure the contributions of these diffractive processes. In Sec. 8 we calculate these contributions using the b-CGC model [143] for the color dipole scattering amplitude. As in [100] we characterize the nuclear effect using the nuclear modification factor (NMF) for diffractive processes defined in (7.7.1). The results of our numerical calculations are presented in Fig. 6.2. The most interesting features of the NMF's are (i) strong dependence of coherent diffractive NMF on gluon rapidity y (or $x_{I\!P}$); (ii) near independence of incoherent diffractive NMF on y and (iii) independence of both NMF's on the photon virtuality. This results are discussed in detail in Sec. 8.

Separation of coherent and incoherent diffractive contributions pose a great experimental challenge because it requires measurements of very small scattering angles $\theta = 2\sqrt{-t/W^2}$, where t is the moment transfer and W is the center-of-mass energy per nucleon of $\gamma^* A$ process. We address this problem in Sec. 6.4. Dependence of the coherent cross section on momentum transfer t is given by (6.4.9). It is seen that it decreases as

$1/|t|^3$ at $|t| \gg 1/R_A^2$, where R_A is the nuclear radius. On the other hand, incoherent diffraction cross section decreases exponentially as $e^{-|t|R_p^2/4}$, but at much larger momentum transfers $t > 1/R_p^2$ as seen in (6.4.20). The results of the calculation are plotted in Fig. 6.3. As expected coherent diffraction dominates at small momentum transfers $-t$ while the incoherent one at large $-t$. However, due to different functional form of t-dependences, the two contributions become of the same order at about $-t \sim R_P^{-2}$ and remain comparable even at larger momentum transferes. The corresponding scattering angle for $W = 100$ GeV is $\theta \approx 0.13^{\rm o}$ and is very weakly dependent on the hadron transverse momentum, $x_{I\!P}$ and photon virtuality Q^2. It seems that such scattering angles are within the experimental reach and hopefully the two contribution can be separated.

6.2 Diffractive gluon production

6.2.1 Dipole cross section

Consider diffractive production of a gluon of transverse momentum $\boldsymbol{k}$ at rapidity y. Let the total rapidity interval be $Y = \ln(1/x)$, where $x = Q^2/W^2$, Q^2 is photon virtuality and W the center-of-mass energy of $\gamma^* N$ scattering. Cross section for diffractive gluon production reads [88]

$$\frac{d\sigma_{\rm diff}^{\gamma^* A}(Q^2, x, k, y)}{d^2k\, dy} = \int \frac{d^2r}{2\pi^2} dz\, \Phi^{\gamma^*}(Q, r, z)\, \frac{d\sigma_{\rm diff}^{q\bar{q}A}(r, x, k, y)}{d^2k\, dy}\,, \tag{6.2.1}$$

where

$$\frac{d\sigma_{\rm diff}^{q\bar{q}A}(r, x, k, y)}{d^2k\, dy} \tag{6.2.2}$$

is the differential cross section for the diffractive gluon production by a $q\bar{q}$ dipole (a.k.a. onium) of transverse size r scattering off a nucleus. Eq. (6.2.1) generalizes the quasi-classical result derived in [89, 90, 91]. Other kinematic variables that are often used are β and $x_{I\!P}$. They are defined as $\ln(1/\beta) = Y - y$ and $\ln(1/x_{I\!P}) = y$, where $Y - y$ is the rapidity interval between the photon and the produced gluon. We work in the

approximation $\alpha_s \ln(1/x) \sim 1$, $\alpha_s \ln(1/\beta) \sim 1$. Diffractive production in the region $\beta \lesssim 1$ was addressed in [82, 92]. We assume that the produced gluon is at the edge of the rapidity gap, so that the total rapidity gap in the process is y, see Fig. 6.1.

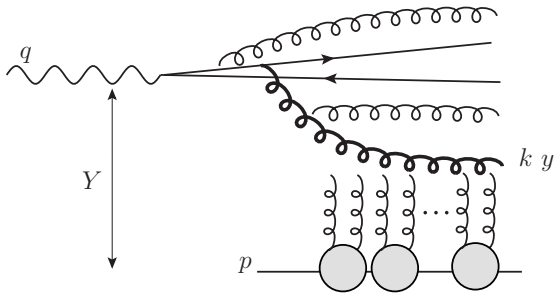

Figure 6.1 Diffractive production of a gluon with transverse momentum $\boldsymbol{k}$ and rapidity y, which is also the rapidity gap of the process.

Virtual photon light-cone wave-function reads(c.f.(5.2.9),(5.2.9))

$$|\Psi^{\gamma^*}(Q,r,z)|^2 = |\Psi_T^{\gamma^*}(Q,r,z)|^2 + |\Psi_L^{\gamma^*}(Q,r,z)|^2 \quad (6.2.3)$$

$$|\Psi_T^{\gamma^*}(Q,r,z)|^2 = 2N_c \sum_f \frac{\alpha_{\rm em}^f}{\pi}\{a^2 K_1^2(ra)[z^2+(1-z)^2] + m_f^2 K_0^2(ra)\} \quad (6.2.4)$$

$$|\Psi_L^{\gamma^*}(Q,r,z)|^2 = 2N_c \sum_f \frac{\alpha_{\rm em}^f}{\pi} 4Q^2 z^2 (1-z)^2 K_0^2(ra) \quad (6.2.5)$$

where $a^2 = Q^2 z(1-z) + m_f^2$, $\alpha_{\rm em}^2 = e^2 z_f^2/(4\pi)$, with z_f being the quark electric charge.

6.2.2 Coherent and incoherent diffraction

We will consider two types of diffractive processes on nuclei – coherent and incoherent diffraction. Recall that in Sec. 5.7 that coherent diffraction is a process in which the nucleus stays intact. For the DIS subprocess dipole–nucleus scattering, it is elastic process. At very high energies, such processes constitute half of the total dipole–nucleus cross section, another half being the inelastic processes. Therefore, fractions of coherent diffractive processes is expected to rise with energy. Experimental observation of this diffractive processes is very challenging because it requires measurements at very small

scattering angles, i.e. at very small momentum transfers $t \sim 1/R_A^2$. We discuss this in detail in Sec. 6.4.

Incoherent diffraction means the nucleus decays into colorless remnants. This process occurs at the nuclear edge where the partial scattering amplitude at a given impact parameter is less than unity. Fraction of this contribution in the total inelastic cross section decreases with energy and with nuclear weight. Importance of inelastic diffraction stems from the fact that it measures fluctuation of the color glass condensate near its quasi-classical mean-field value. Typical momentum transfer in this case is $t \sim 1/R_p^2$ which allows much easier experimental study. We will discuss coherent and incoherent diffraction separately, assuming no experimental cuts on the minimal scattering angle. These will be discussed in the next section Sec. 6.4.

The cross section for the coherent diffractive gluon production including the small-x evolution was derived in [88, 99] and can be written as

$$\frac{d\sigma_{\rm cd}(\boldsymbol{r},x,\boldsymbol{k},y)}{d^2\boldsymbol{k}\,dy} = \frac{\alpha_s C_F}{\pi^2}\,\frac{1}{(2\pi)^2}\int d^2b \int d^2r'\, n_p(\boldsymbol{r},\boldsymbol{r}',Y-y)\,|\boldsymbol{I}_{\rm cd}(\boldsymbol{r}',x,\boldsymbol{k},y,\boldsymbol{b})|^2\,, \quad (6.2.6)$$

where

$$\begin{aligned}\boldsymbol{I}_{\rm cd}(\boldsymbol{x}-\boldsymbol{y},x,\boldsymbol{k},y,\boldsymbol{b}) \;=\; & \int d^2z \left(\frac{\boldsymbol{z}-\boldsymbol{x}}{|\boldsymbol{z}-\boldsymbol{x}|^2}-\frac{\boldsymbol{z}-\boldsymbol{y}}{|\boldsymbol{z}-\boldsymbol{y}|^2}\right) e^{-i\boldsymbol{k}\cdot\boldsymbol{z}} \\ & \times\Big\{-N_A(\boldsymbol{z}-\boldsymbol{x},\boldsymbol{b},y)-N_A(\boldsymbol{z}-\boldsymbol{y},\boldsymbol{b},y)+N_A(\boldsymbol{x}-\boldsymbol{y},\boldsymbol{b},y) \\ & +N_A(\boldsymbol{z}-\boldsymbol{x},\boldsymbol{b},y)\,N_A(\boldsymbol{z}-\boldsymbol{y},\boldsymbol{b},y)\Big\}\,. \end{aligned} \quad (6.2.7)$$

Differential cross sections for coherent diffraction reads

$$\frac{d\sigma_{\rm id}(r,x,k,y)}{d^2k\,dy} = \frac{\alpha_s C_F}{\pi^2}\,\frac{\pi R_p^2}{2(2\pi)^2}\int d^2b \int d^2r'\, n(r,r',Y-y)\,\rho\, T_A(\boldsymbol{b})\,|\boldsymbol{I}_{\rm ID}(r',x,k,y,b)|^2\,, \quad (6.2.8)$$

where

$$\boldsymbol{I}_{\rm id}(\boldsymbol{x}-\boldsymbol{y},x,k,y,b)=\int d^2z\left(\frac{\boldsymbol{z}-\boldsymbol{x}}{|\boldsymbol{z}-\boldsymbol{x}|^2}-\frac{\boldsymbol{z}-\boldsymbol{y}}{|\boldsymbol{z}-\boldsymbol{y}|^2}\right)e^{-i\boldsymbol{k}\cdot\boldsymbol{z}}$$
$$\times\Big\{\left[1-N_A(\boldsymbol{z}-\boldsymbol{x},\boldsymbol{b},y)\right]\left[1-N_A(\boldsymbol{z}-\boldsymbol{y},\boldsymbol{b},y)\right]\left[N_p(\boldsymbol{z}-\boldsymbol{x},0,y)+N_p(\boldsymbol{z}-\boldsymbol{y},0,y)\right]$$
$$-\left[1-N_A(\boldsymbol{x}-\boldsymbol{y},\boldsymbol{b},y)\right]N_p(\boldsymbol{x}-\boldsymbol{y},0,y)\Big\}\,. \tag{6.2.9}$$

Here the dipole density $n(r,r',Y-y)d^2r'$ is the number of daughter dipoles of size r' in the interval d^2r' produced by a parent dipole of size r at the relative rapidity $Y-y$ [61, 62, 63]. It satisfies the BFKL equation [113, 114](see Chap. 3) with the initial condition

$$n(\boldsymbol{r},\boldsymbol{r}',0)=\delta(\boldsymbol{r}-\boldsymbol{r}')\,. \tag{6.2.10}$$

At the leading logarithmic order, the corresponding solution is [113, 114]

$$n(\boldsymbol{r},\boldsymbol{r}',y)=\frac{1}{2\pi^2r'^2}\int_{-\infty}^{\infty}d\nu\,e^{2\bar{\alpha}_s\chi(\nu)y}\left(\frac{r}{r'}\right)^{1+2i\nu} \tag{6.2.11}$$

with the eigevalue function χ given by

$$\chi(\nu)=\psi(1)-\frac{1}{2}\psi\left(\frac{1}{2}-i\nu\right)-\frac{1}{2}\psi\left(\frac{1}{2}+i\nu\right)\,, \tag{6.2.12}$$

where $\psi(\nu)=\Gamma'(\nu)/\Gamma(\nu)$. In the diffusion approximation to the leading order BFKL equation [113, 114] it is given by:

$$n(r,r',Y-y)=\frac{1}{2\pi^2}\frac{1}{rr'}\sqrt{\frac{\pi}{14\zeta(3)\bar{\alpha}_s\,(Y-y)}}\,e^{(\alpha_P-1)(Y-y)}\,e^{-\frac{\ln^2\frac{r}{r'}}{14\zeta(3)\bar{\alpha}_s\,(Y-y)}}\,. \tag{6.2.13}$$

Nuclear modification factor R_{AB} for coherent diffractive gluon production in the quasi-classical approximation evolution is suppressed for large nuclei and large dipoles as $R_{q\bar{q}+A}\sim A^{1/3}\exp\{-r^2Q_s^2/4\}$ (modulo logs) for dipole–nucleus scattering. We refer the reader to [100] for detailed discussion on that. Effect of quantum evolution is twofold. The smaller x of nucleus, i.e. the larger is rapidity of the produced gluon y, the stronger is the coherence effect that makes growth of the diffractive cross section in dipole–nucleus scattering slower than in dipole–proton one and, as a result, the nuclear modification

factor gets an additional suppression in the γ^* fragmentation region (forward rapidity). On the other hand, at large $Y - y$, the dipole density (6.2.13) in the virtual photon γ^* spreads to a wider range of sizes r'. Apparently, dipoles with sizes $r' \ll 2/Q_s$ are not suppressed at all. This effect leads to enhancement of the nuclear modification factor in the backward rapidity. This leads to a strong energy dependence of the cross section that we discuss in the next section.

6.3 Numerical calculations

A convenient way to express the nuclear effect on diffractive scattering is to introduce the nuclear modification factor as a ratio of the diffractive cross sections in DIS on a nucleus per nucleon and on a proton [100], also see Sec. 5.7:

$$R_{\rm cd/id} = \frac{\frac{d\sigma^{\gamma^* A}_{\rm cd/id}(Q^2,x,k,y)}{d^2k\,dy}}{A\,\frac{d\sigma^{\gamma^* p}_{\rm cd/id}(Q^2,x,k,y)}{d^2k\,dy}}\,. \tag{6.3.1}$$

The cross section appearing in (6.3.1) are partonic cross sections (6.2.6) and (6.2.8) convoluted with the LO pion fragmentation function given in [152].

We performed numerical calculations with the b-CGC model of the scattering amplitude N [143] with a modification: we treat the nuclei and proton profiles as step-functions; the saturation scales are assumed to scale with A as $Q_s^2 \propto A^{1/3}$. The advantage of this model is that (i) its form complies with the known analytical approximations to the BK equation and (ii) its parameters are fitted to the small-x DIS data.

Our results are presented in Fig. 6.2 which exhibits dependence of the nuclear modification factor for coherent (left column) and incoherent (right column) hadron production on transverse momentum $\boldsymbol{k}$. We assumed that the center-of-mass energy of the $\gamma^* A$ collision is $W = 100$ GeV per proton, which corresponds to the total rapidity interval $Y = 9.2$.

In Fig. 6.2 (a,b) we show variation of the nuclear modification factor with the nuclear

weight. We observe that $R_{\rm cd}$ increases with A. This is a signature behavior of higher twist effects and, in particular, coherent diffraction. In view of the discussion at the end of the previous section, we infer that the effective dipole size r' produced in the dipole evolution is $r' \ll 2/Q_s$, for otherwise the cross section would decrease for heavier nuclei. As one can see in Fig. 6.2 (e,f), NMF has no significant Q^2 dependence, and hence no r dependence as well. Therefore, even at higher y, where evolution effects in the nucleus as well as lack of evolution in γ^* could have produced suppression of $R_{\rm cd}$ with A, no such suppression is observed. We checked this statement up to the most forward direction allowed by our model $\beta = 0.1$. $R_{\rm id}$ decreases with A already at midrapidity $y = 5$ because the general property of incoherent diffraction is that it vanishes in the limit $A \to \infty$ when all partial amplitudes turn black.

Rapidity dependence is displayed in Fig. 6.2 (c,d). $R_{\rm cd}$ rapidly decreases in the forward direction, which is a cumulative effect of evolution in the nucleus and in the virtual photon, whereas $R_{\rm id}$ is essentially rapidity independent. This effect has already been noticed in pA case [101]. It arises because of different physical origins of the two diffractive processes. Coherent diffraction corresponds to elastic scattering of a color dipole on a nucleus, whereas incoherent diffraction is a part of inelastic scattering that originates from the nuclear periphery due to variation of the nuclear density with impact parameter. At low x central impact parameters of a heavy nucleus are black for a typical dipole. Therefore, scattering amplitude of dipole on a heavy nucleus is very different from an incoherent superposition of dipole-nucleon scattering amplitudes, hence strong variation of the nuclear modification factor with energy/rapidity. On the other hand, incoherent diffraction is non-zero only in the range of impact parameters comparable with the proton radius. Therefore, energy/rapidity dependence of dipole-nucleus and dipole-proton cross section is similar, though the geometry is quite different.

Finally, Fig. 6.2 (e,f) exhibits dependence on photon virtuality Q^2, or perhaps better to say no dependence at all. This can be interpreted as insensitivity of the diffractive cross

sections to the size of the parent dipole r. Indeed, as explained in [99], at $k_\perp \gg Q_s, Q$ diffractive spectra depend only on $k_\perp$. For example, cross section for coherent diffractive gluon production in the asymptotic kinematic region $Q_s \ll 1/r \ll k$ reads (in the double-logarithmic approximation)

$$\frac{d\sigma^{q\bar{q}A}}{d^2k\,dy} = \frac{\alpha_s C_F S_A}{\pi^{5/2}k^2} N^2(1/k, b, y) \frac{1}{(2\bar{\alpha}_s(Y-y)\ln(rk))^{1/4}} e^{2\sqrt{2\bar{\alpha}_s(Y-y)\ln(rk)}}. \tag{6.3.2}$$

Clearly, r-dependence cancels out of the nuclear modification factor. Notice, however, that the EIC kinematic region can hardly be classified as asymptotic, and one would expect large corrections to (6.3.2). In fact, it is known that corrections to the double-logarithmic approximation are phenomenologically significant (see e.g. [154, 86]). However, our numerical calculations imply that they cancel in this particular case. Unfortunately, we are not able to extend this analysis to higher Q^2's without transgressing the region of applicability of our model. It would be interesting to analytically investigate the origin of this cancelation.

6.4 t-dependence

In this section we consider dependence of different diffraction channels on momentum transfer $\sqrt{-t}$. t-dependence translates into dependence on the scattering angle θ. While the dominant contribution to the diffractive cross sections stems from scattering at small angles, only angles larger than some cutoff angle θ_0 are experimentally accessible. Our goal in this section is to study the effect of cutoff angle on cross sections and nuclear modification factor introduced in the previous section.

6.4.1 Coherent diffraction

Consider dipole–nucleus elastic scattering amplitude $\Gamma^{q\bar{q}+A}(s, \boldsymbol{b}, \{\boldsymbol{b}_a\})$, where $\boldsymbol{b}$ is the dipole impact parameter and $\boldsymbol{b}_a$'s are positions of nucleons in the nucleus. Average over the nucleon positions will be denoted as $\left\langle \Gamma^{dA}(s, \boldsymbol{b}) \right\rangle$. Cross section for elastic dipole

scattering is

$$\sigma_{\rm cd}^{q\bar{q}+A} = \int d^2b \left|\left\langle \Gamma^{q\bar{q}+A}(s,\boldsymbol{b})\right\rangle\right|^2 . \tag{6.4.1}$$

In this representation this is also the coherent diffraction cross section. Fourier image of the dipole-nucleus elastic scattering amplitude carries information about the transferred momentum Δ such that $t = -\Delta^2 = \boldsymbol{\Delta}^2$:

$$\left\langle \Gamma^{q\bar{q}+A}(s,\boldsymbol{\Delta})\right\rangle = 2\int d^2b \left\langle \Gamma^{q\bar{q}+A}(s,\boldsymbol{b})\right\rangle e^{i\boldsymbol{b}\cdot\boldsymbol{\Delta}} . \tag{6.4.2}$$

If only two-body forces are taken into account in a scattering process (which amounts to neglecting correlations between nucleons), then we can express the scattering amplitude on a nucleus as through the scattering amplitudes on individual nucleons as

$$\Gamma^{q\bar{q}+A}(s,\boldsymbol{b},\{\boldsymbol{b}_a\}) = 1 - \prod_{a=1}^{A}\left(1-\Gamma^{q\bar{q}+N}(s,\boldsymbol{b}-\boldsymbol{b}_a)\right) . \tag{6.4.3}$$

In this approximation averaging can be performed as

$$\langle \ldots\rangle = \prod_{a=1}^{A}\int d^2b_a \int_{-\infty}^{\infty} dz\, \rho_A(\boldsymbol{b}_a,z)\ldots = \prod_{a=1}^{A}\int d^2b_a \rho T_A(\boldsymbol{b}_a)\ldots \tag{6.4.4}$$

where $\rho_A(\boldsymbol{b},z)$ is the nuclear density at a given point in the nucleus and ρ is its average over the nucleus volume.

Impact parameter profile of the dipole-nucleon amplitude is traditionally parameterized as

$$\Gamma^{q\bar{q}+N}(s,\boldsymbol{b}) = \frac{1}{2}\sigma_{\rm tot}^{q\bar{q}+N}(s)\,\frac{1}{\pi R_p^2}e^{-b^2/R_p^2} , \tag{6.4.5}$$

where we neglected a small imaginary part of $\Gamma^{q\bar{q}+N}(s,\boldsymbol{b})$. In a heavy nucleus of radius $R_A \gg R_p$, nucleon can be approximated by a delta function in impact parameter space. Thus,

$$\int d^2b_a \Gamma^{q\bar{q}+N}(s,\boldsymbol{b}-\boldsymbol{b}_a)\,\rho T_A(\boldsymbol{b}_a) \approx \rho\Gamma^{q\bar{q}+N}(s,0)\,\rho T_A(\boldsymbol{b}) . \tag{6.4.6}$$

Using (6.4.4),(6.4.5),(6.4.6) in (6.4.3) we derive for heavy nuclei

$$\left\langle \Gamma^{q\bar{q}+A}(s,\boldsymbol{b})\right\rangle = 1 - e^{-\frac{1}{2}\sigma_{\rm tot}^{q\bar{q}+N}(s)\rho T_A(b)} \tag{6.4.7}$$

Finally, substituting (6.4.7) into (6.4.2) and (6.4.1) we derive

$$\frac{d\sigma_{\rm cd}^{q\bar{q}+A}}{dt} = \frac{1}{16\pi}\left|2\int d^2b\left(1-e^{-\frac{1}{2}\sigma_{\rm tot}^{q\bar{q}+N}(s)\rho T_A(b)}\right)e^{i\boldsymbol{b}\cdot\boldsymbol{\Delta}}\right|^2 . \tag{6.4.8}$$

To estimate the t-dependence of the coherent cross section we use we can use a simple model for the b distribution. Denote $\frac{1}{2}\sigma_{\rm tot}^{q\bar{q}+N}(s)\rho T_A(b) = \Omega S(b)$ and let the profile function $S(b)$ be given be the step function $S(b) = \theta(R_A - b)$. Neglecting contribution of the nucleus diffusion reason is a reasonable approximation in the case of coherent diffraction because the main contribution stems from $b < R_A$ impact parameters. Substituting into (6.4.8) and (6.4.1) we get

$$\frac{d\sigma_{cd}^{q\bar{q}+A}}{dt}\frac{1}{\sigma_{cd}^{q\bar{q}+A}} = \frac{J_1^2(R_A\sqrt{-t})}{|t|} . \tag{6.4.9}$$

Because (6.4.9) does not depend on Ω this formula also gives t-dependence of the diffractive coherent gluon production.

6.4.2 Incoherent diffraction

Coherent diffraction includes only events in which nucleus stays intact. However, generally the nucleus can get excited and subsequently decay into colorless remnants. Total diffractive cross section is given by

$$\sigma_{\rm dif}^{q\bar{q}+A} = \int d^2b\left\langle\left|\Gamma^{q\bar{q}+A}(s,\boldsymbol{b})\right|^2\right\rangle . \tag{6.4.10}$$

The difference between (6.4.10) and (6.4.1) measures dispersion of the scattering amplitude in the impact parameter space. The corresponding physical process is a part of inelastic cross section is called incoherent diffraction:

$$\sigma_{\rm id}^{q\bar{q}+A} = \int d^2b\left\langle\left|\Gamma^{q\bar{q}+A}(s,\boldsymbol{b})\right|^2\right\rangle - \left|\left\langle\Gamma^{q\bar{q}+A}(s,\boldsymbol{b})\right\rangle\right|^2 . \tag{6.4.11}$$

Clearly, the incoherent diffraction stems from the region near the nucleus edge ('diffusion region') since at $b \ll R_A$ the dipole-nucleon amplitudes are all close to the black limit, while at $b \gg R_A$ they all vanish.

To derive $t-$dependence of the incoherent diffraction cross section we define similarly to (6.4.2)

$$\Gamma^{q\bar{q}+A}(s,\mathbf{\Delta},\{\boldsymbol{b}_a\}) = 2\int d^2b\,\Gamma^{q\bar{q}+A}(s,\boldsymbol{b},\{\boldsymbol{b}_a\})e^{i\boldsymbol{b}\cdot\mathbf{\Delta}}\,. \tag{6.4.12}$$

Then (6.4.10) reads:

$$\begin{aligned}
\frac{d\sigma_{\rm dif}}{dt} &= \frac{1}{16\pi}\left\langle\left|\Gamma^{q\bar{q}+A}(s,\mathbf{\Delta},\{\boldsymbol{b}_a\})\right|^2\right\rangle &(6.4.13)\\
&= \frac{1}{4\pi}\int d^2b\int d^2b' e^{i\mathbf{\Delta}\cdot(\boldsymbol{b}-\boldsymbol{b}')}\times\\
&\quad\times\left\langle\left[1-\prod_{a=1}^{A}\left(1-\Gamma^{q\bar{q}+N}(s,\boldsymbol{b}-\boldsymbol{b}_a)\right)\right]\left[1-\prod_{a=1}^{A}\left(1-\Gamma^{q\bar{q}+N}(s,\boldsymbol{b}'-\boldsymbol{b}_a)\right)\right]^{\dagger}\right\rangle\\
&= \frac{1}{4\pi}\int d^2b\int d^2b' e^{i\mathbf{\Delta}\cdot(\boldsymbol{b}-\boldsymbol{b}')}\left[1-e^{-\sum_a\left\langle\Gamma^{q\bar{q}+A}(s,\boldsymbol{b}-\boldsymbol{b}_a)\right\rangle}-e^{-\sum_a\left\langle\Gamma^{q\bar{q}+A}(s,\boldsymbol{b}'-\boldsymbol{b}_a)\right\rangle}\right.\\
&\quad\left.+e^{-\sum_a\left\langle\Gamma^{q\bar{q}+A}(s,\boldsymbol{b}-\boldsymbol{b}_a)\right\rangle+\sum_a\left\langle\Gamma^{q\bar{q}+A}(s,\boldsymbol{b}'-\boldsymbol{b}_a)\right\rangle-\left\langle\Gamma^{q\bar{q}+A}(s,\boldsymbol{b}-\boldsymbol{b}_a)\Gamma^{q\bar{q}+A}(s,\boldsymbol{b}'-\boldsymbol{b}_a)\right\rangle}\right] &(6.4.14)
\end{aligned}$$

Subtracting the coherent diffraction part

$$\frac{d\sigma_{\rm cd}}{dt} = \frac{1}{4\pi}\int d^2b\int d^2b' e^{i\mathbf{\Delta}\cdot(\boldsymbol{b}-\boldsymbol{b}')}\left(1-e^{-\sum_a\left\langle\Gamma^{q\bar{q}+A}(s,\boldsymbol{b}-\boldsymbol{b}_a)\right\rangle}\right)\left(1-e^{-\sum_a\left\langle\Gamma^{q\bar{q}+A}(s,\boldsymbol{b}'-\boldsymbol{b}_a)\right\rangle}\right) \tag{6.4.15}$$

we end up with

$$\begin{aligned}
\frac{d\sigma_{\rm id}}{dt} &= \frac{1}{4\pi}\int d^2b\int d^2b' e^{i\mathbf{\Delta}\cdot(\boldsymbol{b}-\boldsymbol{b}')}\left[1-e^{-\sum_a\left\langle\Gamma^{q\bar{q}+A}(s,\boldsymbol{b}-\boldsymbol{b}_a)\Gamma^{q\bar{q}+A}(s,\boldsymbol{b}'-\boldsymbol{b}_a)\right\rangle}\right]\\
&\quad\times e^{-\sum_a\left[\left\langle\Gamma^{q\bar{q}+A}(s,\boldsymbol{b}-\boldsymbol{b}_a)\right\rangle+\left\langle\Gamma^{q\bar{q}+A}(s,\boldsymbol{b}'-\boldsymbol{b}_a)\right\rangle-\left\langle\Gamma^{q\bar{q}+A}(s,\boldsymbol{b}-\boldsymbol{b}_a)\Gamma^{q\bar{q}+A}(s,\boldsymbol{b}'-\boldsymbol{b}_a)\right\rangle\right]} &(6.4.16)
\end{aligned}$$

Since elastic cross section is small we expand as

$$\begin{aligned}
\frac{d\sigma_{\rm id}}{dt} &= \frac{1}{4\pi}\int d^2b\int d^2b' e^{i\mathbf{\Delta}\cdot(\boldsymbol{b}-\boldsymbol{b}')}e^{-\sum_a\left[\left\langle\Gamma^{q\bar{q}+A}(s,\boldsymbol{b}-\boldsymbol{b}_a)\right\rangle+\left\langle\Gamma^{q\bar{q}+A}(s,\boldsymbol{b}'-\boldsymbol{b}_a)\right\rangle\right]}\\
&\quad\times\sum_a\left\langle\Gamma^{q\bar{q}+A}(s,\boldsymbol{b}-\boldsymbol{b}_a)\Gamma^{q\bar{q}+A}(s,\boldsymbol{b}'-\boldsymbol{b}_a)\right\rangle &(6.4.17)\\
&= \frac{1}{4\pi}\int d^2b_a\left|\int d^2b\, e^{i\mathbf{\Delta}\cdot\boldsymbol{b}}e^{-\rho T_A(b)\Gamma^{q\bar{q}+A}(s,0)}\Gamma^{q\bar{q}+A}(\boldsymbol{b}-\boldsymbol{b}_a)\right|^2\rho T_A(\boldsymbol{b}_a) &(6.4.18)
\end{aligned}$$

Since $|\boldsymbol{b}-\boldsymbol{b}_a|\sim R_p \ll b_a\sim R_A$, we can get

$$\frac{d\sigma_{\rm id}}{dt} = \frac{1}{4\pi}\int d^2b_a\, e^{-2\rho T_A(b_a)\Gamma^{q\bar{q}+A}(s,0)}\left|\int d^2b\, e^{i\mathbf{\Delta}\cdot\boldsymbol{b}}\Gamma^{q\bar{q}+A}(\boldsymbol{b})\right|^2\rho T_A(\boldsymbol{b}_a)\,. \tag{6.4.19}$$

Using (6.4.5)

$$\frac{d\sigma_{\rm id}}{dt} = \frac{1}{4\pi}\frac{\sigma_{\rm tot}^{q\bar{q}+N}(s)}{2}e^{-\frac{1}{2}tR_p^2}\int d^2b_a\, e^{-2\rho T_A(b_a)\Gamma^{q\bar{q}+A}(s,0)}\rho T_A(\boldsymbol{b}_a) = \frac{R_p^2}{2}e^{-\frac{1}{4}|t|R_p^2}\,\sigma_{\rm id}\,. \quad (6.4.20)$$

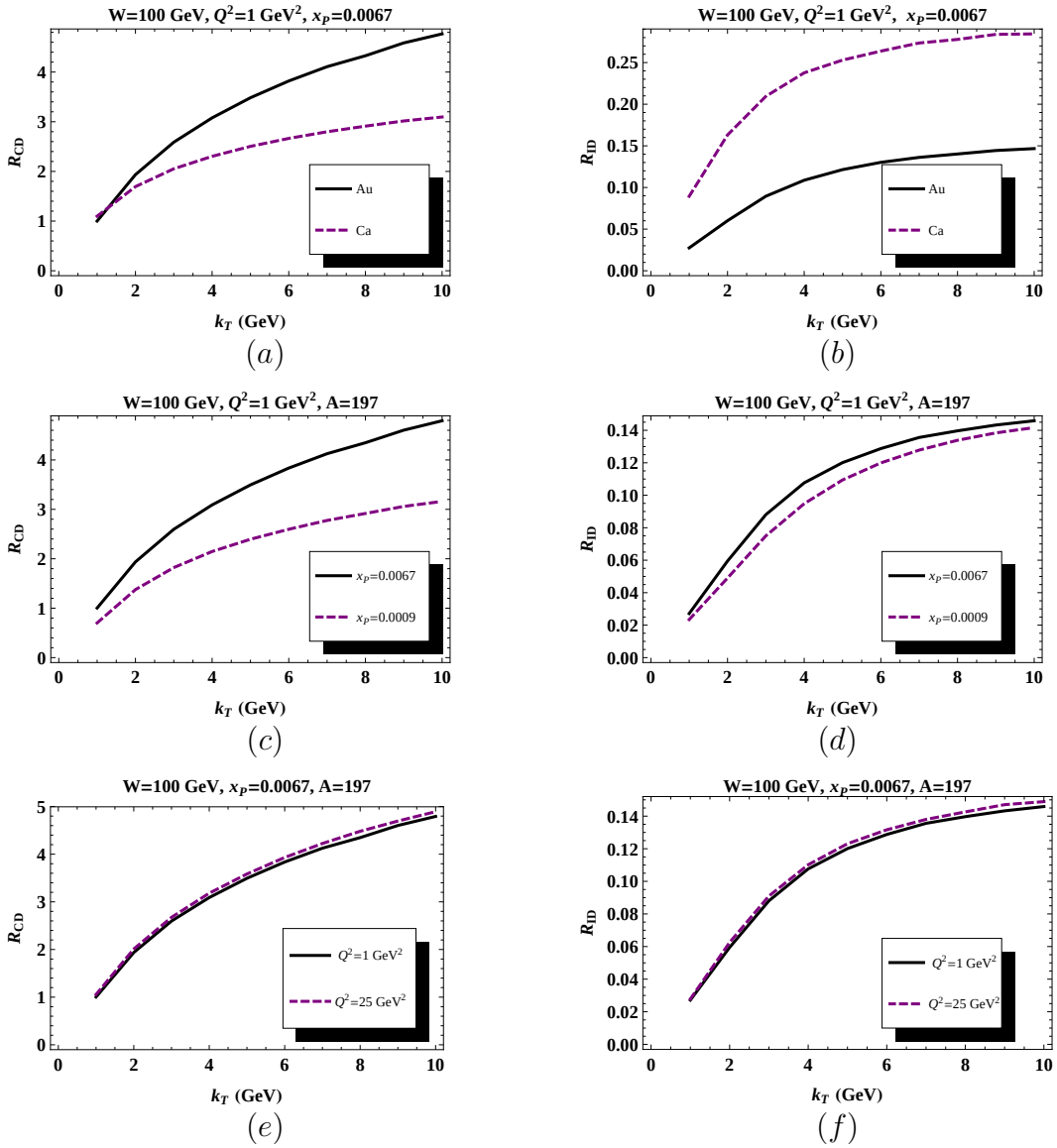

Figure 6.2 Nuclear modification factors for coherent (left column) and incoherent (right column) diffractive hadron production at $W = 100$ GeV as a function at of the hadron transverse momentum k. Shown are dependences on: (a),(b) atomic number A, (c),(d) hadron rapidity y and (e),(f) photon virtuality Q^2.

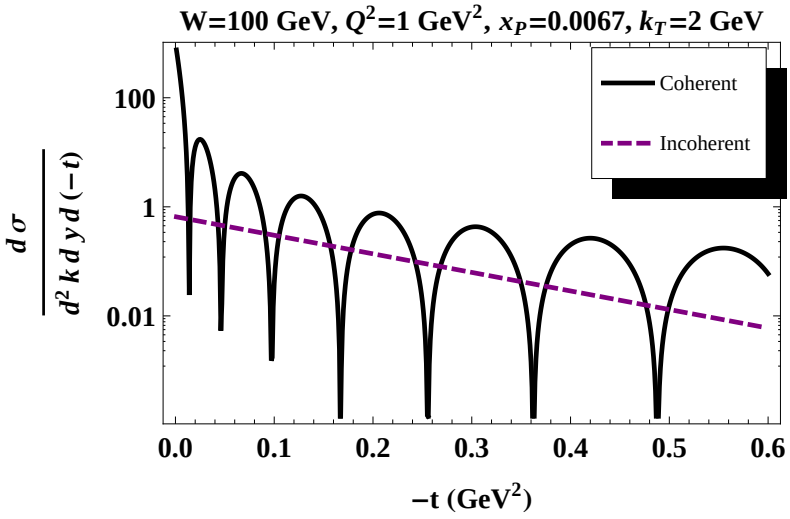

Figure 6.3 t-dependence of coherent vs incoherent diffractive gluon production

CHAPTER 7. Inclusive gluon production in DIS at small-x

7.1 Introduction

In the last decade we have learned a great deal about gluon saturation/color glass condensate [56, 60, 57, 61, 62, 63, 64, 58, 65, 59, 66, 67, 68, 69, 70, 71, 72, 73, 74, 75, 76, 77, 78, 79, 80, 81] thanks to the relativistic dAu and $AuAu$ program at RHIC. The future DIS programs at EIC and LHeC promise to provide even more detailed information about structure of the nuclear matter at low x. How successful that program will be depends a lot on our ability to pinpoint the processes that are most sensitive to the low-x regime. In this chapter we study one such process – inclusive hadron production in eA scattering. It has been a subject of intense theoretical investigation over the past decade [102, 103, 104, 105, 106, 107, 108, 109, 110, 111] and has proved to be a powerful tool in dA collisions at RHIC. On the one hand, we expect that $p(d)A$ and eA processes have very much in common due to the Pomerantchuk theorem, that states that all high energy scattering processes are mediated by exchange of a collective gluon state – known as pomeron – that has vacuum quantum numbers. On the other hand, proton wave function is characterized by a soft, non-perturbative scale, whereas the virtual photon wave function can be calculated using the perturbation theory and is characterized by virtuality Q^2. A possibility to dial Q^2 is a great advantage of DIS. Our main goal in this chapter is to provide a thorough analysis of the inclusive hadron production in various kinematic regions characterized by three dimensional scales: photon virtuality Q^2, hadron momentum k_T and the saturation momentum Q_s and to produce numerical

predictions for both novel and well-known quantities that can be tested at EIC and/or LHeC.

This chapter is organized as follows. In Sec. 7.2 we use the dipole model [112] to relate the DIS $\gamma^* A$ cross section to that of the color dipole $q\bar{q} + A$. The $\gamma^* A$ differential cross section can be expressed in a factorized form as a product of the light-cone wave function of the virtual photon γ^* and $q\bar{q}+A$ differential cross section. In Sec. 7.3 we review the properties of the BFKL pomeron [113, 114] and the unintegrated gluon distribution function at LO, particularly we emphasize the leading logarithmic asymptotics. These are used in Sec. 7.4 to derive the asymptotic properties of gluon production in dipole–nucleus scattering in various kinematic regions. In Sec. 7.5 the result is further generalized to the case of LO gluon production in DIS.

The NLO corrections to the inclusive hadron production are rather complex. These include NLO correction to the BFKL kernel [115, 116], [119, 121, 120, 122, 123, 124, 125, 126, 127, 128], running coupling corrections [129, 135, 136, 130, 131, 134, 132, 133] and momentum conservation [137, 138, 139] corrections to BK [76, 77, 78, 79]. It has been argued in [140] that momentum conservation is the most important phenomenological effect beyond the LO. Therefore, in Sec. 7.6 we investigate the role of this effect on inclusive hadron production. In our calculations we rely on a phenomenological approach suggested in [140, 141] where a modified BK (mBK) equation that satisfies energy conservation was derived. It was utilized in [142, 137] to calculate the NLO corrections to the total DIS cross section. mBK equation serves as the basis for our NLO calculations. First, we derive the dipole scattering amplitude in dilute and saturation regimes; the corresponding expressions are given by (7.6.15) and (7.6.28) respectively. We argue that the energy conservation effects decrease the energy dependence of the saturation momentum. These results are used for computation of dipole density in various asymptotic regimes. Similarly to our analysis of LO case, we explore the NLO gluon production first for dipole—nucleus process and then for DIS scattering.

It is very instructive to know how the DIS on a heavy nucleus is different from DIS on a proton at low x. Had the coherence length been short, of the order of the proton radius, the hadron production in $\gamma^* A$ would have been equal the incoherent sum of A $\gamma^* N$ processes. However, since the coherence length is larger than the nuclear radius, the entire process is coherent. Because it is interesting to compare the coherent and incoherent regimes, one introduces the nuclear modification factor (NMF) R that calibrates the cross section in $\gamma^* A$ with that of $\gamma^* N$ rescaled by atomic weight A. Sec. 7.7 is devoted to the study of the properties of this quantity as a function of the hadron transverse momentum, photon virtuality and atomic weight.

We expect that at EIC/LHeC kinematic region the low-x evolution effects start to play an important role rendering the anomalous dimensions dependent on atomic weight. This manifests itself in inclusive hadron production in dA collisions at RHIC as the transition from the Cronin enhancement at mid-rapidity to suppression of the NMF at forward rapidities even at $k_T > Q_s$. In order to evaluate how steep is the dependence of the NMF on rapidity, we introduce a new observable J, defined as the logarithmic derivative of R, viz. $d \ln R/dy$. We demonstrate in Sec. 7.7 that at $k_T \gg Q_s$, J is proportional to the difference of the anomalous dimensions of the gluon distribution in nucleus and in proton. Without the low-x evolution one expect J to vanish. However, due to the low-x evolution J acquires a finite negative value. Therefore, J can serve as a direct probe of the effect of the slow-x evolution on the nuclear gluon distribution function.

The numerical computations are presented in Sec. 7.8. We use the bCGC model [143] for the dipole-nucleus forward scattering amplitude, albeit with the simplified b-dependence. In Fig. 7.5 we plot $d^2F_2/d\ln k_T^2\, dy$ as a function of photon virtuality Q^2 and hadron transverse momentum k_T and rapidity $y = \ln(1/x_{\mathbb{P}})$.* In order to emphasize the role played by the NLO effects we exhibit both LO and NLO results in each plot

*We use the $x_{\mathbb{P}}$ notation borrowed from the diffractive DIS where it denotes the momentum fraction carried by the pomeron. It does not have this simple interpretation in our case because the interaction is inelastic.

for the structure function. In Fig. 7.5 we see that the NLO calculation yields much smaller cross section for inclusive hadron production than the LO one. Additionally, its functional dependence on k_T, Q^2 and y is substantially weaker in NLO than in LO. This is in accordance with our observation in Sec. 7.6 that NLO correction reduces the anomalous dimension of the gluon distribution. Interestingly, most of the NLO effect cancels in the NMF which appears to be a robust quantity in this respect. This indicates that the momentum conservation effect factors out to a large extent from the inclusive cross section.

The NMF shown in Fig. 7.7 displays a number of interesting features. First, the NMF is strongly suppressed at small k_T's but exhibits an enhancement toward higher k_T's where the Cronin effect ($R > 1$) is observed. This seems to be in contrast with pA collisions [108] where the Cronin effect gives way to suppression of NMF at all k_T's as the hadron rapidity increases. This is the result of the linear evolution in the rapidity interval between the virtual photon and the hadron. This evolution produces dipoles of different sizes that scatter in the nucleus with different amplitudes. At small k_T large dipoles, on which the gluon saturation effects are stronger, dominate the cross section, whereas at higher k_T smaller dipoles contribute to the NMF enhancement. Second, we observe a relatively weak A-dependence. This is also a result of the averaging over different dipoles. Third, we note a peculiar Q^2 dependence that is explained in Sec. 7.8.

To investigate the rapidity dependence in more detail we plot the logarithmic slope of the nuclear modification factor J on Fig. 7.8 (for dipole-nucleus scattering). We see that it is negative for the entire kinematic region indicating the graduate suppression of the NMF towards large rapidities. This is in agreement with our arguments in Sec. 7.7. We argue that J is directly proportional to the difference between the anomalous dimensions of the gluon distribution function in the nucleus and in proton. Hence we believe that measuring J is a great tool for exploring the low-x regime of QCD.

7.2 From $\gamma^* A$ to $q\bar{q} + A$ scattering

The dominant contribution to the inclusive hadron production in DIS at small-x, at rapidities away from the virtual photon and nucleus fragmentation regions, comes from the fragmentation of fast s-channel gluons [60]. The cross section for inclusive production of a gluon of transverse momentum $\boldsymbol{k}$ at rapidity y in deep inelastic scattering can be represented as an integral in the configuration space [144]:

$$\frac{d\sigma^{\gamma^* A}(\boldsymbol{k}, y; Q)}{d^2k dy} = \frac{1}{2\pi^2} \int d^2r \int_0^1 dz\, \Phi(\boldsymbol{r}, z, Q)\, \frac{d\sigma^{q\bar{q}+A}(\boldsymbol{k}, y; \boldsymbol{r})}{d^2k dy}\,, \tag{7.2.1}$$

where the virtual photon wave function Φ describes splitting of a photon of virtuality Q^2 into $q\bar{q}$ color dipole. It is given by (5.2.9)and(5.2.11) The cross section for inclusive gluon production in dipole–nucleus scattering reads [103]

$$\frac{d\sigma^{q\bar{q}+A}(\boldsymbol{k}, y; \boldsymbol{r})}{d^2k dy} = \frac{2\alpha_s C_F}{\pi^2} \frac{1}{k^2} \int d^2b \int d^2r' e^{-i\boldsymbol{k}\cdot\boldsymbol{r}'} [\nabla^2_{r'} N_G(\boldsymbol{r}', \boldsymbol{b}', y)]\, [\nabla^{-2}_{r'} n(\boldsymbol{r}, \boldsymbol{r}', Y - y)]\,, \tag{7.2.2}$$

Here the dipole density $n(r, r', Y - y)d^2r'$ is the number of daughter dipoles of size r' in the interval d^2r' produced by a parent dipole of size r at the relative rapidity $Y - y$(see (6.2.11)).

Let $f(\boldsymbol{r}, \boldsymbol{r}', y)$ be the particular solution of the two-dimensional Poisson equation

$$\nabla^2_{r'} f(\boldsymbol{r}, \boldsymbol{r}', y) = n(\boldsymbol{r}, \boldsymbol{r}', y)\,. \tag{7.2.3}$$

Employing (6.2.11) we derive the Mellin representation of f

$$f(\boldsymbol{r}, \boldsymbol{r}', y) = \nabla^{-2}_{r'} n(\boldsymbol{r}, \boldsymbol{r}', y) = \frac{1}{2\pi^2} \int_{-\infty}^{\infty} d\nu\, \frac{1}{(2i\nu + 1)^2}\, e^{2\bar{\alpha}_s \chi(\nu) y} \left(\frac{r}{r'}\right)^{1+2i\nu}\,. \tag{7.2.4}$$

It is convenient to write (7.2.2) as a convolution in the momentum space. To this end we introduce the Fourier-image of f with respect to the second argument:

$$\tilde{f}(\boldsymbol{r}, \boldsymbol{q}, y) = \int d^2r'\, e^{-i\boldsymbol{q}\cdot\boldsymbol{r}'}\, f(\boldsymbol{r}, \boldsymbol{r}', y) = \frac{r}{\pi q} \int_{-\infty}^{\infty} d\nu\, e^{2\bar{\alpha}_s \chi(\nu) y} \left(\frac{rq}{2}\right)^{2i\nu} \frac{\Gamma\left(\frac{1}{2} - i\nu\right)}{\Gamma\left(\frac{1}{2} + i\nu\right)(2i\nu + 1)^2} \tag{7.2.5}$$

and the unintegrated gluon distribution function of the nucleus [60, 103]

$$\varphi_A(\boldsymbol{k}, y) = \frac{C_F}{\alpha_s (2\pi)^3} \int d^2b \int d^2r\, e^{-i\boldsymbol{k}\cdot\boldsymbol{r}}\, \nabla_r^2 N_G(\boldsymbol{r}, \boldsymbol{b}, y)\,. \tag{7.2.6}$$

$N_G(\boldsymbol{r}, \boldsymbol{b}, y)$ is the forward scattering amplitude of a gluon dipole $\boldsymbol{r}$ on the nucleus at impact parameter $\boldsymbol{b}$ at the relative rapidity y. In the large-N_c approximation, it obeys the BK equation [78, 76] and its properties are discussed in the next section. Using (7.2.5) and (7.2.6) in (7.2.2) we get

$$\frac{d\sigma^{q\bar{q}+A}(\boldsymbol{k}, y; \boldsymbol{r})}{d^2k dy} = \frac{4\alpha_s^2}{\pi k^2} \int d^2p\, \varphi_A(\boldsymbol{p}, y)\, \tilde{f}(\boldsymbol{r}, \boldsymbol{k}-\boldsymbol{p}, Y-y)\,. \tag{7.2.7}$$

7.3 Logarithmic approximations

7.3.1 Asymptotic expressions for $\tilde{f}$

It is worthwhile to list here the asymptotic formulae for $\tilde{f}$ in various kinematic regions (we follow notations of [88, 99, 100] where more details can be found).

1. $\alpha_s y \gg \ln^2 \frac{rq}{2}$. In this case the eigenfunction (6.2.12) can be expanded near its minimum $\chi \approx 2\ln 2 - 7\zeta(3)\nu^2$. Expression under the ν-integral in (7.2.4) has a saddle point at

$$i\nu_{\rm sp} = \frac{\ln(2/rq)}{14\zeta(3)\bar{\alpha}_s y}\,. \tag{7.3.1}$$

In this approximation integration over ν in (7.2.4) produces

$$\tilde{f}(\boldsymbol{r}, \boldsymbol{q}, y) = \frac{r}{q} \frac{1}{\sqrt{14\pi\zeta(3)\bar{\alpha}_s\, y}}\, e^{(\alpha_P^{(0)}-1)y}\, e^{-\frac{\ln^2 \frac{rq}{2}}{14\zeta(3)\bar{\alpha}_s\, y}}\,, \tag{7.3.2}$$

with $\alpha_P^{(0)} - 1 = 4\bar{\alpha}_s \ln 2$.

2. $rq < 2$ and $\ln \frac{2}{rq} \gg \alpha_s y$. In this region, the leading contribution to the ν-integral stems from the pole at $i\nu = 1/2$. Approximating the eigenfunction as $\chi \approx 1/(1 - 2i\nu)$ and employing the saddle point method in (7.2.4) again yields

$$\tilde{f}(\boldsymbol{r}, \boldsymbol{q}, y) = \frac{r^2}{8\sqrt{\pi}} \frac{1}{\left(2\bar{\alpha}_s y \ln \frac{2}{rq}\right)^{1/4}} e^{2\sqrt{2\bar{\alpha}_s y \ln \frac{2}{rq}}}\,. \tag{7.3.3}$$

The saddle point is

$$2i\nu_{\rm sp} = 1 - \sqrt{\frac{2\bar{\alpha}_s y}{\ln\frac{2}{rq}}}\,. \tag{7.3.4}$$

3. $rq > 2$ and $\ln\frac{rq}{2} \gg \alpha_s y$. Now, another pole in χ dominates, $\chi \approx 1/(1+2i\nu)$ with the result for $\tilde{f}$

$$\tilde{f}(\boldsymbol{r},\boldsymbol{q},y) = \frac{1}{2q^2\sqrt{\pi}}\frac{1}{\left(2\bar{\alpha}_s y\ln\frac{rq}{2}\right)^{1/4}}e^{2\sqrt{2\bar{\alpha}_s y\ln\frac{rq}{2}}} \tag{7.3.5}$$

and for the saddle point

$$2i\nu_{\rm sp} = -1 + \sqrt{\frac{2\bar{\alpha}_s y}{\ln\frac{rq}{2}}}\,. \tag{7.3.6}$$

7.3.2 Properties of φ_A

Unintegrated gluon distribution φ_A is defined by (7.2.6). $N_G(\boldsymbol{r},y,\boldsymbol{b})$ stands for the forward elastic gluon dipole scattering amplitude. At large N_c, the gluon dipole is equivalent to two $q\bar{q}$ dipoles each of which scatters with amplitude $N(\boldsymbol{r},y,\boldsymbol{b})$. Therefore,

$$N_G(\boldsymbol{r},\boldsymbol{b},y) = 2N(\boldsymbol{r},\boldsymbol{b},y) - N^2(\boldsymbol{r},\boldsymbol{b},y) \tag{7.3.7}$$

The $q\bar{q}$ scattering amplitude satisfies the BK equation [78, 76] and its properties are well-known. Initial condition for the BK equation is the GGM formula [112] for the forward scattering amplitude N of a $q\bar{q}$ color dipole on the nucleus discussed in Chap. 4) as the quasi-classical approximation of the scattering amplitude(c.f.(4.1.14)):

$$N(\boldsymbol{r},\boldsymbol{b},0) = 1 - e^{-\frac{1}{8}\boldsymbol{r}^2 Q_{s0}^2}\,. \tag{7.3.8}$$

The *gluon* saturation momentum [56] at initial rapidity $y=0$, which corresponds to the Bjorken variable x_0 such that $y = \ln\frac{x_0}{x}$, is related to gluon distribution function xG at $x = x_0$ as

$$Q_{s0}^2 = \frac{4\pi^2\alpha_s N_c}{N_c^2-1}\,\rho\,T(\boldsymbol{b})\,x_0 G(x_0, 1/\boldsymbol{r}^2)\,, \tag{7.3.9}$$

where ρ is the nuclear density, $T(\boldsymbol{b})$ is the nuclear thickness function as a function of the impact parameter $\boldsymbol{b}$. The gluon distribution function at the leading order in α_s, i.e. in the two-gluon exchange approximation, reads

$$xG(x,1/\boldsymbol{r}^2) = \frac{\alpha_s C_F}{\pi} \ln \frac{1}{\boldsymbol{r}^2 \Lambda^2}\,, \tag{7.3.10}$$

with Λ being some non-perturbative momentum scale characterizing the nucleon's wave function. Using (7.3.8) in (7.3.7) we derive the initial condition for the gluon dipole scattering amplitude

$$N_G(\boldsymbol{r},\boldsymbol{b},0) = 1 - e^{-\frac{1}{4}\boldsymbol{r}^2 Q_{s0}^2}\,. \tag{7.3.11}$$

Let us now list some properties of the amplitude N_G, see [88, 108] for details.

1. At $r \ll 1/Q_{s0}$ the BK equation reduces to the BFKL equation, which must be solved with the initial condition $N(\boldsymbol{r},\boldsymbol{b},0) \approx r^2 Q_{s0}^2/4$. Small dipoles scatter independently, perforce $N_G \approx 2N$. Thus, in this region

$$N_G(\boldsymbol{r},\boldsymbol{b},y) = \int_{-\infty}^{\infty} d\nu\, e^{2\bar{\alpha}_s \chi(\nu) y}\, (rQ_{s0})^{1+2i\nu}\, \frac{1}{8\pi} \frac{1 + (1-2i\nu)\ln\frac{Q_{s0}}{\Lambda}}{(1-2i\nu)^2}\,. \tag{7.3.12}$$

2. In particular, if $r \ll 1/Q_{s0}$ and $\ln \frac{1}{rQ_{s0}} \gg \alpha_s y$ the solution is

$$N_G(\boldsymbol{r},\boldsymbol{b},y) = \frac{\sqrt{\pi}}{8\pi} \frac{(\ln \frac{1}{rQ_{s0}})^{1/4}}{(2\bar{\alpha}_s y)^{3/4}} r^2 Q_{s0}^2 \left(1 + \sqrt{\frac{2\bar{\alpha}_s y}{\ln \frac{1}{rQ_{s0}}}} \ln \frac{Q_{s0}}{\Lambda}\right) e^{2\sqrt{2\bar{\alpha}_s y \ln \frac{1}{rQ_{s0}}}}\,. \tag{7.3.13}$$

3. For $r \ll 1/Q_{s0}$ and $\alpha_s y \gg \ln^2 \frac{1}{rQ_{s0}}$ we have

$$N_G(\boldsymbol{r},\boldsymbol{b},y) = \frac{rQ_{s0}}{4} \frac{\ln \frac{Q_{s0}}{\Lambda}}{\sqrt{14\zeta(3)\pi\bar{\alpha}_s y}} e^{(\alpha_P - 1)y}\, e^{-\frac{\ln^2(rQ_{s0})}{14\zeta(3)\bar{\alpha}_s y}} \tag{7.3.14}$$

4. The saturation region is characterized by the saturation momentum $Q_s(y)$. With the double logarithmic accuracy it reads [145, 146, 147]

$$Q_s(y) = Q_{s0} e^{2\bar{\alpha}_s y} \tag{7.3.15}$$

In the saturation region $r > 1/Q_s$, solution to the BK equation is [145, 146, 147]

$$N(\boldsymbol{r}, \boldsymbol{b}, y) = 1 - S_0 e^{-\frac{1}{8}\ln^2(r^2 Q_s^2)}\,, \tag{7.3.16}$$

where S_0 is a constant that can be determined by matching N from (7.3.16) with that of (7.3.12) at $r = 2/Q_s(y)$. Consequently,

$$N_G(\boldsymbol{r}, \boldsymbol{b}, y) = 1 - S_0^2 e^{-\ln^2(rQ_s)}\,, \tag{7.3.17}$$

where we utilized (7.3.7).

Eqs. (7.3.12)-(7.3.17) are derived with the logarithmic accuracy. We can calculate φ_A given by (7.2.6) in the same approximation as

$$\varphi_A(\boldsymbol{k}, y) \approx \frac{C_F}{\alpha_s (2\pi)^2} \int d^2b \int_0^{1/k} dr\, \frac{\partial}{\partial r}\left(r \frac{\partial}{\partial r} N_G(\boldsymbol{r}, \boldsymbol{b}, y)\right) = \frac{C_F}{\alpha_s (2\pi)^2 k} \int d^2b\, \frac{\partial}{\partial r} N_G(\hat{\mathbf{r}}/k, \boldsymbol{b}, y)\,. \tag{7.3.18}$$

We stress that this formula holds only in the asymptotic regions specified in 1-4 above; still this is a very useful approximation as it captures the most essential features of the unintegrated gluon distribution.

It is evident from (7.3.18), that in place of function $N_G(\boldsymbol{r}, \boldsymbol{b}, y)$ it is convenient to use function $\tilde{N}_G(k, b, y) = N_G(\hat{\mathbf{r}}/k, \boldsymbol{b}, y)$, where $\hat{\mathbf{r}} = \boldsymbol{r}/r$. In particular, $\partial N_G(\hat{\mathbf{r}}/k, b, y)/\partial r = -k^2 \partial \tilde{N}_G(k, \boldsymbol{b}, y)/\partial k$. Plugging (7.3.18) into (7.2.7) we obtain

$$\frac{d\sigma^{q\bar{q}+A}(\boldsymbol{k}, y; \boldsymbol{r})}{d^2k dy} = \frac{\alpha_s C_F}{\pi^3 k^2} \int d^2b \int d^2p\, \frac{\partial \tilde{N}_G(p, b, y)}{\partial \ln(1/p)}\, \tilde{f}(\boldsymbol{r}, \boldsymbol{p} - \boldsymbol{k}, Y - y)\,. \tag{7.3.19}$$

7.4 Properties of the dipole–nucleus cross section

To calculate the cross section for gluon production in dipole–nucleus scattering we need to evaluate the integral over the transverse momentum $\boldsymbol{p}$ in the right-hand-side of (7.3.19). It convenient to consider the inclusive cross section at a fixed impact parameter b:

$$g(\boldsymbol{k}, y, \boldsymbol{b}; \boldsymbol{r}) \equiv \frac{d\sigma^{q\bar{q}+A}(\boldsymbol{k}, y; \boldsymbol{r})}{d^2k dy\, d^2b} \left(\frac{\alpha_s C_F}{\pi^3 k^2}\right)^{-1} = \int d^2p\, \frac{\partial \tilde{N}_G(p, b, y)}{\partial \ln(1/p)}\, \tilde{f}(\boldsymbol{r}, \boldsymbol{p} - \boldsymbol{k}, Y - y)\,. \tag{7.4.1}$$

When taking the p-integral with the logarithmic accuracy in various kinematic regions, it is useful to keep in mind that (7.3.17), (7.3.12) imply that $\partial\tilde{N}_G/\partial\ln(1/p) \sim \ln(Q_s/p)$ $\exp\{-\ln^2(Q_s/p)\}$ if $p \ll Q_s$ and $\partial\tilde{N}_G/\partial\ln(1/p) \sim Q_s^2/p^2$ if $p \gg Q_s$, while (7.3.3),(7.3.5) indicate that $\tilde{f} \sim 1/k^2$ if $k \gg 1/r$ and $\tilde{f} \sim r^2$, if $k \ll 1/r$.

1. $k \gg Q_s \gg 2/r$. Due to the strong ordering of the relevant scales we have

$$g \approx 2\pi \int_{Q_s}^{k} dpp \frac{\partial\tilde{N}_G(p,b,y)}{\partial\ln(1/p)}\, \tilde{f}(\boldsymbol{r},\boldsymbol{k},Y-y)\,. \tag{7.4.2}$$

Using (7.3.12) we derive

$$\begin{aligned}\int_{Q_s}^{k} dpp \frac{\partial\tilde{N}_G(p,b,y)}{\partial\ln(1/p)} &= k^2 \int_{-\infty}^{\infty} d\nu\, e^{2\bar{\alpha}_s\chi(\nu)y} \left(\frac{Q_{s0}}{k}\right)^{1+2i\nu} \frac{1}{8\pi} \frac{1+(1-2i\nu)\ln\frac{Q_{s0}}{\Lambda}}{(1-2i\nu)^2} \frac{1+2i\nu}{1-2i\nu} \\ &\approx \frac{\sqrt{\pi}}{8\pi} \frac{(\ln\frac{k}{Q_{s0}})^{3/4}}{(2\bar{\alpha}_s y)^{5/4}} Q_{s0}^2 \left(1+\sqrt{\frac{2\bar{\alpha}_s y}{\ln\frac{k}{Q_{s0}}}}\ln\frac{Q_{s0}}{\Lambda}\right) e^{2\sqrt{2\bar{\alpha}_s y\ln\frac{k}{Q_{s0}}}}\,.\end{aligned} \tag{7.4.3}$$

Thus, it follows upon substitution of (7.3.5) and (7.4.3) into (7.4.2) and then into (7.3.19) that

$$\begin{aligned}\frac{d\sigma^{q\bar{q}+A}(\boldsymbol{k},y;\boldsymbol{r})}{d^2k\,dy} &= \frac{\alpha_s C_F}{8\pi^3 k^4} \int d^2b\, Q_{s0}^2 \frac{(\ln\frac{k}{Q_{s0}})^{3/4}}{(2\bar{\alpha}_s y)^{5/4}(2\bar{\alpha}_s(Y-y)\ln\frac{kr}{2})^{1/4}} \\ &\times \left(1+\sqrt{\frac{2\bar{\alpha}_s y}{\ln\frac{k}{Q_{s0}}}}\ln\frac{Q_{s0}}{\Lambda}\right) e^{2\sqrt{2\bar{\alpha}_s(Y-y)\ln\frac{kr}{2}}} e^{2\sqrt{2\bar{\alpha}_s y\ln\frac{k}{Q_{s0}}}}\end{aligned} \tag{7.4.4}$$

2. $k \gg 2/r \gg Q_s$. Repeating the by now familiar procedure yields

$$g \approx 2\pi \int_{Q_s}^{k} dpp \frac{\partial\tilde{N}_G(p,b,y)}{\partial\ln(1/p)}\, \tilde{f}(\boldsymbol{r},\boldsymbol{k},Y-y) \tag{7.4.5}$$

We observe that the cross section in this case is exactly the same as (7.4.4).

3. $Q_s \gg k \gg 2/r$:

$$g \approx 2\pi \int_{k}^{Q_s} dpp \frac{\partial\tilde{N}_G(p,b,y)}{\partial\ln(1/p)}\, \tilde{f}(\boldsymbol{r},\boldsymbol{p},Y-y) \tag{7.4.6}$$

With the help of (7.3.17) and (7.3.5) we get

$$g = 2rS_0^2 \int_{-\infty}^{\infty} d\nu \frac{1}{1+2i\nu}\, e^{\frac{2\bar{\alpha}_s(Y-y)}{1+2i\nu}} \int_{k}^{Q_s} dp\, e^{-\ln^2\frac{Q_s}{p}} \ln\frac{Q_s}{p} \left(\frac{rp}{2}\right)^{2i\nu} \tag{7.4.7}$$

Now, using $\tau = \ln \frac{Q_s}{p}$ in place of p

$$\int_k^{Q_s} dp\, e^{-\ln^2 \frac{Q_s}{p}} \ln \frac{Q_s}{p} p^{2i\mu} = Q_s^{2i\mu+1} \int_0^{\ln(Q_s/k)} d\tau\, \tau\, e^{-\tau^2-\tau(1+2i\mu)}$$
$$\approx Q_s^{2i\mu+1} \int_0^{\infty} d\tau\, \tau\, e^{-\tau^2} = \frac{1}{2} Q_s^{2i\mu+1}\,. \tag{7.4.8}$$

Putting everything together yields

$$\frac{d\sigma^{q\bar{q}+A}(\boldsymbol{k}, y; \boldsymbol{r})}{d^2k dy} = \frac{\bar{\alpha}_s C_F S_0^2}{\pi^{5/2} k^2} \int d^2b \frac{1}{(\ln \frac{rQ_s}{2})^{1/4} (2\bar{\alpha}_s (Y-y))^{1/4}} e^{2\sqrt{2\bar{\alpha}_s (Y-y) \ln \frac{rQ_s}{2}}} \tag{7.4.9}$$

4. $Q_s \gg 2/r \gg k$:

$$g \approx 2\pi \int_{2/r}^{Q_s} dpp \frac{\partial \tilde{N}_G(p, b, y)}{\partial \ln(1/p)} \tilde{f}(\boldsymbol{r}, \boldsymbol{p}, Y-y) \tag{7.4.10}$$

This case is similar to the previous one except the the lower limit of the integral in (7.4.7), k, is now replaced by $1/r$. However, for very large Q_s, the integral over p is independent of the lower limit of integration as is clear from (7.4.8). We conclude thereby that the cross section in this case coincides with (7.4.9).

5. $2/r \gg k \gg Q_s$:

$$g \approx 2\pi \int_{Q_s}^{k} dpp \frac{\partial \tilde{N}_G(p, b, y)}{\partial \ln(1/p)} \tilde{f}(\boldsymbol{r}, \boldsymbol{k}, Y-y) + 2\pi \int_k^{2/r} dpp \frac{\partial \tilde{N}_G(p, b, y)}{\partial \ln(1/p)} \tilde{f}(\boldsymbol{r}, \boldsymbol{p}, Y-y) \tag{7.4.11}$$

The first of these integrals reads using (7.4.3) and (7.3.3)

$$2\pi \int_{Q_s}^{k} dpp \frac{\partial \tilde{N}_G(p, b, y)}{\partial \ln(1/p)} \tilde{f}(\boldsymbol{r}, \boldsymbol{k}, Y-y)$$
$$= \frac{1}{32} \frac{(\ln \frac{k}{Q_{s0}})^{3/4}}{(2\bar{\alpha}_s y)^{5/4}} \frac{1 + \sqrt{\frac{2\bar{\alpha}_s y}{\ln \frac{k}{Q_{s0}}}} \ln \frac{Q_{s0}}{\Lambda}}{\left(2\bar{\alpha}_s (Y-y) \ln \frac{2}{rQ_{s0}}\right)^{1/4}} Q_{s0}^2 r^2\, e^{2\sqrt{2\bar{\alpha}_s y \ln \frac{k}{Q_{s0}}}}\, e^{2\sqrt{2\bar{\alpha}_s (Y-y) \ln \frac{2}{rQ_{s0}}}} \tag{7.4.12}$$

The second one is done by substituting (7.3.13) and the integral form (7.2.5) (it is useful to note that $\partial \tilde{N}_G / \partial \ln(1/p) \approx 2\tilde{N}_G$) and then integrating over p in the

leading log approximation (i.e. treating $\log p$ as a constant) followed by the saddle point integral over ν. We have

$$\begin{aligned}
&2\pi \int_k^{2/r} dpp \frac{\partial \tilde{N}_G(p,b,y)}{\partial \ln(1/p)} \tilde{f}(\boldsymbol{r},\boldsymbol{p},Y-y) \\
=&Q_{s0}^2 r^2 \frac{(\ln \frac{k}{Q_{s0}})^{1/4} (\ln \frac{2}{kr})^{1/4} \left(1+\sqrt{\frac{2\bar{\alpha}_s y}{\ln \frac{k}{Q_{s0}}}} \ln \frac{Q_{s0}}{\Lambda}\right)}{2(2\bar{\alpha}_s y)^{3/4} (2\bar{\alpha}_s (Y-y))^{3/4}} e^{2\sqrt{2\bar{\alpha}_s y \ln \frac{k}{Q_{s0}}}} e^{2\sqrt{2\bar{\alpha}_s (Y-y) \ln \frac{2}{kr}}}
\end{aligned} \tag{7.4.13}$$

Substitution of (7.4.12) and (7.4.13) into (7.3.19) gives for the cross section

$$\begin{aligned}
\frac{d\sigma^{q\bar{q}+A}(\boldsymbol{k},y;\boldsymbol{r})}{d^2k dy} =& \frac{\alpha_s C_F}{\pi^3 k^2} \int d^2b\, Q_{s0}^2 r^2 \frac{(\ln \frac{k}{Q_{s0}})^{1/4} (\ln \frac{2}{kr})^{1/4} \left(1+\sqrt{\frac{2\bar{\alpha}_s y}{\ln \frac{k}{Q_{s0}}}} \ln \frac{Q_{s0}}{\Lambda}\right)}{2(2\bar{\alpha}_s y)^{3/4} (2\bar{\alpha}_s (Y-y))^{3/4}} \\
&\times e^{2\sqrt{2\bar{\alpha}_s y \ln \frac{k}{Q_{s0}}}} e^{2\sqrt{2\bar{\alpha}_s (Y-y) \ln \frac{2}{kr}}} \left[1+\frac{(\ln \frac{k}{Q_{s0}})^{1/2} (2\bar{\alpha}_s (Y-y))^{1/2}}{(2\bar{\alpha}_s y)^{1/2} (\ln \frac{2}{kr} \ln \frac{2}{rQ_{s0}})^{1/4}}\right]
\end{aligned} \tag{7.4.14}$$

6. $2/r \gg Q_s \gg k$:

$$g \approx 2\pi \int_{Q_s}^{2/r} dpp \frac{\partial \tilde{N}_G(p,b,y)}{\partial \ln(1/p)} \tilde{f}(\boldsymbol{r},\boldsymbol{p},Y-y) \tag{7.4.15}$$

Repeating the steps leading to (7.4.13) and noting (7.3.15), we finally get

$$\begin{aligned}
\frac{d\sigma^{q\bar{q}+A}(\boldsymbol{k},y;\boldsymbol{r})}{d^2k dy} =& \frac{\alpha_s C_F}{\pi^3 k^2} \int d^2b\, Q_{s0}^2 r^2 \frac{(\ln \frac{2}{rQ_{s0}})^{1/4} \ln \frac{Q_{s0}}{\Lambda}}{2^{5/2} (2\bar{\alpha}_s y)^{3/4} (2\bar{\alpha}_s (Y-y))^{3/4}} \\
&\times e^{4\sqrt{2}\bar{\alpha}_s y} e^{2\sqrt{2\bar{\alpha}_s (Y-y) \ln \frac{2}{Q_{s0} r}}}
\end{aligned} \tag{7.4.16}$$

Eqs. (7.4.4)–(7.4.16) represent the dipole–nucleus inclusive cross section in all kinematic regions.

7.5 Gluon production at the leading order in asymptotic regions

The DIS inclusive cross section is obtained from the dipole–nucleus one using (7.2.1). Integration over the dipole size r and momentum fraction z can be carried out for $Q \gg$

Λ, m. In this case the largest contribution stems from the transversely polarized virtual photon. Setting $m_f = 0$ in (6.2.3) we write (7.2.1) as

$$\frac{d\sigma^{\gamma^* A}(\boldsymbol{k}, y; Q)}{d^2k dy} = \frac{N_c}{\pi^2} \sum_f \frac{\alpha_{\rm em}^f}{\pi} \int d^2r \int_0^1 dz\, Q^2 z(1-z)\, K_1^2\left(rQ\sqrt{z(1-z)}\right) \times \left[z^2 + (1-z)^2\right] \frac{d\sigma^{q\bar{q}+A}(\boldsymbol{k}, y; \boldsymbol{r})}{d^2k dy}\,. \quad (7.5.1)$$

At large Q the dominant contribution to the z-integral arises from $z \to 0, 1$. This corresponds to either quark or antiquark carrying most of the photon's energy. These limits are symmetric, therefore we can calculate the z-integral for $z \to 0$ and multiply the result by 2. Thus,

$$\begin{aligned}\frac{d\sigma^{\gamma^* A}(\boldsymbol{k}, y; Q)}{d^2k dy} &\approx \frac{N_c Q^2}{\pi^2} \frac{2\alpha_{\rm em}}{3} \int_{4/Q^2}^\infty dr^2 \frac{d\sigma^{q\bar{q}+A}(\boldsymbol{k}, y; \boldsymbol{r})}{d^2k dy}\, 2\int_0^\infty dz\, z\, K_1^2\left(rQ\sqrt{z}\right) \\ &= \frac{8N_c}{3\pi^2 Q^2} \frac{2\alpha_{\rm em}}{3} \int_{4/Q^2}^\infty \frac{dr^2}{r^4} \frac{d\sigma^{q\bar{q}+A}(\boldsymbol{k}, y; \boldsymbol{r})}{d^2k dy}\,, \end{aligned} \quad (7.5.2)$$

where we took into account only three light quarks. To set the low limit of integration in (7.5.2) we noted that integrand in (7.5.1) peaks at $rQ \sim 1/\sqrt{z(1-z)} \geq 2$. Upon substitution of (7.3.19) into (7.5.2) we get

$$\frac{d\sigma^{\gamma^* A}(\boldsymbol{k}, y; Q)}{d^2k dy} = \frac{16\alpha_s \alpha_{\rm em}}{9\pi^5} \frac{N_c C_F}{Q^2 k^2} \int d^2b \int_{4/Q^2}^\infty \frac{dr^2}{r^4} \int d^2p\, \frac{\partial \tilde{N}_G(p, b, y)}{\partial \ln(1/p)}\, \tilde{f}(\boldsymbol{r}, \boldsymbol{p} - \boldsymbol{k}, Y - y)\,. \quad (7.5.3)$$

To determine the cross section for gluon production in DIS it is convenient to do integral over r before we integrate over ν in $\tilde{f}$. We thus define an auxiliary function

$$d(Q, p, y) = \int_{\frac{4}{Q^2}}^\infty \frac{dr^2}{r^4} \tilde{f}(\boldsymbol{r}, \boldsymbol{p}, y)\,. \quad (7.5.4)$$

Employing (7.2.5) in (7.5.4) we obtain the Mellin representation of d

$$d(Q, p, y) = \frac{Q}{2\pi p} \int_{-\infty}^\infty d\nu e^{2\alpha_s \chi(\nu) y} \left(\frac{p}{Q}\right)^{2i\nu} \frac{\Gamma(\frac{1}{2} - i\nu)}{(\frac{1}{2} - i\nu)\Gamma(\frac{1}{2} + i\nu)(2i\nu + 1)^2} \quad (7.5.5)$$

Inasmuch as we are interested only in asymptotic behavior of d, which we will derive using the saddle-point approximation, we can write in view of (7.2.5)

$$d(Q, p, y) = \frac{Q^2}{4} \tilde{f}(2/Q, \boldsymbol{p}, y) \frac{1}{\frac{1}{2} - i\nu_{\rm sp}} \quad (7.5.6)$$

where $\nu_{\rm sp}$ is a saddle point given by one of the formulas (7.3.1),(7.3.4),(7.3.6). In particular, using (7.3.2), (7.3.3) and (7.3.5) in (7.5.6) yields

$$d(Q,\boldsymbol{p},y)=\frac{Q}{4p}\frac{1}{\sqrt{14\pi\zeta(3)\bar{\alpha}_s\,y}}\,e^{(\alpha_P^{(0)}-1)y}\,e^{-\frac{\ln^2\frac{p}{Q}}{14\zeta(3)\bar{\alpha}_s\,y}}\,,\qquad \alpha_s y\gg\ln^2\frac{p}{Q} \tag{7.5.7}$$

$$d(Q,\boldsymbol{p},y)=\frac{1}{4\sqrt{\pi}}\frac{(\ln\frac{Q}{Q_{s0}})^{1/2}}{\left(2\bar{\alpha}_s y\right)^{3/4}(\ln\frac{Q}{p})^{1/4}}e^{2\sqrt{2\bar{\alpha}_s y\ln\frac{Q}{p}}}\,,\qquad Q\gg p \tag{7.5.8}$$

$$d(Q,\boldsymbol{q},y)=\frac{Q^2}{8\sqrt{\pi}p^2}\frac{1}{\left(2\bar{\alpha}_s y\ln\frac{p}{Q}\right)^{1/4}}e^{2\sqrt{2\bar{\alpha}_s y\ln\frac{p}{Q}}}\,,\qquad Q\ll p \tag{7.5.9}$$

Inspecting (7.5.3),(7.5.4),(7.5.6),(7.3.19) and (7.4.1) we get

$$\frac{d\sigma^{\gamma^* A}(\boldsymbol{k},y;Q)}{d^2k\,dy}=\frac{4N_c\alpha_{\rm em}\kappa}{9\pi^2}\frac{d\sigma^{q\bar{q}+A}(\boldsymbol{k},y;2/Q)}{d^2k\,dy} \tag{7.5.10}$$

where we denoted by κ the logarithmic (or constant) factor $(1/2-i\nu_{\rm sp})^{-1}$. Explicitly,

$$\kappa=2\left(\frac{\ln\frac{\max\{k,Q\}}{\min\{k,Q\}}}{2\bar{\alpha}_s(Y-y)}\right)^{1/2}\,,\ \text{if}\ \ k,Q\gg Q_s\,;\qquad \kappa=1\,,\ \text{if}\ \ k,Q\ll Q_s\,, \tag{7.5.11}$$

Eq. (7.5.10) together with the expressions of the inclusive dipole–nucleus cross section derived in Sec. 7.5 provide the cross section for the inclusive gluon production in DIS at the leading logarithmic approximation.

7.6 NLO BFKL effects: energy conservation

7.6.1 NLO BK effects

The NLO BFKL kernel [115, 116] does not seems be offer stable results, and it is expected that higher order calculation might cure the problem. But given the extreme complexity of NLO BFKL calculations, it seems to be a formidable task to obtain higher-order results within the forseeablle future. However, it is found that momentum conservation is the dominant contribution in higher orders [117, 118], or better to say, to all orders. Recall that LO BFKL/BK equations are derived in the eikonel approximation. And each step of emission does alter the original trajectory of emitter. This is only

good for very soft emissions in every step, in other words, LO BFKL/BK are valid for infinitely large rapidity intervals between the dipole and the target nucleus. For finite rapidity intervals, higher order effects are no longer negligible. Specifically, [117, 118] proposed a resummation of collinear singlaritites to all orders to correct the problem of NLO BFKL. Let us also recall that DGLAP equations is derived in the limit of large-Q^2 and resums the collinar singularities. The combined effect is to pick up higher order terms of BFKL/BK that satisfy momentum conservation. We will briefly explain why the collinear singlarities correspond to momentum conservation.

Momentum conservations at small-x requires(quark contribution can be safely omitted, see Chap. 2)

$$\int_0^1 dx x G(x,Q^2) = 1 \tag{7.6.1}$$

Also recall that the anomalous dimension is defined in (2.3.6). Combined it with DGLAP equation (2.2.5), one gets

$$\int_0^1 dx \int_x^1 \frac{dz}{z} P_{\mathrm{GG}}(z) x G(\frac{x}{z}, Q^2) \tag{7.6.2}$$

A change of variable $y = x/z$ would decouple the 2-dimensional integral,

$$\int_0^1 dy y G(y,Q^2) \int_0^1 dz z P_{\mathrm{GG}}(z) = 0 \tag{7.6.3}$$

Therefore

$$\gamma(1) = 0 \tag{7.6.4}$$

This constraint is central in constructing a model for NLO BK equation.

7.6.2 Dipole scattering amplitude

As explained above, one of the most important NLO effects is the momentum conservation. BK equation modified to account for the energy conservation reads [140, 141]

$$\frac{\partial N(\boldsymbol{r},\boldsymbol{b},y)}{\partial y} = \frac{\bar{\alpha}_s}{2\pi}\left(1 - \frac{\partial}{\partial y}\right)\int d^2r' \frac{\boldsymbol{r}^2}{\boldsymbol{r}'^2(\boldsymbol{r}-\boldsymbol{r}')^2}\{N(\boldsymbol{r}',\boldsymbol{b},y) + N(\boldsymbol{r}-\boldsymbol{r}',\boldsymbol{b},y) + \\ + N(\boldsymbol{r},\boldsymbol{b},y) - N(\boldsymbol{r}',\boldsymbol{b},y)N(\boldsymbol{r}-\boldsymbol{r}',\boldsymbol{b},y)\}\ . \tag{7.6.5}$$

In this section we discuss solution to this equation in dilute and saturation regimes.

7.6.2.1 Dilute regime

Consider first the dilute regime. It is advantageous to represent N as the double Mellin transform

$$N(\boldsymbol{r},\boldsymbol{b},y)=\int_{-i\infty}^{i\infty}\frac{d\omega}{2\pi i}\int_{-i\infty}^{i\infty}\frac{d\gamma}{2\pi i}\mathcal{N}(\gamma,\boldsymbol{b},\omega)\frac{e^{\omega y+\gamma\xi-\xi}}{\omega-2\bar{\alpha}_s\chi_1(\gamma,\omega)}\,, \tag{7.6.6}$$

where we introduced a new dimensionless variable $\xi=\ln(1/r^2Q_{s0}^2)$. The anomalous dimension γ is related to the Mellin variable ν that we have used so far as $\gamma=1/2-i\nu$, so that the LO BFKL eigenvalue function is $\chi(\nu)=\chi(i(\gamma-1/2))$, see (6.2.12). $\chi_1(\gamma,\omega)$ denotes the NLO BFKL eigenvalue function. In the dilute regime the N^2 term in the r.h.s. of (7.6.5) can be neglected. Substituting (7.6.6) into (7.6.5) one arrives at the following relation between the Mellin variables

$$\omega=2\bar{\alpha}_s\chi_1(\gamma,\omega)=2\bar{\alpha}_s(1-\omega)\chi\left(i(\gamma-1/2)\right)\,, \tag{7.6.7}$$

with the explicit solution for ω

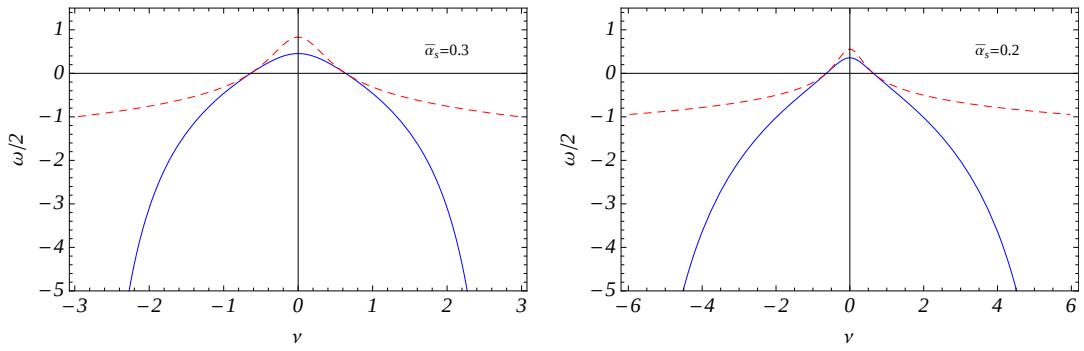

(a) (b)

Figure 7.1 $\omega(\nu)$ for (a) $\bar{\alpha}_s=0.3$ and (b) $\bar{\alpha}_s=0.2$. LO and NLO are represented by dashed (red) and solid (blue) lines respectively. Notice the different ν ranges of the two plots.

$$\omega=\frac{2\bar{\alpha}_s\chi(\nu)}{1+2\bar{\alpha}_s\chi(\nu)}\,. \tag{7.6.8}$$

This solution is plotted in Fig. 7.1. ω diverges at $\nu = \nu^*$ satisfying $2\bar{\alpha}_s\chi(\nu^*) = -1$. As $\bar{\alpha}_s \to 0$, ω approaches the LO expression while $\nu^* \to \pm\infty$. At $\gamma \to 0$, i.e. $i\nu \to 1/2$, $\chi \approx 1/(1-2i\nu) = 1/2\gamma$ and (7.6.8) yields

$$\gamma(\omega) = \bar{\alpha}_s \left(\frac{1}{\omega} - 1 \right) . \tag{7.6.9}$$

This can be used as a model of anomalous dimension that takes into account the energy conservation as suggested in [148, 149].

Integrating (7.6.6) over ω we obtain

$$N(\boldsymbol{r}, \boldsymbol{b}, y) = \int_{-\infty}^{+\infty} d\nu \, C_\nu^A \, e^{\omega(\nu) y + \gamma\xi - \xi} , \tag{7.6.10}$$

with $\omega(\nu)$ given by (7.6.8). Remembering that in the dilute regime (and $N_c \gg 1$) $N_G = 2N$, see (7.3.7), and using the same initial condition as in (7.3.12) we get

$$N_G(\boldsymbol{r}, \boldsymbol{b}, y) = \int_{-\infty}^{\infty} d\nu \, \exp\left\{ \frac{2\bar{\alpha}_s\chi(\nu) y}{1 + 2\bar{\alpha}_s\chi(\nu)} \right\} (rQ_{s0})^{1+2i\nu} \, \frac{1}{8\pi} \, \frac{1 + (1-2i\nu) \ln \frac{Q_{s0}}{\Lambda}}{(1-2i\nu)^2} . \tag{7.6.11}$$

This integral can be taken in the double-logarithmic approximation (DLA), which corresponds to keeping only one of the poles of χ, namely $\chi(\nu) = 1/(1-2i\nu)$. Denote

$$\phi(\xi, y) = \frac{2\bar{\alpha}_s\chi(\nu) y}{1 + 2\bar{\alpha}_s\chi(\nu)} - (1/2 + i\nu)\xi . \tag{7.6.12}$$

Then, in the DLA

$$\phi(\xi, y) \approx \frac{\bar{\alpha}_s}{\gamma + \bar{\alpha}_s} y + \gamma\xi - \xi = 2\sqrt{\bar{\alpha}_s y \xi} - \xi(1 + \bar{\alpha}_s) + \frac{1}{2} (\gamma - \gamma_0)^2 \, \frac{2\xi^{3/2}}{(\bar{\alpha}_s y)^{1/2}} , \tag{7.6.13}$$

where

$$\gamma_0 = \sqrt{\frac{\bar{\alpha}_s y}{\xi}} - \bar{\alpha}_s \tag{7.6.14}$$

is the saddle point. Substituting (7.6.13) into (7.6.11) and integrating over the saddle point gives

$$N_G(\boldsymbol{r}, \boldsymbol{b}, y) = \frac{1 + 2\gamma_0 \ln \frac{Q_{s0}}{\Lambda}}{32\pi^{1/2}\gamma_0^2} \, \frac{(\bar{\alpha}_s y)^{1/4}}{\ln^{3/4} \frac{1}{r^2 Q_s^2}} (r^2 Q_s^2)^{1+\bar{\alpha}_s} e^{2\sqrt{\bar{\alpha}_s y \ln \frac{1}{r^2 Q_s^2}}} . \tag{7.6.15}$$

The most important correction due to momentum conservation requirement is steeper dependence of the scattering amplitude on r.

7.6.2.2 Saturation momentum

To determine the saturation momentum, we need to find a set of lines in the y, ξ plane along which the amplitude is constant. In the DLA approximation this is equivalent to the requirement that the phase (7.6.13) be constant, i.e. $2\sqrt{\bar{\alpha}_s y\xi} - \xi(1+\bar{\alpha}_s) = 0$. Denoting solution to this equation as $\xi_s(y)$ we obtain

$$Q_s^2 = Q_{s0}^2 e^{\xi_s} = Q_{s0}^2\, e^{\frac{4\bar{\alpha}_s y}{(1+\bar{\alpha}_s)^2}}\,. \tag{7.6.16}$$

Energy dependence of the saturation momentum becomes more gradual compared to the LO.

A more accurate evaluation of the saturation momentum requires solving the following two equations [135]:

$$\phi = \frac{2\bar{\alpha}_s\chi(\gamma)y}{1+2\bar{\alpha}_s\chi(\gamma)} + \gamma\xi - \xi \;= 0 \tag{7.6.17a}$$

$$\frac{\partial\phi}{\partial\gamma} = \frac{2\bar{\alpha}_s\chi'(\gamma)y}{1+2\bar{\alpha}_s\chi(\gamma)} - \frac{(2\bar{\alpha}_s)^2\chi(\gamma)\chi'(\gamma)y}{(1+2\bar{\alpha}_s\chi(\gamma))^2} + \xi = 0\,. \tag{7.6.17b}$$

The first one determines the line on y, ξ plane where the amplitude is stationary, while the second one fixes the trajectory of the steepest descend [135]. Eliminating y and ξ from these equations we end up with an equation for the saddle-point $\gamma_{\rm sp}$:

$$\chi'(\gamma_{\rm sp}) + \frac{1}{1-\gamma_{\rm sp}}\chi(\gamma_{\rm sp}) = \frac{2\bar{\alpha}_s\chi(\gamma_{\rm sp})\chi'(\gamma_{\rm sp})}{1+2\bar{\alpha}_s\chi(\gamma_{\rm sp})}\,. \tag{7.6.18}$$

Employing (6.2.12) we write

$$\chi(\gamma) = \psi(1) - \frac{1}{2}\psi(\gamma) - \frac{1}{2}\psi(1-\gamma)\,, \tag{7.6.19}$$

$$\chi'(\gamma) = -\frac{1}{2}\psi'(\gamma) + \frac{1}{2}\psi'(1-\gamma)\,. \tag{7.6.20}$$

Saddle point in the LO is obtained as the solution to (7.6.18) in the $\bar{\alpha}_s \to 0$ limit. Hence, dropping the r.h.s. of (7.6.18) we obtain $\gamma_{\rm sp} = 0.37$. In the NLO approximation $\gamma_{\rm sp}$ depends on $\bar{\alpha}_s$ as shown in Fig. 7.2(a). As $\bar{\alpha}_s$ increases $\gamma_{\rm sp}$ decreases and becomes

closer to the experimental data. For a given $\bar{\alpha}_s$ (7.6.17) implies that

$$Q_s^2 = Q_{s0}^2 \exp\left\{\frac{1}{1-\gamma_{\rm sp}}\frac{2\bar{\alpha}_s\chi(\gamma_{\rm sp})y}{1+2\bar{\alpha}_s\chi(\gamma_{\rm sp})}\right\} \equiv Q_{s0}^2 e^{2\bar{\alpha}_s y\, h(\bar{\alpha}_s)}\,, \tag{7.6.21}$$

Particularly, at the LO $h(\bar{\alpha}_s) = \frac{\chi(\gamma_{\rm sp})}{1-\gamma_{\rm sp}} = 2.44$ independently of $\bar{\alpha}_s$. In Fig. 7.2(b) we show the NLO behavior of h as given by (7.6.21) and its DLA given by (7.6.16). Again we observe that the NLO correction makes the energy dependence of the saturation scale more gradual. This is understandable because the momentum conservation reduces the phase space available for gluon emission.

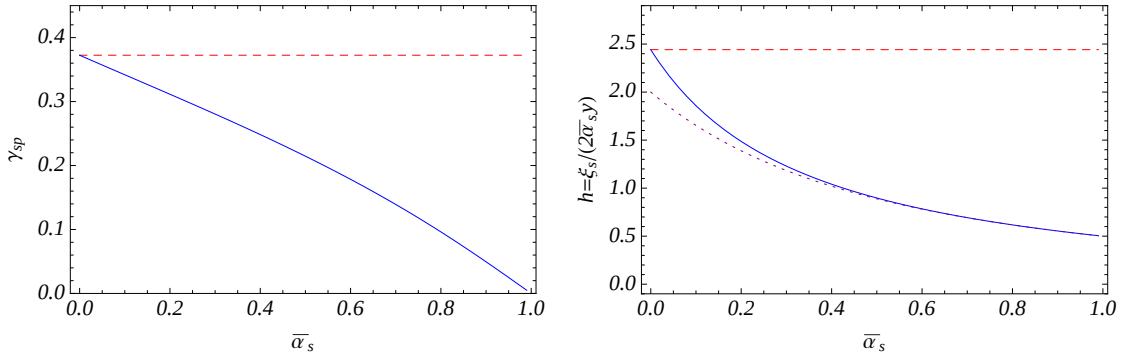

(a) (b)

Figure 7.2 (a) Solution for the saddle point equation (7.6.18) $\gamma_{\rm sp}(\bar{\alpha}_s)$: solid blue line is NLO (momentum conservation), dashed red line is LO. (b) Function $h(\bar{\alpha}_s)$ defined in (7.6.21): solid blue line is NLO, dotted (purple) is its DLA (7.6.16) and dashed (red) is LO.

7.6.2.3 Saturation regime

In the saturation region, (7.6.5) reads

$$\frac{\partial N(\boldsymbol{r},\boldsymbol{b},y)}{\partial y} = \bar{\alpha}_s\left(1-\frac{\partial}{\partial y}\right)\int_{2/Q_s^2}^{r^2}\frac{dr'^2}{r'^2}\left\{N(\boldsymbol{r}',\boldsymbol{b},y) - N(\boldsymbol{r}',\boldsymbol{b},y)N(\boldsymbol{r},\boldsymbol{b},y)\right\} \tag{7.6.22}$$

We expect that the scattering amplitude will approach its unitarity limit as $y \to \infty$. Therefore, we are looking for a solution to (7.6.22) in the form

$$N = 1 - S \tag{7.6.23}$$

where $S \ll 1$ is an element of the scattering-matrix of dipole $\boldsymbol{r}$. Now

$$-\frac{\partial S(r,y)}{\partial y} = \bar{\alpha}_s \left(1 - \frac{\partial}{\partial y}\right) \left\{\ln(r^2 Q_s^2) S(r,y)\right\} . \tag{7.6.24}$$

We are interested in the scaling solution viz. we are looking for a solution in the form $S(r,y) = S(\tau(r,y))$ where

$$\tau = \ln(r^2 Q_s^2) = \ln(r^2 Q_{s0}^2) + \frac{4\bar{\alpha}_s y}{(1+\bar{\alpha}_s)^2} , \tag{7.6.25}$$

and we used (7.6.16). Introducing a new parameter that determines rapidity dependence of the saturation scale (in the DLA)

$$\lambda = \frac{4\bar{\alpha}_s}{(1+\bar{\alpha}_s)^2} \tag{7.6.26}$$

we write (7.6.24) as

$$\frac{\partial S}{\partial \tau}(\bar{\alpha}_s \lambda \tau - \lambda) = \bar{\alpha}_s (\tau - \lambda) S . \tag{7.6.27}$$

It is easily integrated with the solution

$$S(\tau) = S_0 e^{\frac{\tau}{\lambda}} (1 - \bar{\alpha}_s \tau)^{\frac{1}{\bar{\alpha}_s \lambda} - 1} , \tag{7.6.28}$$

where S_0 is an integration constant that is determined by matching with the solution in the dilute regime. This is similar to the solution derived in [140]. Note, that (7.6.28) is applicable only at $1 < \tau \leq 1/\bar{\alpha}_s$. Solution (7.6.28) is exhibited in Fig. 7.3.

7.6.3 Dipole density

We proceed with the analysis of the NLO effects related to the energy conservation in the dipole density. Using the result of the Sec. 7.6.2 we obtain in place of (7.2.5):

$$\tilde{f}(\boldsymbol{r}, \boldsymbol{q}, y) = \frac{r}{\pi q} \int_{-\nu^*}^{\nu^*} d\nu \, \exp\left\{\frac{2\bar{\alpha}_s \chi(\nu) y}{1 + 2\bar{\alpha}_s \chi(\nu)}\right\} \left(\frac{rq}{2}\right)^{2i\nu} \frac{\Gamma\left(\frac{1}{2} - i\nu\right)}{\Gamma\left(\frac{1}{2} + i\nu\right)(2i\nu + 1)^2} , \tag{7.6.29}$$

where ν^* satisfy $1 + 2\bar{\alpha}_s \chi(\nu^*) = 0$. Similarly to our discussion in Sec. 7.3.1, we would like to find asymptotic expressions for $\tilde{f}$ in various kinematic regions. Since the integrand in (7.6.29) is a steeply falling function of ν we can replace the limits of integration by $\nu^* = \pm\infty$.

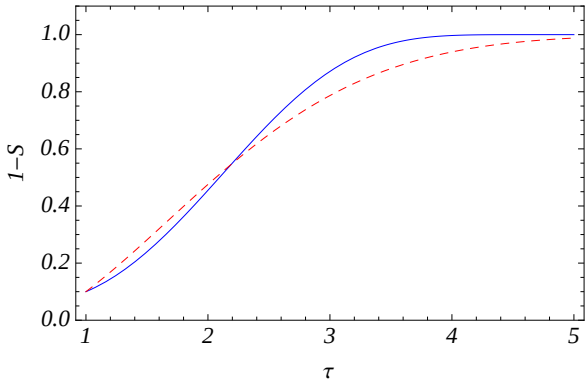

Figure 7.3 Solution to the LO (dashed red line) and the modified (solid blue) BK equations deeply in the saturation region $1 < \tau < 1/\bar{\alpha}_s$. The initial condition is $S = 0.9$ at $\tau = 1$.

1. $\alpha_s y \gg \ln^2 \frac{rq}{2}$. Expression in the exponent of (7.6.29) can be approximated as

$$\frac{2\bar{\alpha}_s\chi(\nu)y}{1+2\bar{\alpha}_s\chi(\nu)} \approx \frac{(\alpha_P^{(0)}-1)y}{\alpha_P^{(0)}} - \frac{14\zeta(3)\bar{\alpha}_s y}{[\alpha_P^{(0)}]^2}\nu^2 \,. \tag{7.6.30}$$

We see that the pomeron intercept became $\alpha_P^{(1)} = 2 - 1/\alpha_P^{(0)}$, while the "diffusion constant" has increased by $1/[\alpha_P^{(0)}]^2$, i.e. growth of $\tilde{f}$ with rapidity has slowed down, while diffusion has speeded up. The later observation has profound implications on diffractive gluon production (see [88, 99, 100] for in-depth discussion). For $\bar{\alpha}_s = 0.4$ the intercept is $\alpha_P^{(1)} = 1.5$ (compare with $\alpha_P^{(0)} = 2.1$), which is in better agreement with the data. Eq. (7.3.2) is modified as follows

$$\tilde{f}(\boldsymbol{r},\boldsymbol{q},y) = \frac{r}{q}\frac{\alpha_P^{(0)}}{\sqrt{14\pi\zeta(3)\bar{\alpha}_s\, y}}\, e^{(\alpha_P^{(1)}-1)y}\, e^{-\frac{[\alpha_P^{(0)}]^2 \ln^2\frac{rq}{2}}{14\zeta(3)\bar{\alpha}_s\,(Y-y)}} \,. \tag{7.6.31}$$

2. $rq < 2$ and $\ln\frac{2}{rq} \gg \alpha_s y$. Expanding $\chi \approx 1/(1-2i\nu)$ we find the saddle point at

$$2i\nu_1 = 1 + 2\bar{\alpha}_s - \sqrt{\frac{2\bar{\alpha}_s y}{\ln\frac{2}{rq}}} \,. \tag{7.6.32}$$

Integration over the saddle-point and assuming $\ln\frac{2}{rq} \ll y/\alpha_s$ yields

$$\tilde{f}(\boldsymbol{r},\boldsymbol{q},y) = \frac{r^2}{8\sqrt{\pi}}\frac{(rq/2)^{2\bar{\alpha}_s}}{\left(2\bar{\alpha}_s y\ln\frac{2}{rq}\right)^{1/4}\left[1-\sqrt{2\bar{\alpha}_s\frac{1}{y}\ln\frac{2}{rq}}\right]} e^{2\sqrt{2\bar{\alpha}_s y\ln\frac{2}{rq}}} \,. \tag{7.6.33}$$

3. $rq > 2$ and $\alpha_s y \ll \ln\frac{rq}{2} \ll y/\alpha_s$. Now, another pole in χ dominates $\chi \approx 1/(1+2i\nu)$ with the result

$$\tilde{f}(\boldsymbol{r},\boldsymbol{q},y) = \frac{1}{2q^2\sqrt{\pi}} \frac{(2/rq)^{2\bar{\alpha}_s}}{\left(2\bar{\alpha}_s y \ln\frac{rq}{2}\right)^{1/4}\left[1-\sqrt{2\bar{\alpha}_s\frac{1}{y}\ln\frac{rq}{2}}\right]} e^{2\sqrt{2\bar{\alpha}_s y \ln\frac{rq}{2}}} . \tag{7.6.34}$$

Note, that in both cases (7.6.33) and (7.6.34) the momentum dependence of the leading twist is modified by an additional power $2\bar{\alpha}_s$. This can have important consequences at high Q^2 and/or $\boldsymbol{k}$. We are discussing this in more detail in Sec. 7.8.

7.7 Nuclear modification factor

The nuclear modification factor is defined as

$$R_{\gamma^* A} = \frac{\int d^2b \, \frac{d\sigma_{\gamma^* A}}{d^2k\, dy\, d^2b}}{A \int d^2b \, \frac{d\sigma_{\gamma^* p}}{d^2k\, dy\, d^2b}} . \tag{7.7.1}$$

In the logarithmic approximation (7.5.10) implies that the cross section for inclusive gluon production in DIS on a heavy nucleus is simply proportional to the cross section for inclusive gluon production by dipole of size $r = 2/Q$. Consequently, the nuclear modification factor (7.7.1) can be approximated by

$$R_{\gamma^* A} \approx R_{q\bar{q}+A}\big|_{r=2/Q} . \tag{7.7.2}$$

In the same approximation, pA scattering can also be approximated as the $q\bar{q}+A$ one provided that we are interested in inclusive processes not too close in rapidity to the proton or nucleus fragmentation region [100]. Atomic weight A and rapidity y dependence of incluisve cross section in pA collisions at the leading logarithmic order was discussed in great detail in [108] and we refer the interested reader to that paper. Here we will focus on *the logarithmic derivative of the nuclear modification factor* defined as

$$J = \frac{1}{R_{\gamma^* A}} \frac{\partial R_{\gamma^* A}}{\partial y} . \tag{7.7.3}$$

Outside the saturation region this observable is proportional to the difference between the anomalous dimension of the gluon distribution in the nucleus γ^A and the one in the proton γ^p. If the coherence effects were negligible, the two anomalous dimensions would have been identical. This is not the case according to the theory of gluon saturation. As the result, the NMF is suppressed even at $\boldsymbol{k} > Q_s$. Thus J is especially sensitive probe of the mechanism that leads to the suppression of the NMF for hadron production at small x.

Let us relate J to the difference of anomalous dimensions $\gamma^A - \gamma^p$. It follows from (7.7.1) that

$$J = \frac{\partial}{\partial y} \ln R_{\gamma^* A} = \frac{\partial}{\partial y} \ln \frac{d\sigma^{\gamma^* A}}{d^2k\, dy} - \frac{\partial}{\partial y} \ln \frac{d\sigma^{\gamma^* p}}{d^2k\, dy} \,. \tag{7.7.4}$$

Using (7.7.2) and (7.3.19),(7.4.1) and assuming that the b-dependence factors out we derive

$$\frac{\partial}{\partial y} \ln R_{\gamma^* A} \approx \frac{\partial}{\partial y} \ln g^A\big|_{\boldsymbol{b}=0} - \frac{\partial}{\partial y} \ln g^p\big|_{\boldsymbol{b}=0} \,, \tag{7.7.5}$$

where g is the inclusive $q\bar{q} + A$ cross section modulo a constant factor, see Sec. 7.4. We assigned superscripts A and p to g to indicate the two cases: $A > 1$ and $A = 1$ respectively. In the following we will omit the specification that g is taken at zero impact parameter. Outside the saturation region we can employ the Mellin representation for N_G (7.3.12) and $\tilde{f}$ (7.2.5), substitute them into (7.4.1), take the LLA limit and obtain up to a pre-exponential factor

$$g^A \propto Q_0 r \, \exp\left[2\bar{\alpha}_s \chi(\nu_0)(Y - y) + 2i\nu_0 \ln \frac{rp}{2} + 2\bar{\alpha}_s \chi(\mu_0^A) y + 2i\mu_0^A \ln \frac{Q_{s0}}{p}\right] \tag{7.7.6}$$

and analogously for g^p. Here ν_0, μ_0^A are the saddle points in the Mellin transform of $\tilde{f}$ and $\tilde{N}_G$ respectively. The omitted pre-factor in (7.7.6) depends on momenta only logarithmically. Momentum p stands for either Q or k depending on the kinematic region of interest. It is straightforward to verify that g^A and g^p obey the equations

$$\frac{\partial g^A}{\partial y} = 2\bar{\alpha}_s[\chi(\mu_0^A) - \chi(\nu_0)] g^A \,, \qquad \frac{\partial g^p}{\partial y} = 2\bar{\alpha}_s[\chi(\mu_0^p) - \chi(\nu_0)] g^p \,. \tag{7.7.7}$$

This is just the Mellin transform of the BFKL equation. Plugging (7.7.7) into (7.7.5) we derive

$$J = 2\bar{\alpha}_s \left[\chi(\mu_0^A) - \chi(\mu_0^p)\right] \approx 2\bar{\alpha}_s \chi'(\gamma_0^p) \left(\gamma_0^A - \gamma_0^p\right) . \tag{7.7.8}$$

$\chi'(\gamma)$ is given by (7.6.20) and the saddle point γ_0^p satisfies (7.6.18).

Consider a few examples. Denote $p = \max\{\boldsymbol{k}, Q\}$. In the region $\ln \frac{p}{Q_{s0}} \gg \bar{\alpha}_s y$ we have (see e.g. (7.3.4) and (7.3.13))

$$\chi \approx \frac{1}{1 - 2i\mu} = \frac{1}{2\gamma} \tag{7.7.9}$$

with the saddle point

$$\gamma^A = \frac{1}{2}(1 - 2i\mu_0^A) = \frac{1}{2}\sqrt{\frac{2\bar{\alpha}_s y}{\ln \frac{p}{\Lambda} + \ln \frac{\Lambda}{Q_{s0}}}} \approx \frac{1}{2}\sqrt{\frac{2\bar{\alpha}_s y}{\ln \frac{p}{\Lambda}}} \left(1 + \frac{\ln \frac{Q_{s0}}{\Lambda}}{2 \ln \frac{p}{\Lambda}}\right) \tag{7.7.10}$$

γ^p is obtained by setting $Q_{s0} = \Lambda$. We see that in this kinematic region $\gamma^p < \gamma^A$. By dint of (7.7.9) $\chi'(\gamma) < 0$ implying that $J < 0$. More precisely,

$$J = -\bar{\alpha}_s \frac{\ln \frac{Q_{s0}}{\Lambda}}{\sqrt{2\bar{\alpha}_s y \ln \frac{p}{\Lambda}}} . \tag{7.7.11}$$

In the saturation region $\ln \frac{p}{Q_{s0}} \ll \bar{\alpha}_s y$, γ^A effectively tends to zero as the dipole scattering amplitude saturates at unity. Therefore, in that region $\gamma^A < \gamma^p$, while $\chi \approx \frac{1}{2(1-\gamma)}$. Hence $\chi'(\gamma) > 0$ implying that again $J < 0$. Finally, in the diffusion region $\chi \approx 2\ln 2 - 7\zeta(3)\nu^2$ and we similarly obtain

$$J = -\frac{\ln \frac{p}{\Lambda} \ln \frac{Q_{s0}}{\Lambda}}{7\zeta(3)\bar{\alpha}_s y^2} . \tag{7.7.12}$$

Negativity of J in all kinematic regions signifies the decrease of the inclusive cross section as a function of rapidity. The rate of the decrease depends on the absolute value of J.

7.8 Numerical analysis

The numerical calculation of the inclusive hadron production is performed using Eqs. (7.2.1), (6.2.3),(7.2.7),(7.2.6). We employed the bGCG model [143] for the forward

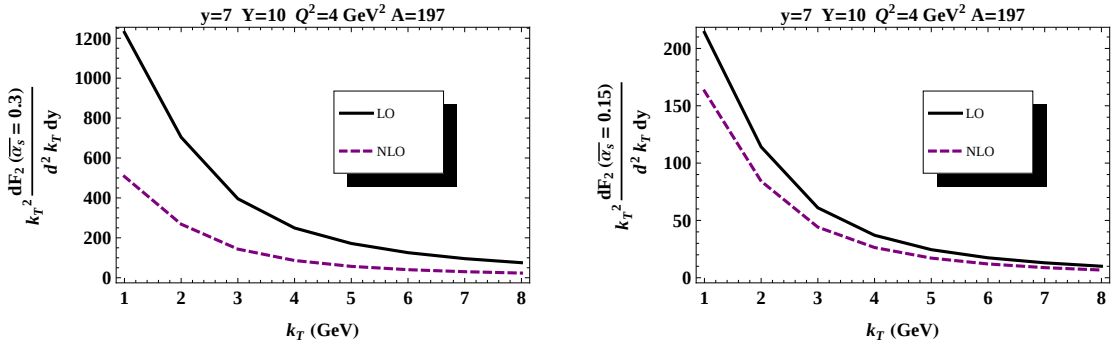

(a) (b)

Figure 7.4 Comparison between the LO and NLO calculations of $k^2 \frac{dF_2(x,Q^2;y)}{d^2kdy}$ as a function of $\boldsymbol{k}$ at two values of coupling (a) $\bar{\alpha}_s = 0.3$ and (b) $\bar{\alpha}_s = 0.15$.

dipole–nucleus scattering amplitude. The bCGC model is reviewed in Appendix. Function $\tilde{f}$ is calculated using formula (7.6.29). The gluon spectrum is then convoluted with the LO pion fragmentation function $\mathcal{F}_G$ as follows

$$\frac{d\sigma_\pi}{d^2k\,dy} = \int_{z_{\min}}^1 \frac{dz}{z^2} \frac{d\sigma_G}{d^2k\,dy}(k/z)\,\mathcal{F}_G(z,k)\,. \tag{7.8.1}$$

The fragmentation function is given in [152]. The total rapidity interval is taken to be $Y = 10$, which is equivalent to $x = e^{-Y} = 4.5 \cdot 10^{-5}$. The range of photon virtualities that we consider is $Q^2 = 2 - 37$ GeV^2. This kinematic region can be probed at the proposed Large Hadron electron Collider and its low Q^2 part at the Electron Ion Collider [153]. The rapidity interval y from the nucleus to the produced gluon is related to $x_{\mathbb{P}}$, a variable used in differctive DIS, as $x_{\mathbb{P}} = e^{-y}$. We consider y in a narrow interval $5 \le y \le 7$ allowed by our formalism. At larger x and/or $x_{\mathbb{P}}$ the validity of the leading logarithmic approximation that we employ becomes uncertain.

The results of our calculations are shown in Figs.(7.4)–(7.8). The NLO calculation shown in the figures refers to the part of the NLO terms that are responsible for momentum conservation. In Fig. 7.4,7.5 we plot the inclusive cross section normalized in the same way as the structure function

$$\frac{dF_2(x,Q^2;y)}{d^2kdy} = \frac{1}{\alpha_{em}} \frac{Q^2}{4\pi^2} \frac{d\sigma^{\gamma^* A}(x,Q^2;y)}{d^2kdy}\,. \tag{7.8.2}$$

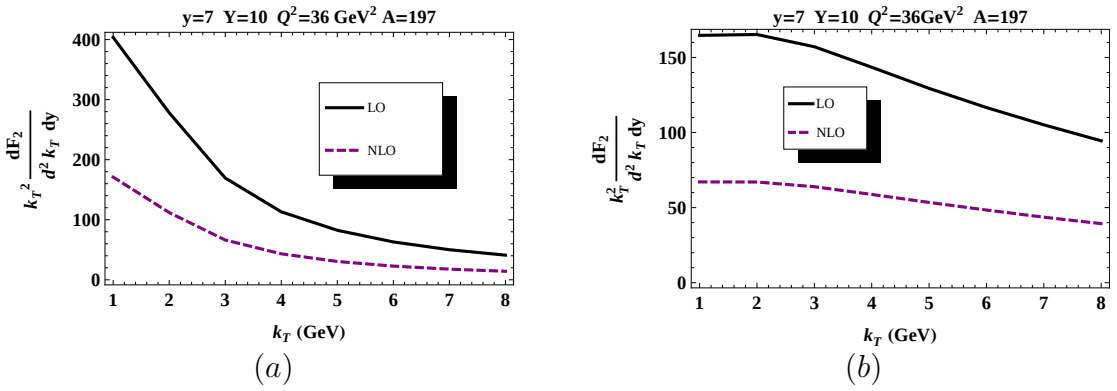

Figure 7.5 Inclusive spectrum $k^2 \frac{dF_2(x,Q^2;y)}{d^2 k dy}$ of (a) pions, (b) gluons as a function of $\boldsymbol{k}$.

We observe that inclusive gluon production at NLO is suppressed compared with the LO case. This is because the anomalous dimension of dipole density at NLO is smaller compared with that of LO, as can be seen in Fig. 7.2. This is expected since energy conservation constrains the phase space available for hadron production. In Fig. 7.4 we demonstrate that the difference between the LO and NLO calculation is smaller at smaller values of coupling.

We see in Fig. 7.5(b) that at small $\boldsymbol{k}$, the gluon production cross section follows $1/\boldsymbol{k}^2$ behavior. Indeed, $1/\boldsymbol{k}^2$ comes from the Lipatov vertex, whereas the gluon distribution in the nucleus is saturated and hence depends on momentum $\boldsymbol{k}$ only logarithmically. This is seen in (7.2.7) where at small $\boldsymbol{k}$ the integral tends to a constant leaving the $1/\boldsymbol{k}^2$ pre-factor in front. Modification of the gluon spectrum due to fragmentation can be inferred by comparing Fig. 7.5(a) and (b).

The cross section grows with Q^2 and $x_{\mathbb{P}}$ logarithmically; both dependences are much steeper at the LO than in the NLO. We also note that momentum conservation correction substantially reduces the cross section. However, the functional form of the $\boldsymbol{k}$-spectrum does not change in the kinematic region that we studied, as we checked explicitly. We attribute this to that fact that the dominant contribution to the Mellin transform stems from anomalous dimension $\gamma \approx 1/2$ in both cases. We expect that at much larger Q and $\boldsymbol{k}$ the NLO $\boldsymbol{k}$-spectrum becomes steeper than those in LO due to additional factors

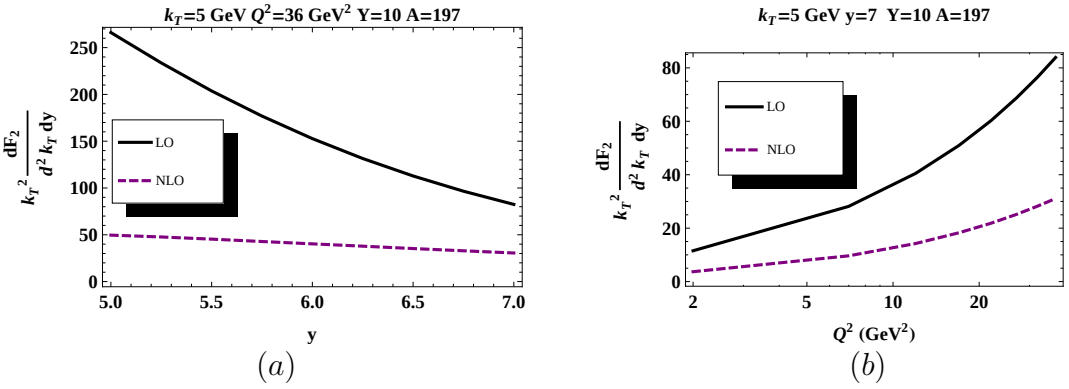

Figure 7.6 Inclusive hadron spectrum $k^2 \frac{dF_2(x,Q^2;y)}{d^2k dy}$ as a function of (a) y, (b) Q^2.

$1/Q^{2\bar{\alpha}_s}$ or $1/\boldsymbol{k}^{2\bar{\alpha}_s}$. However, assumptions of our model restrict our calculation only to the semi-hard values of transverse momenta.

The largest uncertainty in our numerical calculation of hadron spectrum comes from the oversimplified treatment of nuclei geometry. Instead of integrating with a realistic nuclear thickness $T(b)$ we approximated the nuclear density by the step-function. Based on our previous experience with this type of numerical calculations we expect that a more accurate treatment of the nuclear density will only affect the overall normalization of the cross section. From this perspective the ratios of the inclusive spectra should not be much affected by this uncertainty.

Our calculation of the Nuclear Modification Factor (NMF) as a function of $\boldsymbol{k}$ for Au ($A = 197$) and Ca ($A = 40$) is displayed in Fig. 7.7. The general feature of NMF is suppression at low $\boldsymbol{k}$ and enhancement at larger $\boldsymbol{k}$ (the later is often referred to as the Cronin effect [48]). This is in contrast with the hadron production in pA scattering where the Cronin effect gives way to the suppression at all $\boldsymbol{k}$'s provided that the hadron rapidity y is large enough. The reason for this difference is that whereas pA scattering can be approximated by dipole–nucleus scattering [100], $\gamma^* A$ interaction is a superposition of many dipole–nucleus scatterings with different dipole sizes r, see (7.2.2). At small $\boldsymbol{k}$ NMF for dipoles of all sizes is suppressed [108] and therefore we observe suppression of the resulting R for DIS. On the other hand, the fact that $R > 1$ at large $\boldsymbol{k}$ implies

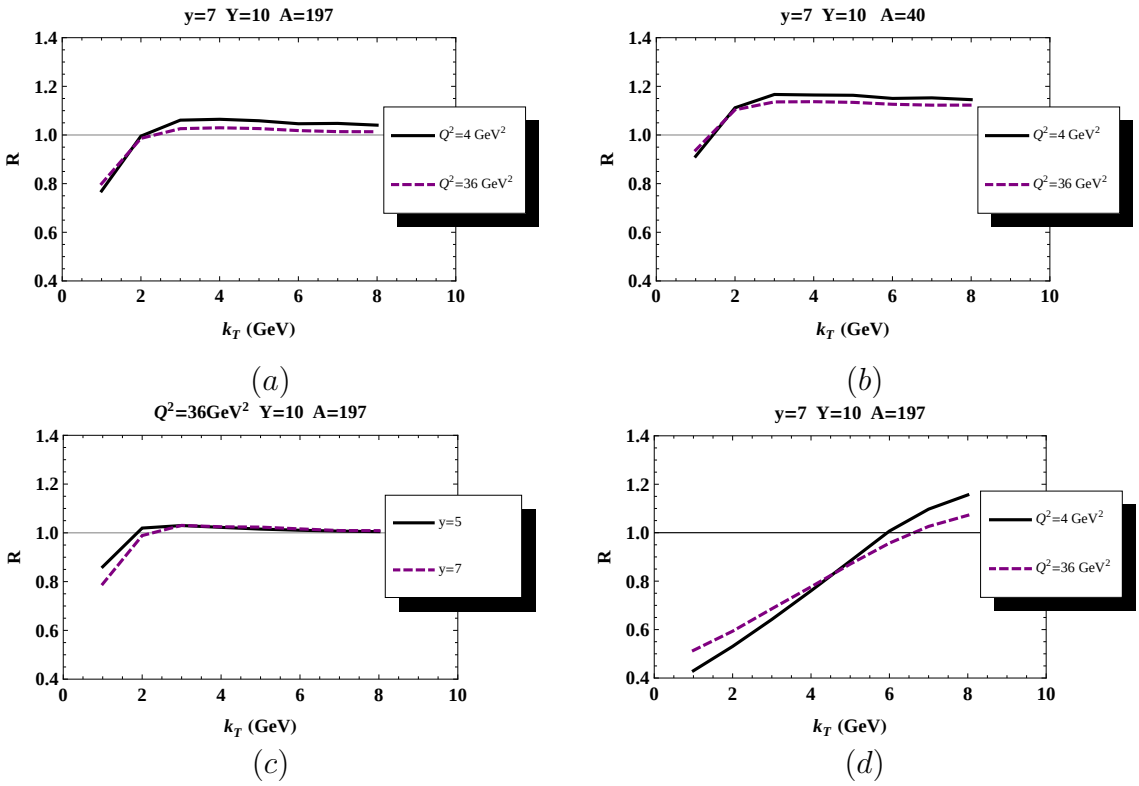

Figure 7.7 Nuclear Modification Factor as a function of $\boldsymbol{k}$ for (a)-(c) hadrons at various A, y and Q^2; (d) gluons. All calculations include the NLO effects.

that the inclusive cross section in that region is dominated by dipoles whose individual scattering on the nucleus exhibits Cronin enhancement, i.e. they are not much effected by the small-x evolution. Presence of such dipoles is ensured by evolution of the dipole density n, which happens if $Y - y \gg 1$. Comparing Figs.7.7 (a)-(c) with (d) we note that due to fragmentation, NMF of hadrons is much slower function of Q^2, y and $\boldsymbol{k}$ than NMF of gluons. Additonally, fragmentation shifts the value of the transverse momentum at which NMF crosses unity towards lower $\boldsymbol{k}$.

Another feature seen in Fig. 7.7 (especially (d)) is that suppression of NMF at low $\boldsymbol{k}$ and its enhancement at high $\boldsymbol{k}$ increases with the photon virtuality Q^2. To understand the Q^2 dependence of the NMF we note that a typical term in its twist expansion looks like

$$R \sim \left(\frac{1}{Q^2}\right)^{n(\gamma_A - \gamma_p)}, \tag{7.8.3}$$

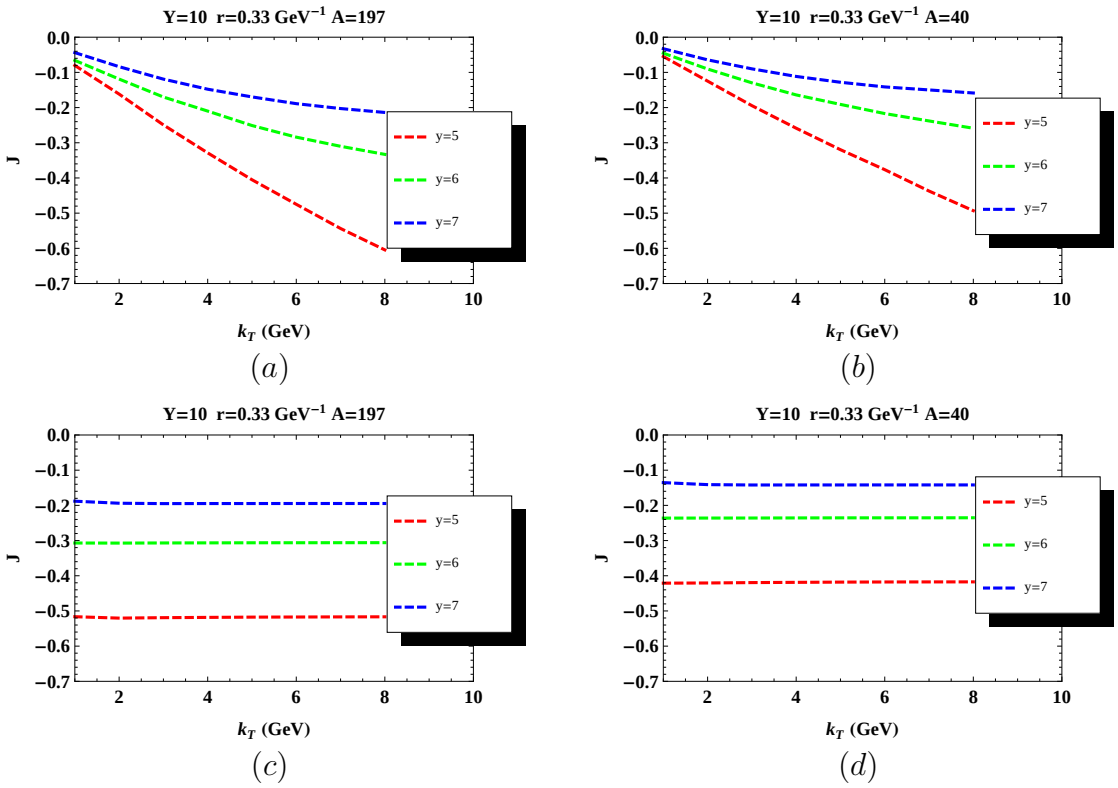

Figure 7.8 Logarithmic derivative of NMF for dipole–nucleus scattering as a function for $\boldsymbol{k}$ for (a),(b) gluons, (c),(d) hadrons. dipole size r, total rapidity Y and nuclear wight A are indicated on each plot. All calculations include the NLO effects.

where $n \geq 1$ is an integer number. It implies that

$$\frac{\partial R}{\partial \ln Q^2} \approx -n(\gamma_A - \gamma_p)R. \tag{7.8.4}$$

At large $\boldsymbol{k}$ $\gamma^A > \gamma^p$ thus $\frac{\partial R}{\partial \ln Q^2} < 0$, whereas at small $\boldsymbol{k}$ $\gamma^A < \gamma^p$ thus $\frac{\partial R}{\partial \ln Q^2} > 0$. This is indeed what we observe in Fig. 7.7. Dependence of NMF on y can be explained similarly.

Fig. 7.8 displays the logarithmic derivative of the NMF J defined in (7.7.3). As we argued in Sec. 7.7 this quantity is proportional to the difference between the anomalous dimensions of the gluon distribution function in nucleus and proton, see(7.7.8). Our analysis in (7.7.11),(7.7.12) indicates that J is negative and decreases as the hadron rapidity y increases, which is indeed seen in Fig. 7.8. Similar trend has been noticed in pA collisions in [150]. We can also see the effect of fragmentation on J by comparing Fig. 7.8(a),(b) with (c),(d). It is interesting that fragmentation completely erases the

$\boldsymbol{k}$ dependence, while leaving the y dependence qualitatively similar. We think that experimental investigation of J is of great interest as it emphasizes the difference between the (linear) gluon evolution in a heavy nucleus and in proton.

CHAPTER 8. Discussions

Chap. 6 studied coherent and incoherent diffractive gluon production in DIS off heavy nuclei in the proposed kinematic region of Electron Ion Collider. Our approach is based on the dipole model introduced in [112]. It allows representing cross sections for high energy hadronic scattering as a convolution of hadronic light-cone wave-functions with the multipole scattering amplitudes. In our case, virtual photon wave function is determined by the perturbative QED and is given by (6.2.3). dipole–nucleus interaction can in turn be represented as a product of dipole density (6.2.13) in transverse coordinate space, satisfying the BFKL equation [113, 114], and the imaginary part of dipole–nucleus forward elastic scattering amplitude as displayed in (6.2.6),(6.2.8), satisfying QCD evolution equations in the small-x region [78, 76]. These formulae are derived in the leading logarithmic approximation $\alpha_s \ln(1/x) \sim 1$, $\alpha_s \ln(1/\beta) \sim 1$, which defines the kinematic region where the results of our calculations are applicable. Note, that hard perturbative factorization is generally broken at small-x, because scattering in this region is characterized by small longitudinal momentum transfer (see e.g. [155]). At moderate x and large Q^2, our formulas reduce to the leading order hard perturbative QCD expressions that can be cast in the factorized form using the diffractive parton distributions [156, 157, 158, 159].

The main results of our calculations are displayed in Fig. 6.2 and Fig. 6.3. We found that nuclear modification factor strongly varies with nuclear weight, and the functional dependence on A is qualitatively different for coherent and incoherent processes. Similarly to diffractive hadron production in pA collisions [101], nuclear effects in coherent

diffractive DIS is strongly dependent on rapidity of produced hadron, whereas they are almost absent in the case of incoherent diffraction. We also made a peculiar observation that the nuclear modification factor for both diffractive channels is essentially independent of the photon virtuality in the region $1 < Q^2 < 25$ GeV^2. Finally, our study of non-forward diffractive hadron production indicates feasibility of experimentally separation of coherent and incoherent diffractive contributions at EIC.

Chap. 7 is dedicated to the dicussion of the inclusive hadron production in DIS scattering at small x. Still, our approach employed the dipole model [112]. We presented the analytical formulae for the cross section in various kinematic regions and discussed the role of the momentum conservation, which is perhaps the most important NLO correction. Modified BK equation proposed in [140, 141] enables us to derive the corresponding correction to the pomeron intercept and found that it is numerically closer to the phenomenological value than the LO result. We also computed the high energy asymptotics of the forward elastic dipole–nucleus scattering amplitude.

Motivated by possible small-x DIS experiments with heavy nuclei [153] we performed numerical calculations of the DIS inclusive cross section using the bCGC model [143]. The results are shown in Figs. 7.4–7.8. We noticed that the NLO effects generally tend to reduce the cross section and make it weaker function of its arguments as compared to the LO result. The nuclear modification factor exhibits suppression at low $\boldsymbol{k}$ and enhancement at higher $\boldsymbol{k}$ even at the largest hadron rapidities that we can address in our approach. To understand dependence of the NMF on rapidity better we introduced the logarithmic derivative of NMF J and showed that it is proportional to the difference between the anomalous dimension of the gluon distribution function in nucleus and proton. Since this difference is non-vanishing only due to coherence effects, J provides a direct measure of the effect of coherence on inclusive cross section. Figs. 7.7,7.8 show dependence of NMF and J on the photon virtuality Q^2, x and hadron rapidity y. We believe that our results may be helpful for experimental investigation of DIS at small-x.

Appendix: bCGC model

We performed the numerical calculations using the bCGC model of the forward dipole scattering amplitude [143]. We treat the nuclei and proton profiles as step-functions; the saturation scales are assumed to scale with A as $Q_s^2 \propto A^{1/3}$. The advantage of this model – besides its compliance with the known analytical approximations to the BK equation [151] – is that its parameters are fitted to the low x DIS data. The explicit form of the scattering amplitude N is given by

$$N(\boldsymbol{r}, 0, y) = \begin{cases} \mathcal{N}_0 \left(\frac{r^2 Q_{qs}^2}{4}\right)^{\gamma}, & rQ_{qs} \leq 2; \\ 1 - \exp[-a \ln^2(brQ_{qs})], & rQ_{qs} \geq 2, \end{cases} \tag{8.0.1}$$

where Q_{qs}^2 is the the *quark* saturation scale related to the *gluon* saturation scale Q_s^2 – which we have called simply the 'saturation scale' throughout the chapters – by $Q_{qs}^2 = (4/9)Q_s^2$. Its functional form is

$$Q_{qs}^2 = A^{1/3} x_0^{\lambda} \, e^{\lambda y} \, s^{\lambda/2} \, \mathrm{GeV}^2 \,, \tag{8.0.2}$$

where s is the square of the center-of-mass energy and y is rapidity with respect to the central rapidity. The anomalous dimension is

$$\gamma = \gamma_s + \frac{1}{c\,\lambda\,(\ln\sqrt{s} + y)} \ln\left(\frac{2}{rQ_{qs}}\right) . \tag{8.0.3}$$

The gluon dipole scattering amplitude can be calculated using (7.3.7). Parameters $\gamma_s = 0.628$ and $c = 9.9$ follow from the BFKL dynamics [151], while $\mathcal{N}_0 = 0.7$ and $\lambda = 0.28$ are fitted to the DIS data. Constants a and b are uniquely fixed from by the requirement of continuity of the amplitude and its first derivative.

Bibliography

[1] C. N. Yang and R. L. Mills, Phys. Rev. **96** 191 (1954).

[2] D. J. Gross, F. Wilczek, Phys. Rev. Lett. **30** 1343 (1973); Phys. Rev. D **8** 3633 (1973).

[3] H. D. Politzer, Phys. Rev. Lett. **30** 1346 (1973).

[4] Michael E. Peskin, Daniel V. Schroeder, *An Introduction To Quantum Field Theory* (Westview Press,1995);

[5] George Sterman, *An Introduction To Quantum Field Theory* (Cambridge University Press,1993).

[6] S. Weinberg, *The Quantum Theory of Fields*,Vols.1-3 (Cambridge University Press,1996).

[7] John Collins, *Foundations of Perturbative QCD* (Cambridge Monographs on Particle Physics, Nuclear Physics and Cosmology,2011)

[8] Y. Kovchegov, E. Levin, *Quantum Chromodynamics at high energy* (Cambridge University Press,New York,2012).

[9] R. G. Roberts, *The structure of the proton:Deep Inelastic Scattering* (Cambridge University Press,New York,1990).

[10] J. R. Forshaw,D. A. Ross, *Quantum chromodynamics and the pomeron* (Cambridge University Press,New York,1997).

[11] R. K. Ellis, W. J. Stirling, and B. R. Webber, *QCD and Collider Physics* (Cambridge University Press, 2003).

[12] F. J. Yndurain, *The theory of quark and gluon interactions* (Fourth edition Springer, 2006).

[13] Gerard t Hooft (2008) Gauge theories. Scholarpedia, 3(12):7443.

[14] Wu-Ki Tung (2009) Bjorken scaling. Scholarpedia, 4(3):7412.

[15] J. J. Aubert *et al.* [European Muon Collaboration], Phys. Lett. B **123**, 275 (1983).

[16] D. Higinbotham, G. AMiller, O. Hen and K. Rith, CERN Courier **53N4**, 24 (2013)

[17] Lepage, G. Peter and Brodsky, Stanley J., Phys. Rev. D. **22**, 2157 (1980).

[18] Brodsky, S. J., and H. C. Pauli., *Schladming Lectures*, SLAC-PUB-5558/91, (1991).

[19] S. Brodsky, H-C. Pauli and S. S. Pinsky, Phys. Rept. **301**, 299 (1998)

[20] G. Altarelli and G. Parisi, Nucl. Phys. B. **126**, 298 (1977)

[21] Yu. L. Dokshitzer, Sov. Phys. JETP. **46**, 641 (1977)

[22] V. N. Gribov, L. N. Lipatov., Sov. J. Nucl. Phys. **15**, 438 (1972)

[23] G. Altarelli, Phys. Rep. **81**, 1 (1982)

[24] G. Altarelli,in *Handbook of Particle Physics*, Vol. 1,chapter 4:"QCD: The theory of strong interactions", Editor H. Schopper, Springer Verlag-Landoldt-Boernstein, Heidelberg-Berlin(2008).

[25] H. Georgi and H. D. Politzer, Phys. Rev. D **9**, 416 (1974)

[26] D. J. Gross and F. Wilczek, Phys. Rev. D **9**, 980 (1974)

[27] V. Gribov, *The Theory of Complex Angular Momentum* (Cambridge University press 2003).

[28] P. D. B. Collins, *An Introduction to Regge Theory and High-Energy Physics* (Cambridge University Press,1977).

[29] R. J. Eden, Rep. Prog. Phys. **34** 995(1971).

[30] A. C. Irving and R. P. Worden, Phys. Rep. **34** 117(1977)

[31] O. Nachtmann, [arXiv:hep-ph/0312279v1]

[32] E. Levin, [hep-ph/9808486].

[33] G. 't Hooft Nucl. Phys. B**72**, 461 (1974).

[34] Bjorken, J. D. (1968). *Current Algebra at Small Distances*, in Proceedings of the International School of Physics *Enrico Fermi* Course XLI, J. Steinberger, ed., Academic Press, New York, pp. 55-81.

[35] Bjorken, J. D. (1969). *Asymptotic Sum Rules at Infinite Momentum*. Phys. Rev. 179, 1547- 1553.

[36] A. M. Stasto, J. Phys. G **38**, 124037 (2011)..

[37] A. Accardi, J. L. Albacete, M. Anselmino, N. Armesto, E. C. Aschenauer, A. Bacchetta, D. Boer and W. Brooks *et al.*, [arXiv:1212.1701 [nucl-ex]].

[38] G. Bertsch, S. J. Brodsky, A. S. Goldhaber and J. F. Gunion, Phys. Rev. Lett. **47**, 297 (1981)..

[39] Y. V. Kovchegov and L. D. McLerran, Phys. Rev. D **60**, 054025 (1999), [Erratum-ibid. D **62**, 019901 (2000)]. [hep-ph/9903246].

[40] J. C. Collins, [hep-ph/0106126].

[41] L. Schoeffel, Acta Phys. Polon. Supp. **1**, 379 (2008).

[42] B. Z. Kopeliovich, I. K. Potashnikova and I. Schmidt, Braz. J. Phys. **37**, 473 (2007). [hep-ph/0604097].

[43] C. A. Garcia Canal and R. Sassot, AIP Conf. Proc. **531**, 199 (2000). [hep-ph/9912233].

[44] M. Arneodo and M. Diehl, [hep-ph/0511047].

[45] E. A. De Wolf, J. Phys. G **28**, 1023 (2002), [Acta Phys. Polon. B **33**, 4165 (2002)]. [hep-ph/0203074].

[46] Y. V. Kovchegov and L. D. McLerran, Phys. Rev. D **60**, 054025 (1999) [Erratum-ibid. D **62**, 019901 (2000)] [hep-ph/9903246].

[47] V. N. Gribov Lecture given at the VIII Winter Petersburg NPI School in the beginning of 1973, [arXiv:hep-ph/0006158].

[48] J. W. Cronin, H. J. Frisch, M. J. Shochet, J. P. Boymond, R. Mermod, P. A. Piroue and R. L. Sumner, Phys. Rev. D **11**, 3105 (1975).

[49] A. Donnachie and P. V. Landshoff, Nucl. Phys. B **244**, 322 (1984); Nucl. Phys. B **267**, 690 (1986); Phys. Lett. B **296**, 227 (1992); Z. Phys. C **61**, 139 (1994).

[50] J. Beringer *et al.* [Particle Data Group Collaboration], Phys. Rev. D **86**, 010001 (2012)..

[51] H1 Collaboration, Paper 89 submitted to the International Europhysics Conference on High Energy Physics (EPS 2003), July 2003, Aachen, Germany, available from http://www-h1.desy.de

[52] S. Chekanov *et al.* [ZEUS Collaboration], Eur. Phys. J. C **21**, 443 (2001)

[53] J. L. Albacete, A. Dumitru and C. Marquet, Int. J. Mod. Phys. A **28**, 1340010 (2013)

[54] L. D. Landau, L. M. Lifshitz, *Quantum Mechanics* (Butterworth-Heinemann,1976).

[55] E. Levin, arXiv:hep-ph/9710546.

[56] L. V. Gribov, E. M. Levin, and M. G. Ryskin, Phys. Rept. **100**, 1 (1983).

[57] A. H. Mueller and J. -w. Qiu, Nucl. Phys. B **268**, 427 (1986).

[58] L. D. McLerran and R. Venugopalan, Phys. Rev. D **49**, 2233 (1994) Phys. Rev. D **49**, 3352 (1994) Phys. Rev. D **50**, 2225 (1994)

[59] Y. V. Kovchegov, Phys. Rev. D **54**, 5463 (1996) Phys. Rev. D **55**, 5445 (1997)

[60] E.M. Levin and M.G Ryskin, Nucl. Phys. **B304**, 805 (1988); Sov. J. Nucl. Phys. **45**, 150 (1987); **41**, 300 (1985).

[61] A. H. Mueller, Nucl. Phys. B **415**, 373 (1994).

[62] A. H. Mueller and B. Patel, Nucl. Phys. B **425**, 471 (1994) [hep-ph/9403256].

[63] A. H. Mueller, Nucl. Phys. B **437**, 107 (1995)

[64] L. D. McLerran and R. Venugopalan, Phys. Rev. D **49**, 3352 (1994)

[65] L. D. McLerran and R. Venugopalan, Phys. Rev. D **50** (1994) 2225

[66] Y. V. Kovchegov, Phys. Rev. D **55**, 5445 (1997)

[67] J. Jalilian-Marian, A. Kovner, L. D. McLerran and H. Weigert, Phys. Rev. D **55**, 5414 (1997)

[68] J. Jalilian-Marian, A. Kovner, A. Leonidov and H. Weigert, Nucl. Phys. B **504** (1997) 415

[69] J. Jalilian-Marian, A. Kovner, A. Leonidov and H. Weigert, Phys. Rev. D **59**, 014014 (1999)

[70] J. Jalilian-Marian, A. Kovner and H. Weigert, Phys. Rev. D **59**, 014015 (1999)

[71] J. Jalilian-Marian, A. Kovner, A. Leonidov and H. Weigert, Phys. Rev. D **59**, 034007 (1999) [Erratum-ibid. D **59**, 099903 (1999)]

[72] A. Kovner, J. G. Milhano and H. Weigert, Phys. Rev. D **62**, 114005 (2000)

[73] H. Weigert, Nucl. Phys. A **703**, 823 (2002)

[74] E. Iancu, A. Leonidov and L. D. McLerran, Nucl. Phys. A **692**, 583 (2001)

[75] E. Ferreiro, E. Iancu, A. Leonidov and L. McLerran, Nucl. Phys. A **703**, 489 (2002)

[76] Y. V. Kovchegov, Phys. Rev. D **60**, 034008 (1999)

[77] Y. V. Kovchegov, Phys. Rev. D **61**, 074018 (2000)

[78] I. Balitsky, Nucl. Phys. B **463**, 99 (1996) I. Balitsky, Phys. Rev. Lett. **81**, 2024 (1998) I. Balitsky, Phys. Rev. D **60**, 014020 (1999)

[79] I. Balitsky, arXiv:hep-ph/9706411.

[80] E. Iancu and R. Venugopalan, In *Hwa, R.C. (ed.) et al.: Quark gluon plasma* 249-3363

[81] J. Jalilian-Marian and Y. V. Kovchegov, Prog. Part. Nucl. Phys. **56**, 104 (2006)

[82] E. Gotsman, E. Levin and U. Maor, Nucl. Phys. B **493**, 354 (1997)

[83] J. Bartels, J. R. Ellis, H. Kowalski and M. Wusthoff, Eur. Phys. J. C **7**, 443 (1999)

[84] K. J. Golec-Biernat and M. Wusthoff, Phys. Rev. D **59**, 014017 (1999)

[85] K. J. Golec-Biernat and M. Wusthoff, Phys. Rev. D **60**, 114023 (1999)

[86] E. Gotsman, E. Levin, M. Lublinsky, U. Maor, and K. Tuchin, arXiv:hep-ph/0007261.

[87] K. J. Golec-Biernat and C. Marquet, Phys. Rev. D **71**, 114005 (2005)

[88] Y. Li and K. Tuchin, Phys. Rev. D **77**, 114012 (2008)

[89] Y. V. Kovchegov, Phys. Rev. D **64**, 114016 (2001) [Erratum-ibid. D **68**, 039901 (2003)]

[90] A. Kovner and U. A. Wiedemann, Phys. Rev. D **64**, 114002 (2001)

[91] A. Kovner, M. Lublinsky, and H. Weigert, Phys. Rev. D **74**, 114023 (2006)

[92] M. Wusthoff, Phys. Rev. D **56**, 4311 (1997)

[93] C. Marquet, Nucl. Phys. B **705**, 319 (2005)

[94] C. Marquet, Phys. Rev. D **76**, 094017 (2007)

[95] S. Munier and A. Shoshi, Phys. Rev. D **69**, 074022 (2004)

[96] M. S. Kugeratski, V. P. Goncalves and F. S. Navarra, Eur. Phys. J. C **46**, 413 (2006)

[97] H. Kowalski, T. Lappi and R. Venugopalan, Phys. Rev. Lett. **100**, 022303 (2008)

[98] H. Kowalski, T. Lappi, C. Marquet and R. Venugopalan, Phys. Rev. C **78**, 045201 (2008)

[99] Y. Li and K. Tuchin, Nucl. Phys. A **807**, 190 (2008)

[100] Y. Li and K. Tuchin, Phys. Rev. C **78**, 024905 (2008)

[101] K. Tuchin, Phys. Rev. C **79**, 055206 (2009)

[102] Y. V. Kovchegov and A. H. Mueller, Nucl. Phys. B **529**, 451 (1998).

[103] Y. V. Kovchegov and K. Tuchin, Phys. Rev. D **65**, 074026 (2002).

[104] M. A. Braun, Phys. Lett. B **483**, 105 (2000)

[105] A. Dumitru and L. D. McLerran, Nucl. Phys. A **700**, 492 (2002)

[106] J. P. Blaizot, F. Gelis, and R. Venugopalan, Nucl. Phys. A **743**, 13 (2004)

[107] D. Kharzeev, E. Levin, and L. McLerran, Phys. Lett. B **561**, 93 (2003)

[108] D. Kharzeev, Y. V. Kovchegov, and K. Tuchin, Phys. Rev. D **68**, 094013 (2003)

[109] D. Kharzeev, Y. V. Kovchegov, and K. Tuchin, Phys. Lett. B **599**, 23 (2004)

[110] R. Baier, A. Kovner, and U. A. Wiedemann, Phys. Rev. D **68**, 054009 (2003)

[111] E. Iancu, K. Itakura, and D. N. Triantafyllopoulos, Nucl. Phys. A **742**, 182 (2004)

[112] A. H. Mueller, Nucl. Phys. B **335**, 115 (1990).

[113] E. A. Kuraev, L. N. Lipatov, and V. S. Fadin, Sov. Phys. JETP **45**, 199 (1977) [Zh. Eksp. Teor. Fiz. **72**, 377 (1977)].

[114] I. I. Balitsky and L. N. Lipatov, Sov. J. Nucl. Phys. **28** (1978) 822 [Yad. Fiz. **28** (1978) 1597].

[115] V. S. Fadin and L. N. Lipatov, Phys. Lett. B **429**, 127 (1998)

[116] M. Ciafaloni and G. Camici, Phys. Lett. B **430**, 349 (1998)

[117] G. P. Salam, JHEP **9807**, 019 (1998).

[118] M. Ciafaloni, D. Colferai and G. P. Salam, Phys. Rev. D **60**, 114036 (1999).

[119] M. Ciafaloni, D. Colferai, G. P. Salam and A. M. Stasto, Phys. Rev. D **68**, 114003 (2003)

[120] M. Ciafaloni, D. Colferai, G. P. Salam and A. M. Stasto, Phys. Rev. D **66**, 054014 (2002)

[121] M. Ciafaloni, D. Colferai, G. P. Salam and A. M. Stasto, Phys. Lett. B **541**, 314 (2002)

[122] J. R. Forshaw, D. A. Ross and A. Sabio Vera, Phys. Lett. B **498**, 149 (2001)

[123] M. Ciafaloni, M. Taiuti and A. H. Mueller, Nucl. Phys. B **616**, 349 (2001)

[124] S. J. Brodsky, V. S. Fadin, V. T. Kim, L. N. Lipatov and G. B. Pivovarov, JETP Lett. **70**, 155 (1999)

[125] D. A. Ross, Phys. Lett. B **431**, 161 (1998)

[126] E. Levin, hep-ph/9806228.

[127] N. Armesto, J. Bartels and M. A. Braun, Phys. Lett. B **442**, 459 (1998)

[128] Y. V. Kovchegov and A. H. Mueller, Phys. Lett. B **439**, 428 (1998)

[129] E. Levin, Nucl. Phys. B **453**, 303 (1995)

[130] M. A. Braun, Phys. Lett. B **348**, 190 (1995)

[131] Y. V. Kovchegov and H. Weigert, Nucl. Phys. A **784**, 188 (2007)

[132] Y. V. Kovchegov and H. Weigert, Nucl. Phys. A **789**, 260 (2007)

[133] Y. V. Kovchegov and H. Weigert, Nucl. Phys. A **807**, 158 (2008)

[134] I. Balitsky, Phys. Rev. D **75**, 014001 (2007)

[135] A. H. Mueller, D. N. Triantafyllopoulos, Nucl. Phys. **B640**, 331-350 (2002).

[136] D. N. Triantafyllopoulos, Nucl. Phys. B **648**, 293 (2003)

[137] J. Kuokkanen, K. Rummukainen and H. Weigert, Nucl. Phys. A **875**, 29 (2012)

[138] H. Weigert, Nucl. Phys. A **783**, 165 (2007).

[139] G. Chachamis, M. Lublinsky and A. Sabio Vera, Nucl. Phys. A **748**, 649 (2005)

[140] A. Kormilitzin and E. Levin, Nucl. Phys. A **849**, 98 (2011)

[141] E. Gotsman, E. Levin, U. Maor and E. Naftali, Nucl. Phys. A **750**, 391 (2005)

[142] E. Gotsman, E. Levin, M. Lublinsky and U. Maor, Eur. Phys. J. C **27**, 411 (2003)

[143] H. Kowalski, L. Motyka and G. Watt, Phys. Rev. D **74**, 074016 (2006)

[144] N. N. Nikolaev and B. G. Zakharov, Z. Phys. C **49**, 607 (1991).

[145] E. Levin and K. Tuchin, Nucl. Phys. B **573**, 833 (2000) [hep-ph/9908317].

[146] E. Levin and K. Tuchin, Nucl. Phys. A **691**, 779 (2001)

[147] E. Levin and K. Tuchin, Nucl. Phys. A **693**, 787 (2001)

[148] R. K. Ellis, Z. Kunszt and E. M. Levin, Nucl. Phys. B **420**, 517 (1994) [Erratum-ibid. B **433**, 498 (1995)].

[149] A. L. Ayala Filho, M. B. Gay Ducati and E. M. Levin, Nucl. Phys. B **511**, 355 (1998)

[150] K. Tuchin, Nucl. Phys. A **798**, 61 (2008)

[151] E. Iancu, K. Itakura and L. McLerran, Nucl. Phys. A **708**, 327 (2002)

[152] B. A. Kniehl, G. Kramer and B. Potter, Nucl. Phys. B **597**, 337 (2001)

[153] D. Boer, M. Diehl, R. Milner, R. Venugopalan, W. Vogelsang, D. Kaplan, H. Montgomery and S. Vigdor *et al.*, arXiv:1108.1713 [nucl-th].

[154] E. Gotsman, E. Levin, M. Lublinsky, U. Maor and K. Tuchin, Nucl. Phys. A **697** (2002) 521.

[155] K. Tuchin, Nucl. Phys. A **854**, 198 (2011)

[156] L. Trentadue and G. Veneziano, Phys. Lett. B **323**, 201 (1994).

[157] A. Berera and D. E. Soper, Phys. Rev. D **53**, 6162 (1996)

[158] J. C. Collins, Phys. Rev. D **57**, 3051 (1998) [Erratum-ibid. D **61**, 019902 (2000)]

[159] F. Hautmann, Z. Kunszt and D. E. Soper, Phys. Rev. Lett. **81**, 3333 (1998)

[160] K. Tuchin and D. Wu, Phys. Rev. D **83**, 054027 (2011).

[161] K. Tuchin and D. Wu, Phys. Rev. D **85**, 114021 (2012).